UNIVERSITÉ DE LILLE

Sciences de la Matière du Rayonnement et de l'Environnement

Thèse de Doctorat

préparée et soutenue publiquement par

Rouba YAACOUB

le 6 Février 2020

pour l'obtention du grade de Docteur de l'Université de Lille

Spécialité: Terre, enveloppes fluides

Laboratoire Optique Atmosphérique (UFR de Physique)

Résonance optique par effet tunnel en optique atmosphérique: application aux observations par satellite des gouttelettes de nuages

---

Olga Korotkova	Professeur	Université de Miami	Rapporteur
Valery Shcherbakov	Professeur	LaMP, Aubière	Rapporteur
Nicolas Rivière	Ingénieur de recherche	ONERA, Toulouse	Examinateur
Céline Cornet	Professeur	LOA, Lille	Président du jury
Olivier Pujol	Maître de conférences	LOA, Lille	Directeur
Philippe Dubuisson	Professeur	LOA, Lille	Co-directeur

UNIVERSITÉ DE LILLE

Sciences de la Matière du Rayonnement et de l'Environnement

Thèse de Doctorat

préparée et soutenue publiquement par

Rouba YAACOUB

le 6 Février 2020

pour l'obtention du grade de Docteur de l'Université de Lille

Spécialité: Terre, enveloppes fluides

Laboratoire Optique Atmosphérique (UFR de Physique)

Tunneling optical resonances in atmospheric optics: application to cloud droplet spaceborne observations

---

Olga Korotkova	Professeur	Université de Miami	Rapporteur
Valery Shcherbakov	Professeur	LaMP, Aubière	Rapporteur
Nicolas Rivière	Ingénieur de recherche	ONERA, Toulouse	Examinateur
Céline Cornet	Professeur	LOA, Lille	Président du jury
Olivier Pujol	Maître de conférences	LOA, Lille	Directeur
Philippe Dubuisson	Professeur	LOA, Lille	Co-directeur

Résumé

L'interaction de la lumière avec un diélectrique sphérique homogène (par exemple une gouttelette d'eau) de caractéristiques connues (diamètre, indice optique) est traitée, en optique atmosphérique, par la théorie de Mie. Cette théorie sert aussi en télédétection pour calculer les propriétés physiques des diffuseurs à partir de méthodes inverses.

Des études récentes ont toutefois suggéré qu'un effet tunnel pourrait être important en optique atmosphérique. Selon ces études, la théorie de Mie, telle qu'utilisée en optique atmosphérique, représente mal cet effet par lequel un objet physique passe à travers une barrière potentielle. Une manifestation de cet effet tunnel est la gloire atmosphérique qui est l'irisation circulaire qui se forme autour de l'ombre projetée d'un objet sur un nuage de gouttelettes d'eau. Plus précisément, la lumière suffisamment proche de la gouttelette la pénètre par effet tunnel et excite des résonances aiguës. Nous avons designé ces résonances par l'acronyme TOR (en anglais: Tunneling Optical Resonance). Dans cette thèse, nous montrons que les TOR peuvent être identifiés et caractérisés en utilisant l'équation de Shrödinger à une dimension en introduisant une énergie potentielle effective qui caractérise l'interaction lumière-gouttelette et qui dépend de l'indice optique, du diamètre de la gouttelette et de l'énergie incidente.

Le premier objectif de cette thèse est d'identifier et de caractériser ces TOR. Afin d'atteindre cet objectif, une nouvelle méthode (méthode de la matrice de transfert – TMM) est développée pour déterminer les conditions pour lesquelles les TOR se produisent. Le deuxième objectif est de comparer cette méthode à celle de la théorie de Mie telle qu'habituellement utilisée en optique atmosphérique. Nos résultats montrent la similarité entre les deux méthodes en l'absence de TOR mais soulignent des désaccords dans le cas contraire. Cette étude est effectuée pour deux cas différents: (1) une seule gouttelette d'eau de diamètre bien déterminé et une énergie incidente précise; (2) une population de gouttelettes de nuage, dont les diamètres varient de 5μm jusqu'à 30μm , et pour des énergies incidentes correspondant aux neuf canaux (de l'IR jusqu'à l'UV) du capteur POLDER. Pour les deux cas, les sections efficaces (diffusion, extinction et absorption) et la distribution angulaire de l'intensité diffusée sont comparées en prenant compte les TOR et sans les considérer. Les résultats suggèrent une nouvelle approche pour l'interaction lumière-gouttelette en optique atmosphérique, qui pourrait conduire a modifier les algorithmes d'inversion en télédétection et de transfert radiatif.

Mots-clés: Effet tunnel, théorie de Mie, diffusion optique, nuages, télédétection

Abstract

The light interaction with a homogeneous dielectric spherical scatterers (*e.g.* cloud droplet) of known characteristics (diameter, optical index) is treated, in atmospheric optics, by the Mie theory. This theory serves, also, in remote sensing to retrieve physical properties of scatterers from the inverse methods.

However, recent studies have suggested that a tunneling effect could be significant in atmospheric optics. According to these studies, the Mie theory, as used in atmospheric optics, may misrepresent this effect for this effect by which a physical object passes through a potential barrier. A manifestation of the tunnel effect is the atmospheric glory, which is the circular iridescence that forms around the projected shadow of an object on a cloud of water droplets. Specifically, light close enough to the water droplet penetrates te droplet by tunnel effect and excites sharp resonances. We designed these resonances by the acronym TOR (Tunneling Optical Resonance). In this thesis, we show that TOR can be solved using a one-dimensional Schrödinger equation with an effective potential energy that characterizes the light-droplet interaction and that depends on the refractive index, diameter of the droplet and the incident light energy.

The first main purpose of this thesis is to identify and characterize these TOR. In order to reach this goal, a new method (called transfer matrix method – TMM) is developed that allows the determination of the conditions for which TOR occur. The second main purpose is to compare this method to the Mie theory as commonly used in atmospheric optics. Our findings show the similarity of the two methods in the case of non-TOR occurrences but highlight disagreements for the TOR case. This study is performed upon two different cases: (1) a single water droplet with a well defined diameter and a specific incident energy; (2) a population of cloud droplets of diameters ranging from 5μm to 30μm for the incident energies that correspond to the nine channels (from IR to UV) of the POLDER sensor. For both (1) and (2), cross sections (scattering, extinction and absorption) and the angular distributions of the scattered intensity are compared when taking into account the TOR and without considering them. The results suggest a new approach for addressing light-droplet interaction in atmospheric optics that may lead to modify some algorithms in remote sensing and radiative transfer.

Keywords: Tunneling effect, Mie theory, optical scattering, clouds, remote sensing

Contents

CHAPTER 1 Introduction

"Vous avez confirmé dans ces lieux pleins d'ennui ce que Newton connut sans sortir de chez lui – You confirmed in these places full of boredom what Newton knew without leaving his home" – said the philosopher Voltaire, symbolizing the significance of theories and their physical propositions for a better understanding to our surrounding and the visual natural phenomena.

In this vast world, plenty of optical, breathtaking, phenomena occur such as rainbows, coronas, glories, light pillars, aurora, etc. Thus, theory and laws should present not only a suitable explanations and convenient demonstrations to the existence of these phenomena, but also a correct predictions of new phenomena. The theory adopted by the atmospheric optics – Mie theory – is capable to explain most of the phenomena mentioned above. A particular phenomenon, the glory, hadn't have a complete explanation to its occurrence although the presence of the Mie theory. Figure 1.1 illustrates two photos of the manifestation of glories through the clouds, one taken from an airplane and the second is taken from a top of the mountain.

a) Photo by Olivier Pujol

b) Photo by Philippe Dubuisson

Figure 1.1: Glories observed (a) from an airplane (b) and from top of a mountain

Since the glory has been seen, physicists tried to present the best way to explain it, and their suggestions ended up with a big failure and with contradictions with the classical optical theory. Nevertheless some recent studies showed a promising prospect by introducing a quantum mechanical effect "the tunneling resonances" as the origin of the glory. This suggestion was first introduced by the physicist Nussenzveig and later on by other physicists who proved some other significant parameters related to the occurrences of the glories.

Nussenzveig's suggestion is based on the treatment of the interaction light-droplet and that this interaction should be solved within the quantum physics. A suggestion that took Nussenzveig almost forty years by creating his own theory followed by studies and collaborations to achieve a reasonable explanation. In this work, we have adopted the suggestion made by Nussenzveig so we can test, in first step, the impact of tunneling resonances on the optical parameters such as cross sections and light intensity. Serving from the cross sections impacts to examine, in a second step, two of the most important transfer radiative parameters the cloud optical thickness (COT) and single scatter Albedo (SSA).

Therefore we will present a deeper examination of the tunneling resonances: Can we visualize the occurrence of glories via theory? In which state the glory exists and for which conditions it manifests? For which diffusion angle does it appear and why the Mie theory couldn't explain its geometrical existences? These questions will be answered subsequently. Once the answers of these questions are clear and set, we proceed to the next goal of this thesis in comparing these results to those given by the Mie theory.

In this chapter, we shall start with the first sightings of the glory world-wide and the delusive explanations that follow this appearance proposed by physicists through centuries. The second part is devoted to present some optical parameters such as the clouds phase and COT for a extracted image of a glory via satellite POLDER. And for the third part, we will present the outline of this manuscript.

I. HISTORY OF THE GLORY

I.1 Each one is his/her own saint – The first sightings of the glory

The glory, also called Ulloa circle, was described for the first time by Juan and Ulloa in their book "Voyage historique de l'Amérique Meridionale" released in 1752. This book was written based on the expedition, led by Bouguer and La Condamine, to – what is known now as – the

Ecuador, commissioned by King Philip V in order to determine the shape of the Earth. The glory was seen in between August 1737 and July 1739 at the top of Pambamarca's mountain. Juan and Ulloa transformed what they saw into a figure – Figure 1.2 – presented in the book Lynch and Futterman (1991).

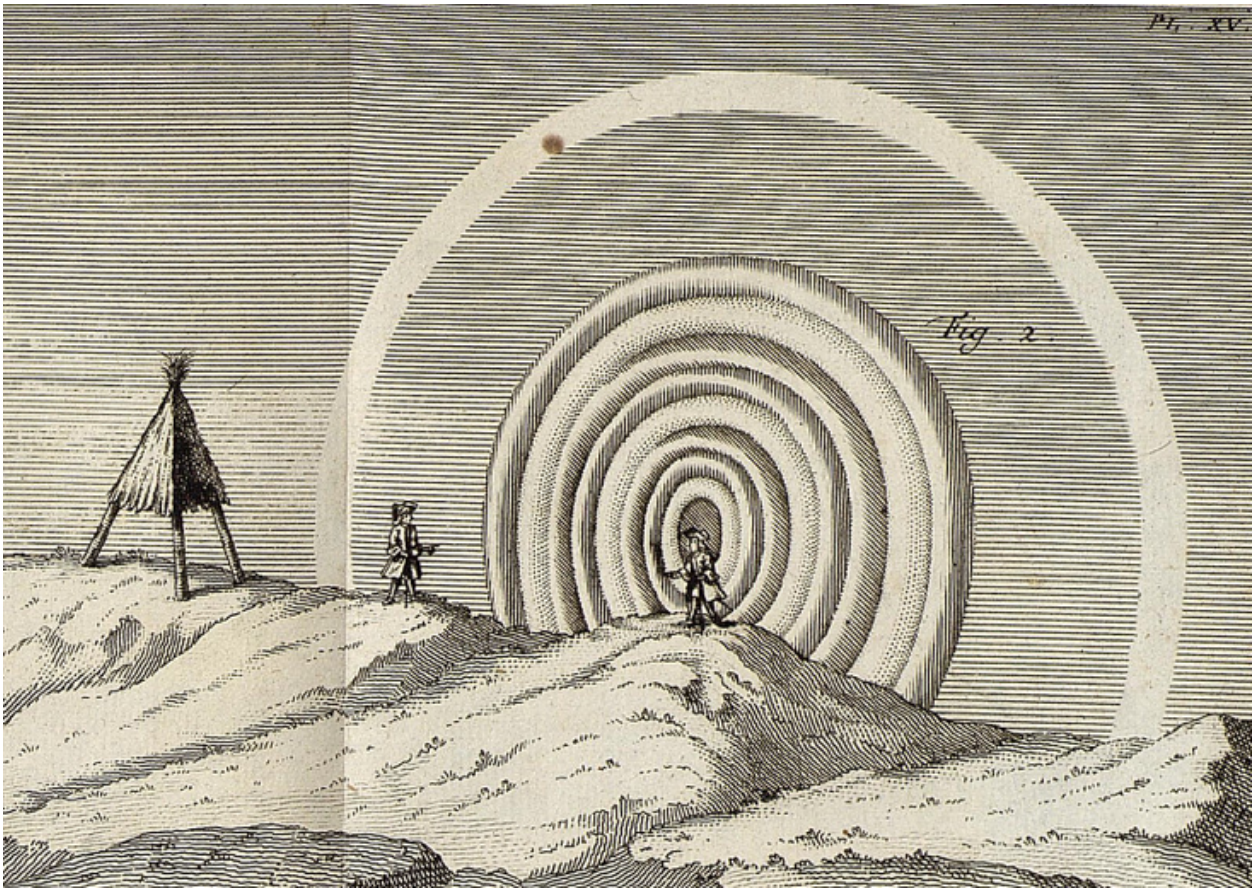

Figure 1.2: The original zoomed-figure of the Ulloa circle at the Pambamarca's mountain (Ulloa et al., 1752)

Bouguer gave a detailed description on what he saw (Pernter and Exner, 1910): "*A phenomenon which must be as old as the world, but which no one seems to have observed so far ... A cloud that covered us dissolved itself and let through the rays of the rising sun ... Then each of us saw his shadow projected upon the cloud ... The closeness of the shadow allowed all its parts to be distinguished: arms, legs, the head. What seemed most remarkable to us was the appearance of a halo or glory around the head, consisting of three or four small concentric circles, very brightly colored, each of them with the same colors as the primary rainbow, with red outermost ...*". The description that came in Ulloa et al. (1752) was similar to what

Bouguer had explained: "*The most surprising thing was that of the six or seven people that were present, each one saw the phenomenon only around the shadow of his own head, and saw nothing around other people's heads ...*". He continued "*When the Phenomenon began, the Arches seemed to be oval in shape or elliptical like the disk of the Sun, but then they little by little became perfectly circular. Each little Arch was red or rose, but this color faded and the color orange succeeded it, followed by yellow, then by jonquil – pale yellow, and finally by green; the outer-most color always stayed red. All that can be better understood by the engraving herein*". As Bouguer said, this phenomenon is old as the world; the mountain Brocken in Hanovre was known to be an *usual theater extraordinary appearances* (Tissandier, 1873). M.Hane's curiosity made him climb the Brocken mountain more than thirty times so he can witness, on May 1797, the Brocken spectrum. Hereafter, the Brocken spectrum attracted, on 1862, the painter M.Stroobant "*His shape through the clouds was weak but was encountered by the seven color of the rainbow*" (Tissandier, 1873). This phenomenon didn't just tempt scientists, in 1828 the romantic writer Samuel Taylor Coleridge mentioned the glory in his poem "Constancy to an ideal object". The balloonist Gaston Tissandier with Admiral Baron Roussin stated: "*we had the happiness to see these beautiful phenomena appear in front of our eyes in their magnificence*" in their 18^{th} aerostatic ascension illustrated in Figure 1.3, "*The shadow of the balloon is surrounded by a pale elliptical halo, but where the seven colors of the spectrum appear visibly, in concentric zones*". He continued "*The smallest details of the balloon ... are drawn with the sharpness of the Chinese shadows. Our silhouettes stand out regularly against the silver background of the cloud; we raise our arms, and our lookalike raise their arms*". On February the 16^{st} 1873, they were able to witness again this phenomenon with exceptional conditions – for three consecutive hours "*..The balloon shadow is projected with remarkable clarity, and a magnificent circular rainbow appears around the shadow of our basket, the engraving on the other hand ... gives a very exact idea of this apparition. The shadow of the nacelle forms the center of iridescent and concentric circles, where the seven colors of the spectrum are distinguished: violet, indigo, blue, green, yellow, orange and red. Purple is interior, and red outside, these two colors are at the same time those which are revealed with the most sharpness*". Figure 1.4 was depicted in Tissandier (1873) to explain: "*we are getting closer to the cloud layer, and the shadow is surrounded this time by three halos with seven elliptical and concentric colors*".

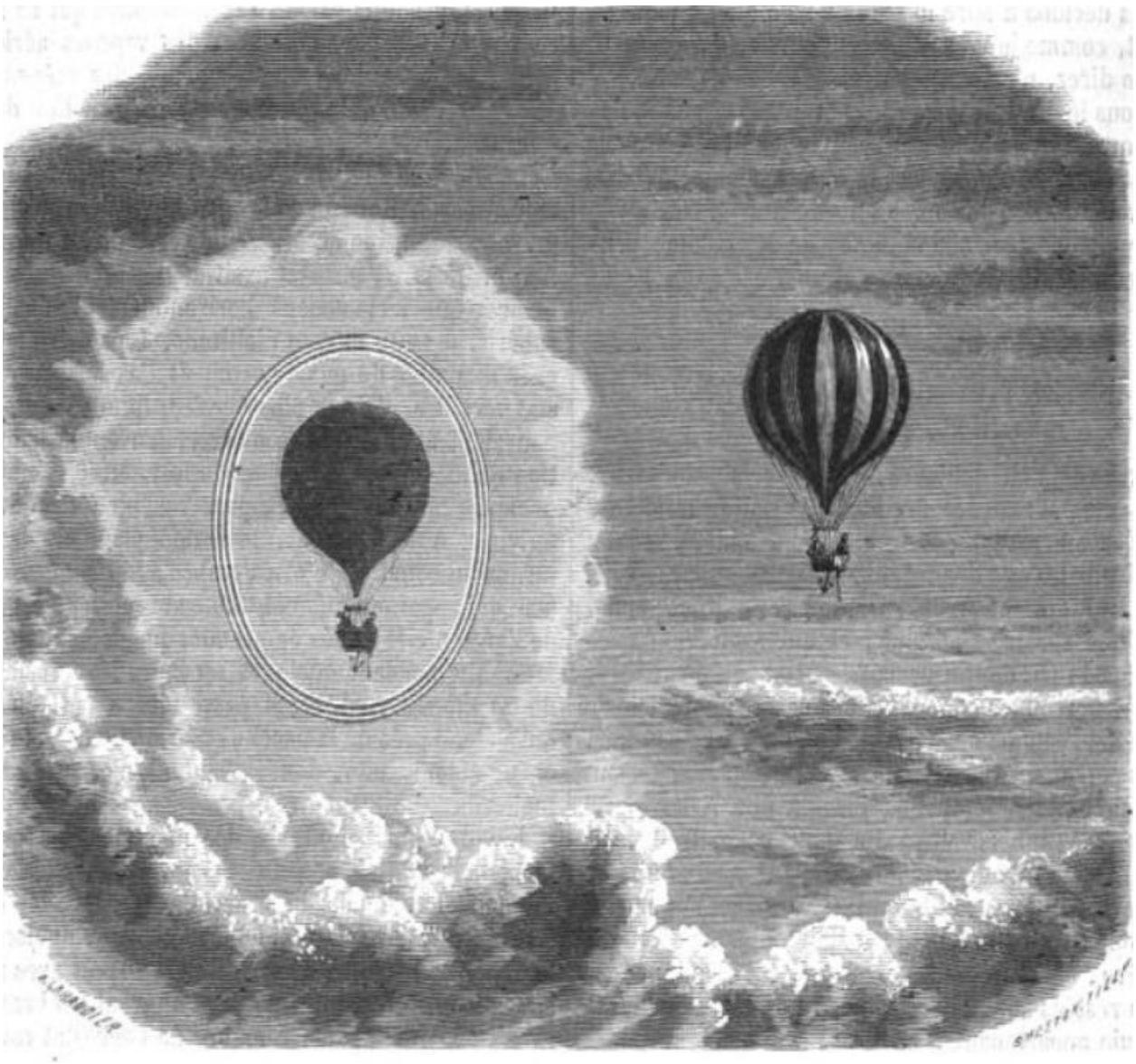

Figure 1.3: The original figure from the balloon on 8 June 1872 by Gaston Tissandier taking from Tissandier (1873)

The Scottish physicist C. T. R. Wilson during his speech at the Nobel Banquet in Stockholm, December 10, 1927, said: "*... I saw the sun rise above a sea of clouds and the shadow of the hill on the clouds below surrounded by gorgeous colored rings. The beauty of what I saw made me fall in love with clouds and I made up my mind to make experiments to learn more about them*" (Wilson, 1927). C. T. R. Wilson intended to reproduce the glory in his laboratory, he failed but he used his invention to detect radiation whence he received a Nobel price.

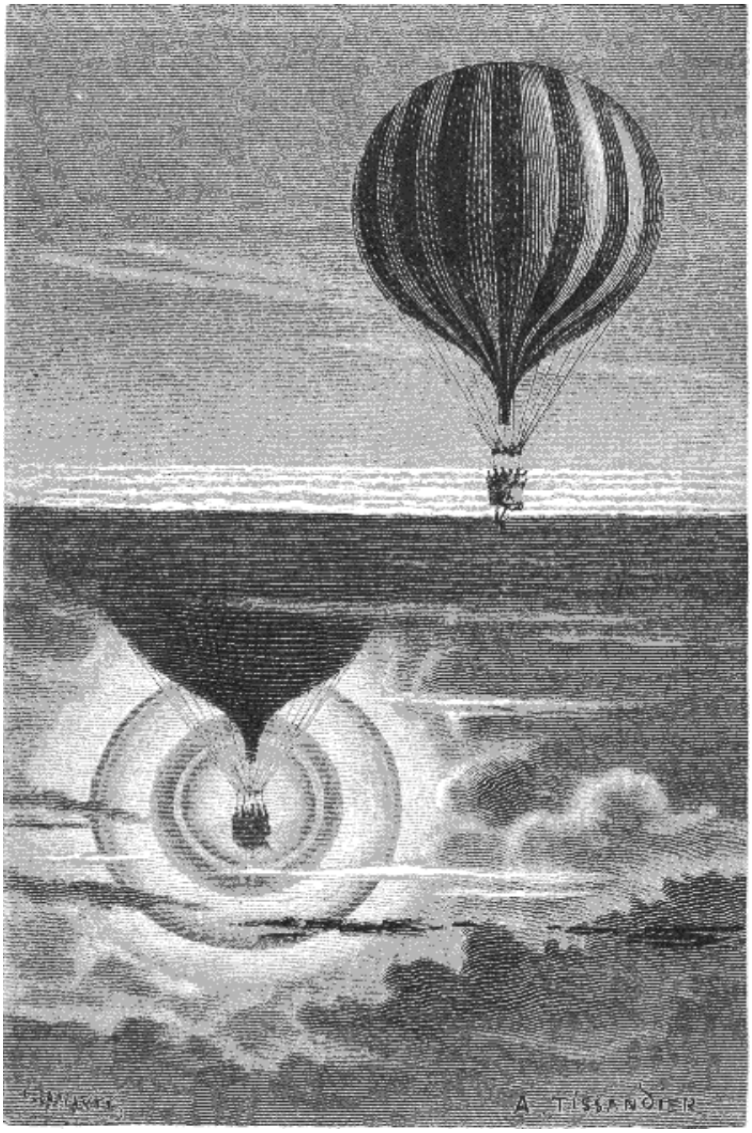

Figure 1.4: The original figure from the balloon on 13 February 1873 by Gaston Tissandier taking from Tissandier (1873).

I . 2 The theoretical essays for understanding the glory

In 1908, Gustav Mie presented a solution of the Maxwell's equations for the light spherical homogeneous dielectric, this solution is nowadays known by theory of Mie. Some formulas of the Mie theory will be briefly presented in the next chapter. This theory is used worldwide, in atmospheric optics, to solve or characterize the scattered light due to a droplet-light interaction (Mie, 1908). Ample studies revolved around the glory properties using the numerical computation of the Mie theory such the "*Effects of refractive index of the glories*"

(Laven, 2008b), the formation of non circular glories (Laven, 2008a), the degree of polarization (Liou and Hansen, 1971) and the angular distribution of scattering of unpolarized sunlight (Laven, 2003).

The shadow (of persons, balloons, etc. ...) while observing a glory gave a hint about the direction of the glory: it is due to a "*back-scattering effect*". From that, physicists attempted to find reasonable explanations for the glory but their attempts ended in disappointment. The first who tried to explain the glory was Joseph Von Fraunhofer (Pernter and Exner, 1910), in the beginning of the 19^{th} century, his idea was based on similarity of the glory with another meteorological effect, the diffraction coronas – a forward diffraction. He believed that (so did Pernter and Exner (1910)) light is scattered by droplets just above the observer's head, the scattered light is then submissive to "reversal of direction of propagation" – reflected back, by a deeper layer of the cloud, the glory then arise from a secondary scattering.

The secondary scattering or the double scattering is what – according to Fraunhofer – caused the colored diffraction rings of the glory. This proposal is shaky because of the following reasons: the regular reflection due by clouds does not happen, the contrast of the glory rings is brighter than those of the coronas; and the angular distribution of intensity is different than the coronas. In 1923, B.B Ray disproved Fraunhofer's proposition (Ray, 1923). Ray finally confirmed from an experimental work with artificial clouds that the glory, due to a primary scattering, arises from back-scattering light within a singular water droplet and that the intensity of the glory rings and the contrast are totally different than those of the coronas. Ray thought (and later by Bricard (1940)) about using the geometrical optics in order to understand the back-scattering effect, produced by an interference between (1) reflected ray by the exterior surface of the droplet and (2) refracted ray that got internal reflection inside the droplet. This proposal is similar to the example of the half-dipped pencil in the water. Although after considering multiple internal reflections, the results was too weak to be taken as glory. Another proposition by Bucerius in 1946 (Bucerius, 1946), based on the "backwards diffraction", the results were not compatible with the intensity and polarization of the glory. In 1947, the astronomer Hendrik C. Van De Hulst (Van De Hulst, 1947) gave a notable explanation to the physical occurrences of the glories. He suggested that a very close luminous ray to the droplet's periphery, enters the droplet within one internal reflection (under a critical angle) following a V-shaped path. This explanation was relatable to geometrical optics, such as virtual focus F, the interference in between rays. The entering ray (referred by a black narrow in Figure 1.5a)) refracts into the droplet and bumps into the other side of

it within a critical angle; since the droplet has a spherical shape – which is symmetrical – the ray leaves the droplet taking the same path as it enters with a critical angle forming the shape of a V, the refractive ray leaves the droplet parallel to the incident ray but in opposite direction. Likewise, adjoining rays pursue the same path within a V-shape presented by two rays in gray dots in Figure 1.5a). As it is shown, the rays seems to leave the droplet as they emerged from the virtual focus F, the interference of the two rays after the internal reflection produce the glory rings. Although the proposal of Van De Hulst seems to be logical, but the whole V-shaped path is applied to a refractive index between 1.4 and 2, while the refractive index of water droplet is 1.33 which causes an angular gap of $\sim 15°$, because the largest deviation (for tangential incident rays) in the case of water droplet reaches $165°$. Therefore Van De Hulst went to search how to patch this gab. Surface waves was the second proposal of Van De Hulst, suggesting a solution for the $15°$ of gab, Figure 1.5b) shows that the rays that touch the surface turn into an electromagnetic surfaces waves, they graze the surface and then enter the droplet. This suggestion was proved afterwards that it is realistic and it can happen, but it didn't gave the same intensity given by a glory. In 1966, H. C. Bryant and

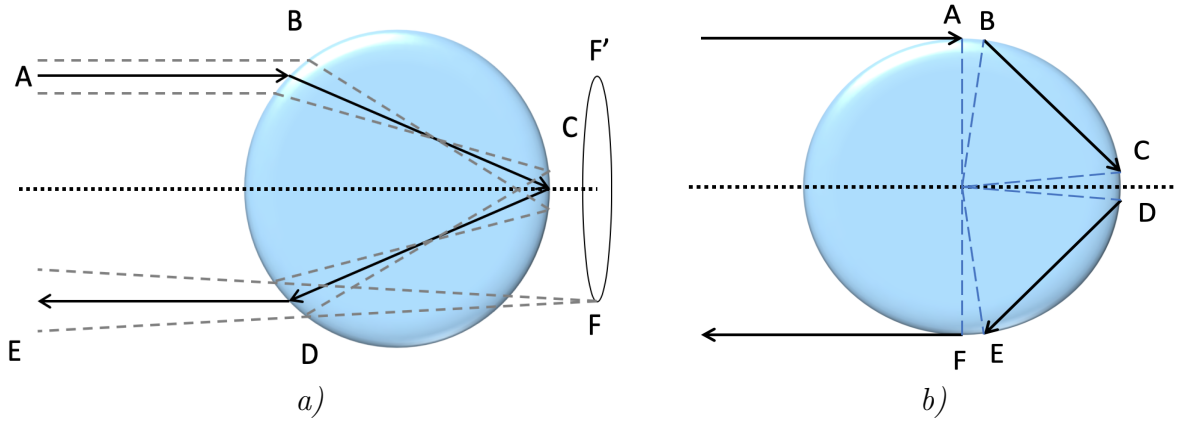

Figure 1.5: The geometrical presentation of the water droplet (a) for Hulst suggestion in 1947 of the V-shape path of the light and the interference of the neighboring rays that creates the glory, (b) the second suggestion of Hulst introducing the surface waves between A and B, C and D, E and F. Re-drawn from Nussenzveig (2006)

A. J. Cox conclude, from numerical investigations, that the glory is a surface wave grazing the surface due to an incident ray very close to the tangential periphery of the droplet.
H.M Nussenzveig, a Brazilian physicist, started in 1965 with a study that lasted 39 years (ended up in 2003) to develop a research over the physical explanation of the glories, and

with the help of several collaborations, this study ended up with a rational answer: wave tunneling. Nussenzveig developed a theory called CAM, abbreviation of Complex Angular Momentum, a new version of complex angular momentum (Nussenzveig, 1965), this theory was re-explained after in details by Nussenzveig (1992) and Adam (2002). CAM theory was invented because of the plenty infinite terms proposed in that converges very slowly, so the uses of this theory was to turn these terms into less convergence with the help of computers. After testing the accuracy of CAM theory, Nussenzveig started to develop and examine his idea about the tunneling inside the sphere. In 1969, Nussenzveig presented, after treating glories by using the scalar scattering within CAM theory, the first confirmation of Van de Hulst's suggestion: the surface waves; this study was totally confirmed by several studies (Khare and Nussenzveig, 1977; Nussenzveig, 1979; Khare, 1982; Nussenzveig, 1992) using the electromagnetic scattering that gave some significant results concerning the glory. In 1987, Nussenzveig and Wiscombe (1987) found by studying the scattering by a total reflection sphere that the ray which is close enough to the water droplet can tunnel into it and will give a very important contribution to the diffraction. After tunneling, the ray will be reflected involving the van de Hulst surface waves and stay trapped inside the droplet. In 1977, Khare and Nussenzveig (1977) evaluated the contribution of rays via Van De Hulst's terms, and in 1994 he studied with Guimarães the Mie resonances. In 2002, Nussenzveig (2002) studied three effects that may be the contributors for the glory: (1) the rays that hit the droplet – also known by the rays in the below-edge zone (Johnson, 1993) – will be detailed after, (2) the tangential rays with surface waves and (3) Mie resonance with the contribution of light tunneling. Therefore according to Nussenzveig (2012) "*The inescapable conclusion is that glories are a macroscopic light-tunneling effect*".

II. POLDER OBSERVATIONS OF GLORY

Besides what is written in bibliography and the marvelous figures taken by artists, photographers, scientists and travelers, we will present an extract figure from a satellite illustrating the existence of the glories (another example is presented in Bréon and Goloub (1998)) in order to verify its occurrences at the back-scattering diffusion angle and to examine its light intensity.

POLDER is an instrument developed by the CNES (Centre National d'Étude Spatiale) in order to study the Earth's atmosphere. The French space agency CNES presents with AERIS,

especially the Data Center ICARE, various services in the field of atmospheric optics such as phase of clouds, the cloud optical thickness, Cloud Mean SW Albedo, and much more of remote sensing Data, given by the satellite POLDER. http://www.icare.univ-lille1.fr
The survey of the satellite POLDER divides the Earth into segments or orbits. This survey gives Data-base from 1996 till 2013, each day, for 12 months, for each orbits. Our aim is to search, in these orbits, the appearance of the phenomenon glory and to present some of its occurrence's optical parameters. A code has been developed (by Fabrice Ducos, a research engineer at the Laboratoire d'Optique Atmosphérique – LOA) to divide orbits into smaller vertical segments that we call them sequences. The purpose of such code is the ability to visualize the occurrences of the glories to the naked eye.
As an example, Figure 1.6a) presents an orbit of a specific day, and Figure 1.7a) to Figure 1.8c) are some of the corresponding sequences of Figure 1.6a). One of the POLDER components is the CCD matrix detector, the latter is composed of an array 242×274 (Deschamps et al., 1994), this array corresponds to 6.5×8.8mm in size. We have detected several glories, including a glory on 10^{st} of May 2010.
The occurrence of this glory will be referred subsequently, by presenting some of the appearances of this glory on the orbit. Figure 1.6a) presents the orbit number "P3L1TBG1124218M" given by the satellite POLDER. This surveyed region commences from the south of Argentina going through Mexico to the center of United States.
Figure 1.6b) is the corresponding clouds phase and Figure 1.6c) is the corresponding cloud optical thickness (COT). These extract Data are given by ICARE. The glory is extended on 10 consecutive sequences.

The most evident and brighten glories, for this specific orbit, are shown in figures: from sequence number 24 (Figure 1.7a)) till sequence number 34 (Figure 1.8c)) and each one of these figures represent a CCD array. To a better illustration, we precise the glory, when it exists clearly, by a blue square. In between these glories, we chose the sequence 28 – Figure 1.8a) over the Eastern Pacific Ocean 13° S, 93° W offshore Chile – as the occurrence of glory that we are going to study because of the clarity of the glory and since our aim, in this work, is to study the liquid clouds and not the ice or mixed clouds.

Going back to Figure 1.6a), the white star highlights the position of the glory presented in sequence 28 (Figure 1.8a)). The black border star in Figure 1.6b) represents the phase of cloud of the glory presented in sequence 28. The star takes up a red space referring to pure liquid clouds.

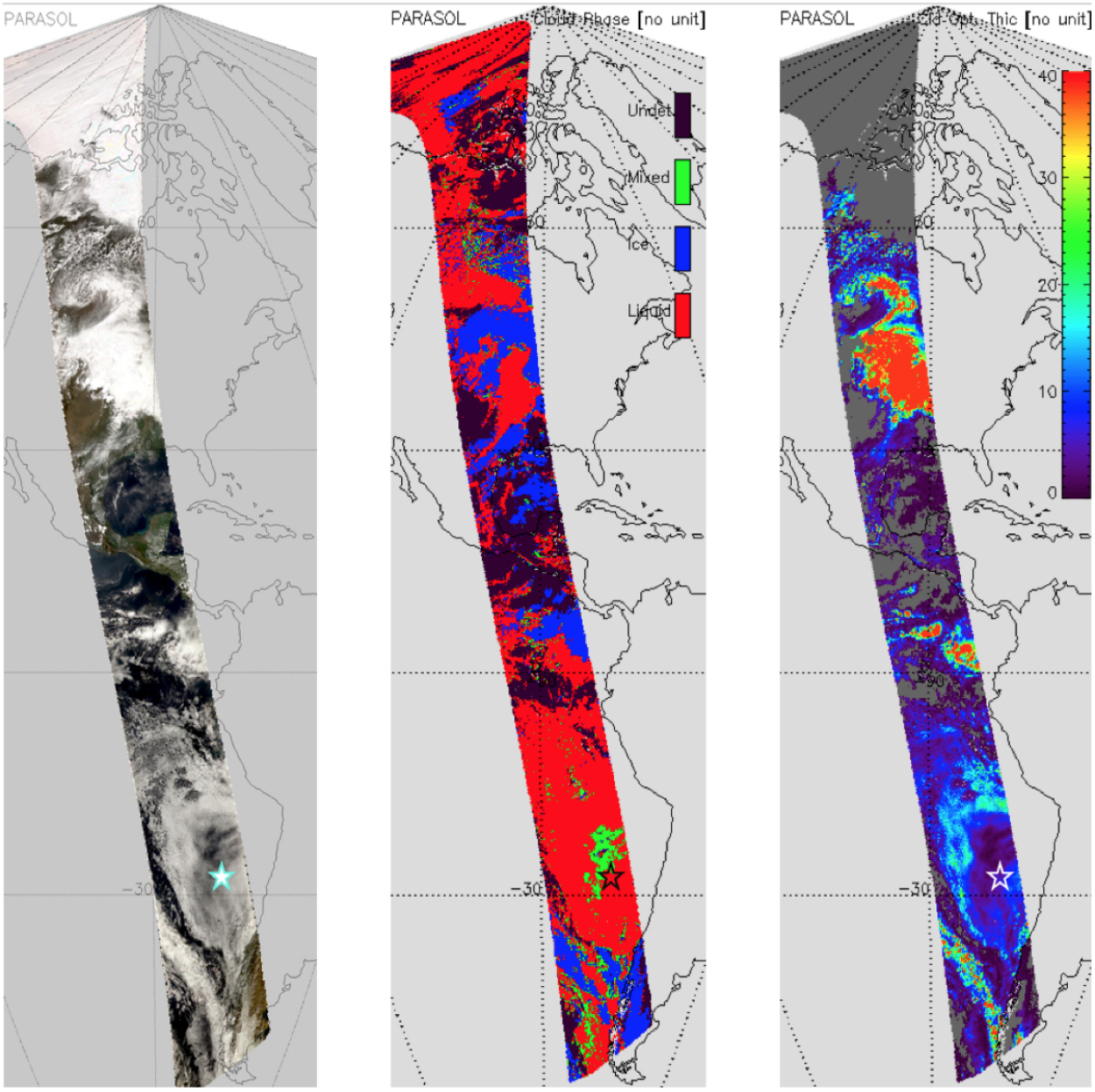

Figure 1.6: POLDER-level 1 Data extract, on the 10^{st} of May 2010 (a) presents the result of an extraction for all the pixels of P3L1TBG1124218M – the white star correspond to the glory of figure 1.8a), (b) presents the phase of the clouds, distributed over four types of clouds: liquid, ice, mixed and undetermined respectively presented in red, blue, green and black – the glory is surrounded by black border star that corresponds to liquid clouds in red color (c) presents the Cloud Optical Thickness – the glory is surrounded by a white border star that corresponds to a value less than 10 .

The degree of transparency of a cloud – also known by COT – is another optical parameter presented in Figure 1.6c). The manifestation of the glory is highlighted in a white border star that corresponds to a value of COT less than 10 .

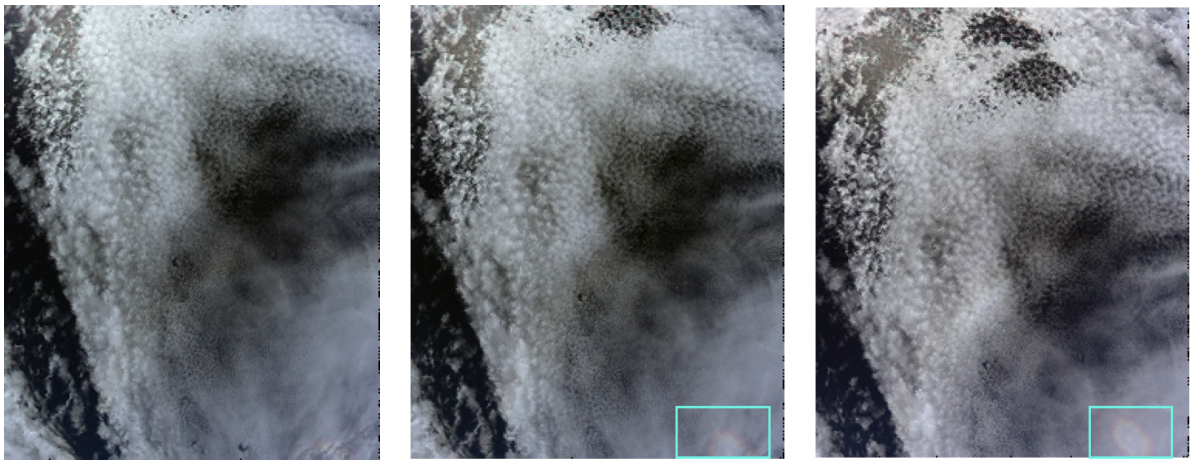

a) *b)* *c)*

Figure 1.7: Picture captured by POLDER-level 1 on the 10^{st} of May 2010 (a) for the sequence 24, (b) for the sequence 26 and (c) for sequence 27, with a blue square that surrounds the position of glory

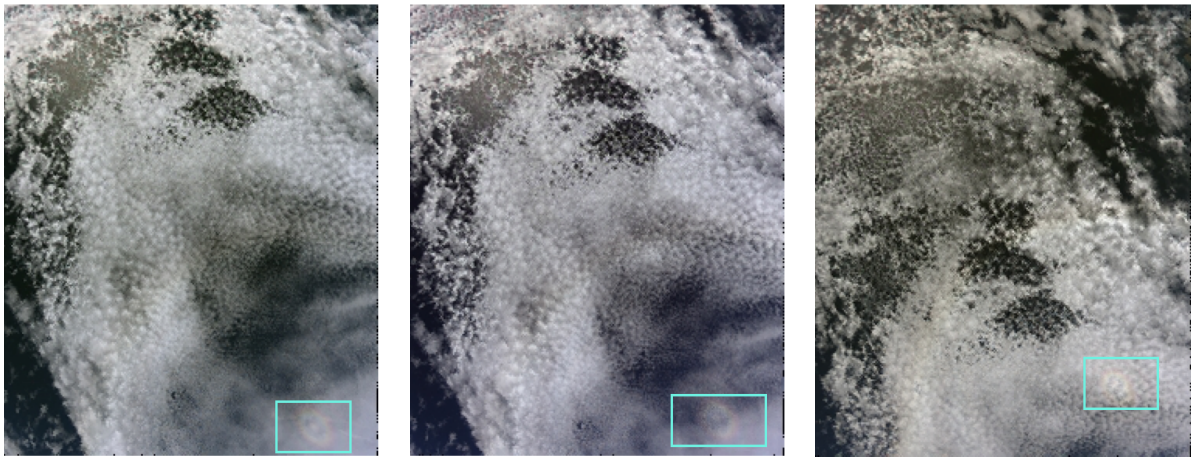

a) *b)* *c)*

Figure 1.8: Similar to Figure 1.7 (a) for the sequence 28, (b) for the sequence 29 and (c) for sequence 34

Figure 1.9a) presents the radiance in $Wm^{-2}sr^{-1}$ and Figure 1.9b) presents the diffusion angles (θ°). These Figures present the extracted Data of Figure 1.8a) as a function of pixel

numbers across the field of view and the pixel numbers along the field of view.
The position of the glory in sequence 28 of Figure 1.9a) is surrounded by a black square. The value, at the position of glory is considered (about $0.433\,Wm^{-2}sr^{-1}$) to be an important value of radiance because it shows, to the naked eye, the obvious shape of the glory with a low value of radiance for its surrounding.
It has been proven that the glory occurs as a back-scattering light (diffusion angle = 180°) which is totally analogous with Figure 1.9b) that represents the diffusion angle of the figure of sequence 28. The diffusion angle is equal to 180° in the same exact position of the glory – symbolized by a black square – of Figure 1.8a). This result confirms that the phenomenon in the orbit number "P3L1TBG1124218M" for sequence 28 is a glory for liquid clouds phase (from Figure 1.6b)).
From this point, and via satellite, the existence of glory is confirmed for pure liquid clouds at diffusion angle $\theta = 180°$.

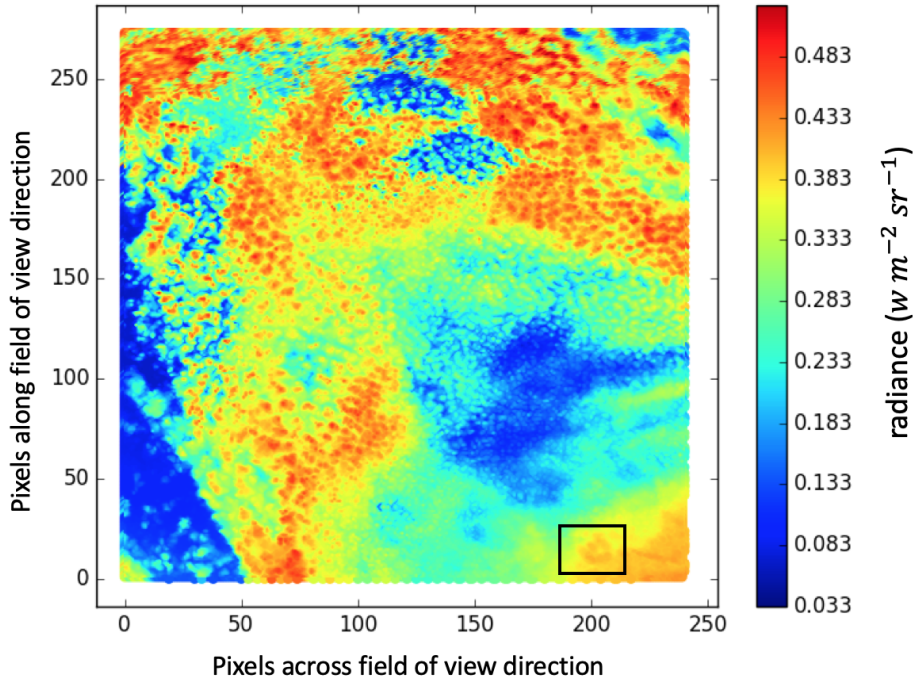

a) the radiance

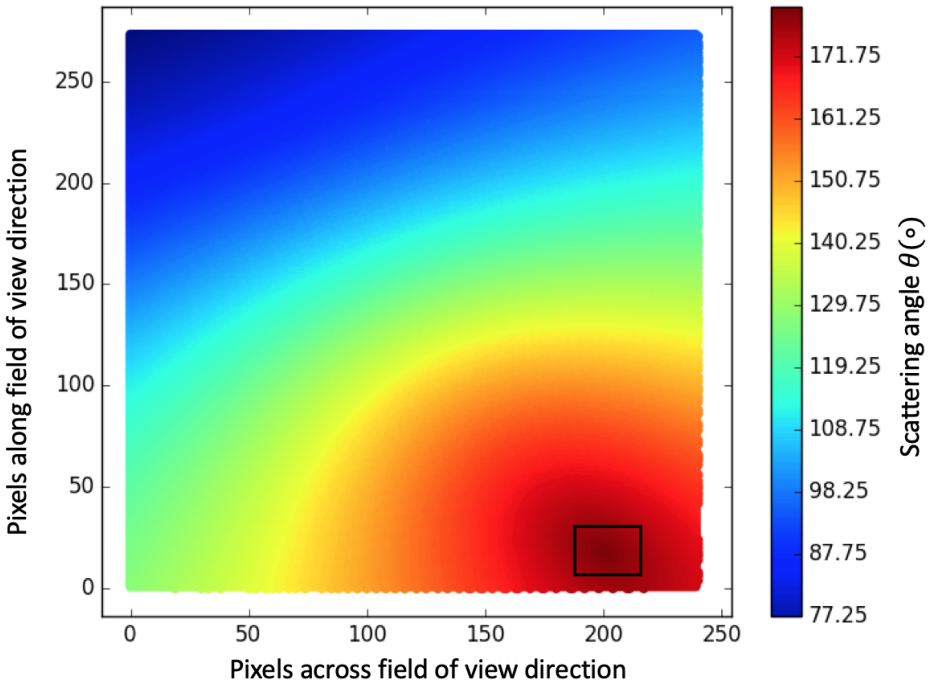

b) the scattering angle

Figure 1.9: (a) The re-drawn of 1.8a) presenting the radiance ($Wm^{-2}sr^{-1}$) in colorbar for each surface pixel (b) The scattering angle $\theta(^{\circ})$ in color-bar of Figure 1.8a) for each surface pixel, with a black square that represents the glory of sequence 28 (Adapted with permission from Yaacoub et al. (2019) ©The Optical Society of America).

III. OUTLINE OF THE MANUSCRIPT

As we illustrated in this chapter, the glory is, in our case, for pure water droplet clouds, occurred at angle of back-scattering with a very remarkable radiance that highlights the shape of the glory (Figure 1.9).

Therefore using these information and the concept proposed by Nussenzveig that we have adopted in this work (the tunneling optical resonance), we will present, in chapter 2, a new insight for the light-droplet interaction. We will start by recalling some formulas of Mie theory, then we will introduce in details the concept of Tunneling Optical Resonance symbolized by TOR, afterwards we will introduce the condition for which this effect exists and some of its characteristics. Also, we will present some optical parameters as the scattering amplitude, the cloud optical thickness and the single scatter Albedo.

In chapter 3, we are going to present the methodology by introducing the transfer matrix method. However, the transfer matrix method is a reachable method used as the base to establish most of this work. This method is used to characterize and locate the position of TOR.

In chapter 4, we will begin by presenting the application of the matrix method and by setting some criteria to the detection of the tunneling resonances values. In the second fold of chapter 4, we will start by choosing a simple distribution of diameters such as a single droplet, and then a more realistic distribution that agrees with small diameters of water droplets based on the wavelengths of the nine channels of POLDER. The cross sections are also presented for more accuracy, the cloud optical thickness and the single scatter Albedo are also calculated for the transfer matrix method and for Mie prediction. The intensities of the nine channels of POLDER are then calculated for its corresponding diffusion angles in order to analyze the impact of the tunneling on the spectral domain of POLDER.

As perspectives, we will present the possible approaches that can be applied using our method to different complex-shaped scatterers and the future solutions that arise from taking into account precisely and explicitly the tunneling resonance into the light-droplet interactions.

This work is the topic of the published article in JOSA Yaacoub et al. (2019). This article is presented in appendix.

CHAPTER 2

Theoretical features of light-droplet interaction

Mie theory is commonly used in atmospheric optics to calculate the cross sections (σ) of absorption, scattering and extinction, for spherical (or almost spherical) cloud droplets of known characteristics (diameter D, optical index $\underline{n} = n + i\,\kappa$) and their related optical properties or to derive these characteristics from remote sensing measurements.

Recent studies had declared that the Mie theory as commonly used in the practices of atmospheric optics may misrepresent some resonances (the first published study was made by Nussenzveig): light in the surrounding of a droplet can penetrate into it and excite sharp resonances. The atmospheric glory (*cf.* Chapter 1) is an evidence of such resonances, that we will call Tunneling Optical Resonance (TOR) because of their physical origin.

The main purpose of this chapter is presented as twofold: the first fold is specified to present a brief reminder of the theory of light-droplet interaction with interest to the Mie theory, and the second part is to explain redundantly the concept of TOR and some of its characteristics. Cross sections are very important elements in radiative transfer (and atmospheric optics), therefore a last segment in this chapter is reserved for some magnitudes of practical interest related to the cross sections such as the Cloud Optical Thickness (COT), and the Single Scattering Albedo (SSA).

I. LIGHT-DROPLET INTERACTION

I.1 Maxwell's equations

Light, an electromagnetic field $[\boldsymbol{E}(\boldsymbol{r},t), \boldsymbol{B}(\boldsymbol{r},t)]$, that interacts with matter is classically given by the Maxwell's equations using the vacuum permittivity (ε_0) and the magnetic permeability in vacuum (μ_0):

$$\begin{cases} \nabla \times \boldsymbol{E} + \dfrac{\partial}{\partial t}\boldsymbol{B} = \boldsymbol{0} \\ \nabla \cdot \boldsymbol{B} = 0 \end{cases} \qquad \begin{cases} \nabla \times \dfrac{\boldsymbol{B}}{\mu_0} - \dfrac{\partial}{\partial t}(\varepsilon_0 \boldsymbol{E}) = \boldsymbol{J} \\ \nabla \cdot (\varepsilon_0 \boldsymbol{E}) = \rho \end{cases} \tag{2.1}$$

In these equations $\boldsymbol{J}$ and ρ are, respectively, the current density and the charge density *i.e.* the sources of the field. The combination in between the terms of Maxwell's equations leads to a vector wave equation:

$$\nabla^2 \boldsymbol{E} - \underline{n}^2 \frac{\partial^2 \boldsymbol{E}}{\partial (ct)^2} = \boldsymbol{0}. \tag{2.2}$$

Vector $\boldsymbol{B}$ can be presented as the same form as Equation 2.2. The wave equation concerns both time and spatial variables. However, because of the linearity of this equation, fields of any arbitrary time dependence can be constructed from a linear superposition of harmonic solutions $\exp(-i\omega t)$, with ω the angular frequency, so that there is no loss of generality assuming that $\partial^2 \boldsymbol{E}/\partial (ct)^2 = -(\omega/c)^2 \boldsymbol{E}$, where c is the celerity of light in vacuum. Then, Equation 2.2 becomes the Helmholtz's equation:

$$\nabla^2 \boldsymbol{E} + \underline{n}^2 k_0^2 \ \boldsymbol{E} = \boldsymbol{0}, \tag{2.3}$$

where $k_0 = \omega/c$ is the angular wave number in vacuum ($k = \underline{n} k_0$ is the angular wave number in the medium of the optical index $\underline{n}$).

It has been proved by Hertz (1889) – for more information check Born and Wolf (2006) section 2.2.2 – that an electromagnetic field can be derived from a single vector function $\boldsymbol{\Pi}$, called *Hertz vector*, which satisfies (Stratton, 1941),

$$\nabla^2 \boldsymbol{\Pi} - \mu_0 \epsilon \frac{\partial^2 \boldsymbol{\Pi}}{\partial t^2} = \boldsymbol{0}. \tag{2.4}$$

Equation 2.4 is a second-order vector wave equation and for the same reason as above, we focus on its spatial dependence and consider the corresponding Helmholtz equation,

$$\nabla^2\mathbf{\Pi} + k^2\mathbf{\Pi} = \mathbf{0}. \tag{2.5}$$

Such an equation is impracticable in most cases, except for the situation of cylindrical and spherical symmetries (Stratton, 1941). However, it is known that Equations 2.4 and 2.5 are respectively equivalent to the following scalar wave equations:

$$\nabla^2\Psi + k^2\frac{\partial^2\Psi}{\partial t^2} = 0, \tag{2.6}$$

$$\nabla^2\psi + k^2\psi = 0 \qquad \text{with} \qquad \Psi = \psi\exp(-i\omega t) \tag{2.7}$$

The scalar function ψ is the spatial component of the function Ψ. The functions $\mathbf{\Pi}$ and $\mathbf{\Pi}^*$ are two independent solutions of Equation 2.7. If we introduce the *Debye's potentials* $\mathbf{\Pi}$ and $\mathbf{\Pi}^*$ such that $\mathbf{\Pi} = \boldsymbol{r}\Pi$ and $\mathbf{\Pi}^* = \boldsymbol{r}\Pi^*$, the electromagnetic field can be derived from $\mathbf{\Pi}$ and $\mathbf{\Pi}^*$ as follows:

$$\begin{cases} \boldsymbol{E} = \nabla\times(\Pi^*\boldsymbol{r}) + \dfrac{i}{c}\nabla\times\nabla\times(\Pi\boldsymbol{r}), \\ \boldsymbol{H} = -\underline{n}\nabla\times(\Pi\boldsymbol{r}) + \dfrac{i}{c}\nabla\times\nabla\times(\Pi^*\boldsymbol{r}). \end{cases} \tag{2.8}$$

The problem of solving the field is simplified into solving a scalar wave equation for given boundary conditions. Any linear combination of $\mathbf{\Pi}$ and $\mathbf{\Pi}^*$ is a solution of Equation 2.7.

I . 2 Solution of the scalar wave equation in spherical coordinates

Since a droplet is a sphere, the spherical coordinates (r, θ, ϕ) are the most convenient ones to form the solution of Equation 2.7. In this context, it is well known that the wave function can be expressed as the product of two independent functions:

$$\psi_\ell^{m_\ell}(r,\theta,\phi) = R_\ell(r)Y_\ell^{m_\ell}(\theta,\phi), \tag{2.9}$$

where $R_\ell(r)$ is the radial solution and $Y_\ell^{m_\ell}(\theta,\phi)$ the angular solution, *i.e.* the spherical harmonic,

$$Y_\ell^{m_\ell}(\theta,\phi)=\sqrt{\frac{2\ell+1}{4\pi}\frac{(\ell-m_\ell)!}{(\ell+m_\ell)!}}P_\ell^{m_\ell}(\cos\theta)\exp(im_\ell\phi), \tag{2.10}$$

where $P_\ell^{m_\ell}(\cos\theta)$ is the associated Legendre polynomials with the partial wave $\ell=0,\,1,\,2,\ldots$, and $m_\ell=0,\,\pm1,\,\ldots,\,\pm\ell$, $\forall\,\ell\in\mathbb{N}$. For $R_\ell(r)$, it is easy to show that it satisfies the second order differential equation,

$$\left[\frac{\mathrm{d}^2}{\mathrm{d}r^2}+\underline{n}^2k_0^2-\frac{\ell(\ell+1)}{r^2}\right]U_R(r)=0,\qquad\text{with}\quad U_R(r)=rR_\ell(r). \tag{2.11}$$

The radial and angular solutions are general forms. Particular solutions are obtained by using boundary conditions of the physical problem.

I.3 Mie theory

Mie theory (Mie, 1908) is a classical solution of Maxwell's equations (Equation 2.1) for the interaction of a plane monochromatic wave with a homogeneous dielectric sphere. It is the case, at least to a first approximation, of a pure water droplet. Boundary conditions are expressed at the droplet interface , *i.e.* at $r=r_d$ where r_d is the droplet radius. Here, from the Maxwell's equations, the boundaries condition are that the tangential and normal components of $\boldsymbol{E}$ and $\boldsymbol{B}$ be continuous at $r=r_d$. To satisfy such boundaries condition, it is necessary to assume that, apart from the incident field $(\boldsymbol{E}_i\,,\ \boldsymbol{B}_i)$ and the field $(\boldsymbol{E}_w\,,\ \boldsymbol{B}_w)$ within the sphere, there is a scattered field $(\boldsymbol{E}_s\,,\ \boldsymbol{B}_s)$ outside the sphere. Then:

$$\text{outside the sphere:}\begin{cases}\boldsymbol{E}=\boldsymbol{E}_i+\boldsymbol{E}_s,\\ \boldsymbol{B}=\boldsymbol{B}_i+\boldsymbol{B}_s.\end{cases}\qquad\text{inside the sphere:}\begin{cases}\boldsymbol{E}=\boldsymbol{E}_w,\\ \boldsymbol{B}=\boldsymbol{B}_w.\end{cases} \tag{2.12}$$

In the spherical coordinates, it means that $E_\theta\,,\ E_\phi\,,\ E_r\,,\ B_\theta\,,\ B_r$ and B_ϕ are continuous at the interface $r=r_d$. It is not difficult to obtain the fields given by the Mie theory, but it is quite long. A comprehensive and clear demonstration is available in Born and Wolf (2006). It consists in separating the Debye's potential into an electrical part ${}^e\Pi$ and a magnetic part ${}^m\Pi$ from which the electromagnetic field can be derived; introducing $\alpha=\beta\epsilon$ where $\beta=i\omega$, one has:

$$\begin{cases} E_r &= \dfrac{\partial^2(r^e\Pi)}{\partial^2 r} + k^2(r^e\Pi), \\ E_\theta &= \dfrac{1}{r}\dfrac{\partial^2(r^e\Pi)}{\partial r\partial\theta} + \mu_0\beta\dfrac{1}{r\sin\theta}\dfrac{\partial(r^m\Pi)}{\partial\phi}, \\ E_\phi &= \dfrac{1}{r\sin\theta}\dfrac{\partial^2(r^e\Pi)}{\partial r\partial\phi} - \mu_0\beta\dfrac{1}{r}\dfrac{\partial(r^m\Pi)}{\partial\theta}, \end{cases} \tag{2.13}$$

$$\begin{cases} B_r &= \mu_0\dfrac{\partial^2(r^m\Pi)}{\partial^2 r} + k^2(r^m\Pi), \\ B_\theta &= -\mu_0\alpha\dfrac{1}{r\sin\theta}\dfrac{\partial(r^e\Pi)}{\partial\phi} + \dfrac{1}{r}\dfrac{\partial^2(r^m\Pi)}{\partial r\partial\theta}, \\ B_\phi &= \mu_0\alpha\dfrac{1}{r}\dfrac{\partial(r^e\Pi)}{\partial\theta} + \dfrac{1}{r\sin\theta}\dfrac{\partial^2(r^m\Pi)}{\partial r\partial\phi}. \end{cases} \tag{2.14}$$

Considering the boundaries condition, we get the following expressions of the Debye's potentials $({}^e\Pi_i,\ {}^m\Pi_i)$ for the incident field, $({}^e\Pi_s,\ {}^m\Pi_s)$ for the scattered field and $({}^e\Pi_w,\ {}^m\Pi_w)$ for the internal field.

$$\begin{cases} {}^e\Pi_i &= \dfrac{1}{rk_0^2}\displaystyle\sum_{\ell=1}^{\infty} i^{\ell-1}\dfrac{2\ell+1}{\ell(\ell+1)}\,\psi_\ell(k_0r)P_\ell^{(1)}(\cos\theta)\cos\phi, \\ {}^m\Pi_i &= \dfrac{1}{rk_0\mu_0\omega}\displaystyle\sum_{\ell=1}^{\infty} i^{\ell}\dfrac{2\ell+1}{\ell(\ell+1)}\,\psi_\ell(k_0r)P_\ell^{(1)}(\cos\theta)\sin\phi, \\ \\ {}^e\Pi_s &= \dfrac{1}{rk_0^2}\displaystyle\sum_{\ell=1}^{\infty} A_\ell\,\zeta_\ell(k_0r)P_\ell^{(1)}(\cos\theta)\cos\phi, \\ {}^m\Pi_s &= \dfrac{1}{rk_0\mu_0\omega}\displaystyle\sum_{\ell=1}^{\infty} B_\ell\,\zeta_\ell(k_0r)P_\ell^{(1)}(\cos\theta)\sin\phi, \\ \\ {}^e\Pi_w &= \dfrac{1}{rk^2}\displaystyle\sum_{\ell=1}^{\infty} C_\ell\,\psi_\ell(kr)P_\ell^{(1)}(\cos\theta)\cos\phi, \\ {}^m\Pi_w &= \dfrac{1}{rk\mu_0\omega}\displaystyle\sum_{\ell=1}^{\infty} D_\ell\,\psi_\ell(kr)P_\ell^{(1)}(\cos\theta)\sin\phi. \end{cases} \tag{2.15}$$

Introducing $x = k_0r_d$ (size parameter), the coefficients A_ℓ, B_ℓ, C_ℓ and D_ℓ are given by:

$$A_\ell = i^{\ell+1}\frac{2\ell+1}{\ell(\ell+1)}\frac{\underline{n}\psi'_\ell(x)\psi_\ell(\underline{n}x) - \psi_\ell(x)\psi'_\ell(\underline{n}x)}{\underline{n}\zeta'_\ell(x)\psi_\ell(\underline{n}x) - \zeta_\ell(x)\psi'_\ell(\underline{n}x)}$$

$$B_\ell = i^{\ell+1}\frac{2\ell+1}{\ell(\ell+1)}\frac{\underline{n}\psi'_\ell(\underline{n}x)\psi_\ell(x) - \psi_\ell(\underline{n}x)\psi'_\ell(x)}{\underline{n}\psi'_\ell(\underline{n}x)\zeta_\ell(x) - \psi_\ell(\underline{n}x)\zeta'_\ell(x)}$$

$$C_\ell = i^{\ell-1}\frac{2\ell+1}{\ell(\ell+1)}\frac{\underline{n}\psi'_\ell(x)\zeta_\ell(x) - \underline{n}\psi_\ell(x)\zeta'_\ell(x)}{\psi'_\ell(nx)\zeta_\ell(x) - n\psi_\ell(nx)\zeta_\ell(x)}$$

$$D_\ell = i^{\ell-1}\frac{2\ell+1}{\ell(\ell+1)}\frac{\underline{n}\psi'_\ell(x)\zeta_\ell(x) - \underline{n}\psi_\ell(x)\zeta'_\ell(x)}{n\psi'_\ell(\underline{n}x)\zeta_\ell(x) - \psi_\ell(\underline{n}x)\zeta'_\ell(x)}.$$

In these equations, ψ_ℓ, χ_ℓ and ζ_ℓ are the Riccati-Bessel functions (Watson, 1995):

$$\psi_\ell(z) = \sqrt{\frac{\pi z}{2}}\,J_{\ell+1/2}(z), \quad \chi_\ell(z) = -\sqrt{\frac{\pi z}{2}}\,N_{\ell+1/2}(z)$$

and

$$\zeta_\ell(z) = \psi_\ell(z) - i\,\chi_\ell(z) = \sqrt{\frac{\pi z}{2}}\,H^{(1)}_{\ell+1/2}(z).$$

where $J_{\ell+1/2}(z)$ is the *Bessel* function, $N_{\ell+1/2}(z)$ the *Neumann* function and $H^{(1)}_{\ell+1/2}(z)$ the first *Hankel* function. The total Debye's potentials ${}^e\Pi$ and ${}^m\Pi$ are then:

$${}^e\Pi = {}^e\Pi_i + {}^e\Pi_s + {}^e\Pi_w \qquad \text{and} \qquad {}^m\Pi = {}^m\Pi_i + {}^m\Pi_s + {}^m\Pi_w. \tag{2.16}$$

I.4 The cross sections

Cross sections are of fundamental importance to calculate the scattered and absorbed light by a sphere and derived quantities of practical importance such as the cloud optical thickness COT (will be fairly detailed in the section III.).

The concept of cross sections can be explained in a very simple way – as my prof Olivier Pujol explained to me: in Figure 2.1, there is a swimming pool full of fishes, so in order to eat my lunch i had to go fishing with a landing net. The fishes I got in my landing net are **absorbed** (σ_a) and the fishes that touched the landing net and changed their direction are **scattered** (σ_s). If we compare the number of absorbed fishes and scattered fishes to the incident number of fishes, we got what is called the absorption and scattering cross sections respectively, (σ_a) and (σ_s). The number of fishes that head to the detector (presented by my prof, supposed to remain at the same vertical level) gives the extinction cross sections: $\sigma_e = \sigma_a + \sigma_s$. Precisely, σ_e is the number of fishes that are subtracted from the incident

beam fishes direction. As the dimension and the type of the landing net will affect the amount of the caught and deviated fishes, as the dimension and the type of the sphere will affect the absorbed and scattered light.

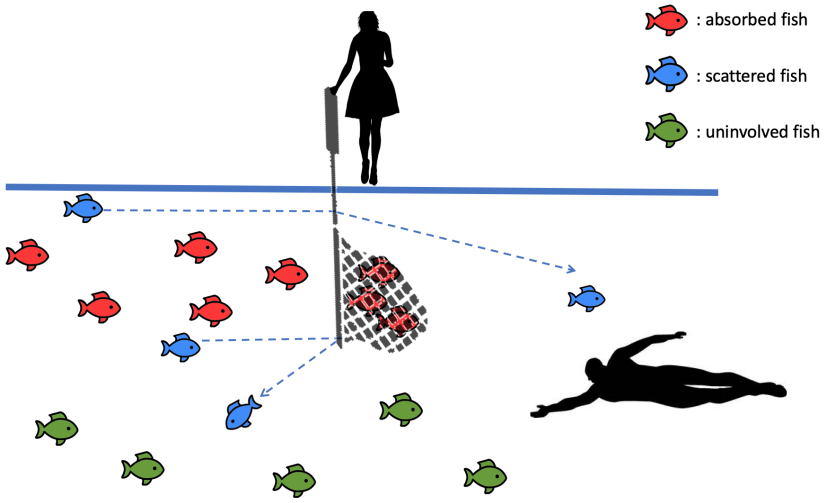

Figure 2.1: Scheme presenting the absorbed, scattered and extincted fishes, where the fishes are used to symbolize the concept of the cross section that depends on the dimension and type of landing net.

To get the cross section formulas, one has to evaluate and integrate in all directions the Poynting's vector $\boldsymbol{S} = \boldsymbol{E} \times \boldsymbol{B}/\mu_0$. The integrals are expressed with the coefficients ${}^{e}B_\ell$ and ${}^{m}B_\ell$ with the benefit of the orthogonality between the associated Legendre functions. The two coefficients ${}^{e}B_\ell$ and ${}^{m}B_\ell$ are given by:

$$ {}^{e}B_\ell = i^{\ell+1}\frac{2\ell+1}{\ell(\ell+1)}\frac{\underline{n}\psi'_\ell(x)\psi_\ell(\underline{n}x) - \psi_\ell(x)\psi'_\ell(\underline{n}x)}{\underline{n}\zeta_\ell^{(1)'}(x)\psi_\ell(\underline{n}x) - \underline{n}\zeta_\ell^{(1)}(x)\psi'_\ell(\underline{n}x)} \tag{2.17} $$

$$ {}^{m}B_\ell = i^{\ell+1}\frac{2\ell+1}{\ell(\ell+1)}\frac{\underline{n}\psi_\ell(x)\psi'_\ell(\underline{n}x) - \psi'_\ell(x)\psi_\ell(\underline{n}x)}{\underline{n}\zeta_\ell^{(1)}(x)\psi'(\underline{n}x) - \underline{n}\zeta_\ell^{(1)'}(x)\psi_\ell(\underline{n}x)} \tag{2.18} $$

with $x = k_0 r_d$; the prime superscript ($'$) indicates the first derivative with respect to the argument. The averaged Poynting's vector represents the time-averaged flow of light energy:

$$ \langle \boldsymbol{S} \rangle = \frac{1}{2\mu_0}\mathrm{Re}\{\underline{\boldsymbol{E}}(\boldsymbol{r}) \times \underline{\boldsymbol{B}}(\boldsymbol{r})\} \tag{2.19} $$

Equation 2.20 represents the combination between the two Equations 2.12 and 2.19:

$$\langle \boldsymbol{S} \rangle = \langle \boldsymbol{S}^{(i)} \rangle + \langle \boldsymbol{S}^{(s)} \rangle + \langle \boldsymbol{S}^{(a)} \rangle \tag{2.20}$$

where $\langle \boldsymbol{S}^{(i)} \rangle$ is the Poynting vector for the incident field, $\langle \boldsymbol{S}^{(a)} \rangle$ is for absorption, $\langle \boldsymbol{S}^{(s)} \rangle$ concerns the scattering and $\langle \boldsymbol{S}^{(e)} \rangle$ is for extinction:

$$\langle \boldsymbol{S}^{(i)} \rangle = \frac{1}{2\mu_0} \mathrm{Re}\Big\{ \underline{\boldsymbol{E}}^{(i)}(\boldsymbol{r}) \times \Big[\underline{\boldsymbol{B}}^{(i)}(\boldsymbol{r}) \Big]^* \Big\} \tag{2.21}$$

$$\langle \boldsymbol{S}^{(s)} \rangle = \frac{1}{2\mu_0} \mathrm{Re}\Big\{ \underline{\boldsymbol{E}}^{(s)}(\boldsymbol{r}) \times \Big[\underline{\boldsymbol{B}}^{(s)}(\boldsymbol{r}) \Big]^* \Big\} \tag{2.22}$$

$$\langle \boldsymbol{S}^{(e)} \rangle = \frac{1}{2\mu_0} \mathrm{Re}\Big\{ \underline{\boldsymbol{E}}^{(i)}(\boldsymbol{r}) \times \Big[\underline{\boldsymbol{B}}^{(s)}(\boldsymbol{r}) \Big]^* + \underline{\boldsymbol{E}}^{(s)}(\boldsymbol{r}) \times \Big[\underline{\boldsymbol{B}}^{(i)}(\boldsymbol{r}) \Big]^* \Big\} \tag{2.23}$$

The Poynting vector is related to the net flow energy per second over the surface of a sphere which is equal to the integral of the radial part $\langle S \rangle_r$ of $\langle S \rangle$. Then, from Equation 2.20:

$$-\mathcal{W}^{(a)} = \mathcal{W}^{(i)} + \mathcal{W}^{(s)} + \mathcal{W}^{(e)} \tag{2.24}$$

where $\mathcal{W}^{(a)}, \mathcal{W}^{(i)}, \mathcal{W}^{(s)}$ and $\mathcal{W}^{(e)}$ are the integrals, over the surface of the droplet, of the radial components of $\langle S^{(a)} \rangle_r$, $\langle S^{(i)} \rangle_r, \langle S^{(s)} \rangle_r$ and $\langle S^{(e)} \rangle_r$. Since the surrounding of the droplet is dielectric, $\mathcal{W}^{(i)}$ is equal to zero; so $\mathcal{W}^{(a)} + \mathcal{W}^{(s)} = -\mathcal{W}^{(e)}$ with

$$-\mathcal{W}^{(e)} = \frac{1}{2\mu_0} \mathrm{Re} \int\int_S \Big[\underline{\boldsymbol{E}}^{(i)}(\boldsymbol{r}) \times \Big(\underline{\boldsymbol{B}}^{(s)}(\boldsymbol{r}) \Big)^* + \underline{\boldsymbol{E}}^{(s)}(\boldsymbol{r}) \times \Big(\underline{\boldsymbol{B}}^{(i)}(\boldsymbol{r}) \Big)^* \Big] \boldsymbol{n} \cdot \, \mathrm{d}S$$

$\boldsymbol{n}$ is the normal to the surface of integration. After identifying each element $\langle S \rangle$ and $\mathcal{W}$ for extinction, scattering and absorption, the cross sections are given by:

$$\sigma_s = \frac{\mathcal{W}^{(s)}}{|\langle S^{(i)} \rangle|} \qquad \sigma_a = \frac{\mathcal{W}^{(a)}}{|\langle S^{(i)} \rangle|}$$

Whilst, the absorption cross section is presented as $\sigma_a = \sigma_e - \sigma_s$, the final forms of σ_e and σ_s as a function of ${}^{e}B_\ell$ and ${}^{m}B_\ell$, ℓ and k_0, are:

$$\begin{aligned} \sigma_e &= \frac{2\pi}{k_0^2} \mathrm{Re} \sum_\ell (-i)^{\ell+1} \ell(\ell+1)({}^{e}B_\ell + {}^{m}B_\ell) \\ \sigma_s &= \frac{2\pi}{k_0^2} \sum_\ell \frac{\ell^2(\ell+1)^2}{2\ell+1} (|{}^{e}B_\ell|^2 + |{}^{m}B_\ell|^2) \end{aligned} \tag{2.25}$$

I.5 Natural light intensity

Another physical quantity is calculated through ${}^{e}B_{\ell}$ and ${}^{m}B_{\ell}$: the scattering of natural light $I^{(s)}$, a very basic but important element in atmospheric optics that is linked to the power of the electromagnetic radiation field. $I^{(s)}$ is divided into two components:

$$I_{\perp}^{(s)} = \frac{1}{k_0^2 r^2}\left|\sum_{\ell=1}^{\infty}(-i)^{\ell}\left({}^{e}B_{\ell}\frac{P_{\ell}^{(1)}(\cos\theta)}{\sin\theta} - {}^{m}B_{\ell}P_{\ell}^{(1)'}(\cos\theta)\sin\theta\right)\right|^2 \tag{2.26}$$

$$I_{\parallel}^{(s)} = \frac{1}{k_0^2 r^2}\left|\sum_{\ell=1}^{\infty}(-i)^{\ell}\left({}^{e}B_{\ell}P_{\ell}^{(1)'}(\cos\theta)\sin\theta - {}^{m}B_{\ell}\frac{P_{\ell}^{(1)}(\cos\theta)}{\sin\theta}\right)\right|^2 \tag{2.27}$$

with

$$\left|E_{\theta}^{(s)}\right|^2 = I_{\parallel}^{(s)}\cos^2\phi \qquad \left|E_{\phi}^{(s)}\right|^2 = I_{\perp}^{(s)}\sin^2\phi \tag{2.28}$$

The scattering light is presented as: $I^{(s)} = \frac{1}{2}(I_{\perp}^{(s)} + I_{\parallel}^{(s)})$.
It is worth mentioning that dealing with scattering, the detector of light is placed far away from the scatterer ($r \gg D$), so that the radial component of the electromagnetic field are negligible with respect to the two other components.

II. TUNNELING OPTICAL RESONANCE – TOR

II.1 Effective potential energy

The radial wave equation presented in Equation 2.11 is formally analogous to the one dimension Schrödinger's equation by introducing the effective potential energy $\mathcal{E}_{p,ef}$ and the energy $\mathcal{E} = k_0/\hbar c$:

$$\left[\frac{\mathrm{d}^2}{\mathrm{d}r^2} - k_0^2\left(\frac{\mathcal{E}_{p,ef}}{\mathcal{E}} - 1\right)\right]U_R(r) = 0, \qquad \text{with} \qquad \mathcal{E}_{p,ef} = (1-\underline{n}^2)\mathcal{E} + \frac{\ell(\ell+1)}{k_0^2 r^2}\mathcal{E} \tag{2.29}$$

Therefore, $\mathcal{E}_{p,ef}$ is the sum of two terms: the r-independent constant term $(1-\underline{n}^2)\mathcal{E}$, and the "centrifugal" term $\ell(\ell+1)\mathcal{E}/(k_0^2 r^2)$. Due to this formal identity, the light-droplet interaction (radial part precisely) can be considered as a 1D problem of a quantum object of energy $\mathcal{E}$ and wave function $U_R(r)$, under the field of $\mathcal{E}_{p,ef}$.
The specific point of this problem, compared to similar problems in quantum mechanics, is that $\mathcal{E}_{p,ef}$ depends on the characteristics of the incident wave ($\mathcal{E}$ or k_0 and ℓ) and

on the droplet $(D\ ,\ \underline{n})$, $\underline{n}$ being dependent on $\mathcal{E}$ (Hale and Querry, 1973). This is why light-droplet interaction is considered as a morphology-dependent scattering problem.
Figure 2.2 is a sketch of $\mathcal{E}_{p,ef}/\mathcal{E}$ and its two components. The circle represents a droplet of radius r_d with n as the refractive index. The interval $[0, r_d]$ locates the center of the droplet at $(r = 0)$ till the droplet radius $(r = r_d)$, referring to *"inside the droplet"*. The interval $]r_d, \infty[$ is the *"outside the droplet"* with n_{air} as refractive index .
The red plot represents the first term of $\mathcal{E}_{p,ef}/\mathcal{E} : 1 - n^2$, a constant term for the inside the droplet, and equal to zero for the outside since $n = n_{air} \approx 1$. Note that for the sketch, the optical index of the droplet has been considered as being $n = 1.33$.
The blue plot is the centrifugal term $\ell(\ell+1)/k_0^2 r^2$ that decreases with the increment of r till zero for $r \to \infty$. The black plot is the sum of the two plots.

Figure 2.3 represents some additional information on the $\mathcal{E}_{p,ef}/\mathcal{E}$, as we can see clearly this ratio exhibit a potential well at $r = r_d$ with two particular energies: $\mathcal{E}_H$ stands for energy of the top of the well and $\mathcal{E}_L$ stands for the energy of the bottom of the well.

This plot is commonly divided into two zones, known as the below-edge zone $[\mathcal{E}_H\,, +\infty[$ and the above-edge zone $]-\infty\,, \mathcal{E}_H]$. If the incident energy is situated in the potential well $]\,\mathcal{E}_L\,, \mathcal{E}_H\,[$ *i.e.* in the above-edge zone, the droplet can absorb light by tunneling and excite some resonances; this is what we call the **tunneling optical resonance TOR**. Envisioned, in this way, light interaction with matter by tunneling is quite obvious.

Some remarks on *the variation of* $\mathcal{E}_{p,ef}/\mathcal{E}$ are built on the mathematical form of the Equation 2.29 presented as followed:

(a) in function of ℓ : if $\ell \nearrow$: $\quad (1-n^2) + \dfrac{\ell(\ell+1)\nearrow}{k_0^2 r^2} = \mathcal{E}_{p,ef}/\mathcal{E}\nearrow$

(b) in function of r : if $r \nearrow$: $\quad (1-n^2) + \dfrac{\ell(\ell+1)}{k_0^2 r^2 \nearrow} = \mathcal{E}_{p,ef}/\mathcal{E}\searrow$

(c) in function of n : if $n \nearrow$: $\quad (1-n^2)\searrow + \dfrac{\ell(\ell+1)}{k_0^2 r^2} = \mathcal{E}_{p,ef}/\mathcal{E}\nearrow$

(d) in function of frequency ν :

$$\text{if } \nu \nearrow : \qquad (1-n^2) + \frac{\ell(\ell+1)}{k_0^2 r^2} = (1-n^2) + \frac{c^2}{4\pi^2 \nu^2 \nearrow}\frac{\ell(\ell+1)}{r^2} = \mathcal{E}_{p,ef}/\mathcal{E}\searrow$$

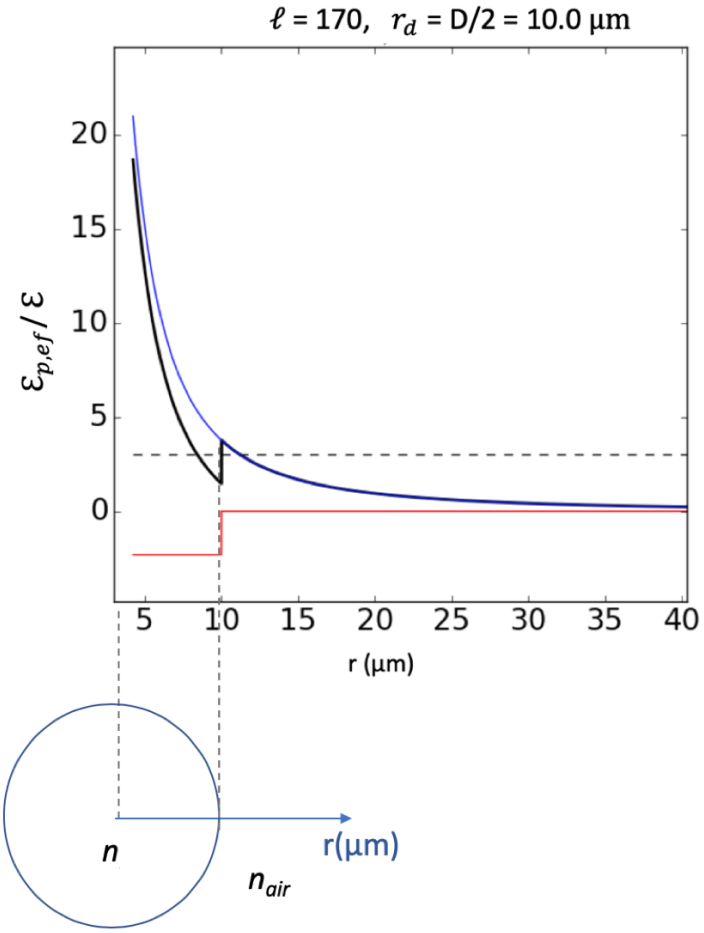

Figure 2.2: For an incident energy $\mathcal{E} = 3.0$ eV represented by the gray dashed line, for a droplet – symbolized by the circle – with $r_d = 10\mu$m and $\ell = 170$, the blue plot represents the $\ell(\ell+1)/k_0^2 r^2$ component of $\mathcal{E}_{p,ef}/\mathcal{E}$ and the red plot represents the term $1 - n^2$. The black curve ($\mathcal{E}_{p,ef}/\mathcal{E}$) is the sum of the blue and red plots.

Important characteristics of $\mathcal{E}_{p,ef}$ for a given set of $\mathcal{E}$, ℓ, D are:

1. The *well depth* Δ. At the top of the potential well, $\mathcal{E}_{p,ef} = \ell(\ell+1)k_0^2 r_d^2$, and at the bottom $\mathcal{E}_{p,ef} = 1 - n^2 + \ell(\ell+1)/k_0^2 r_d^2$. The well depth ($\Delta$) is the subtraction of those two elements so $\Delta = (n^2 - 1)\mathcal{E}$

2. The *barrier thickness* e is obtained from $\mathcal{E}_{p,ef}/\mathcal{E} = 1$, so the Equation 2.29 would be written as follow:

$$\frac{\mathcal{E}_{p,ef}}{\mathcal{E}} = 1 - n^2 + \frac{\ell(\ell+1)}{k_0^2 r^2} \quad \text{where} \quad k_0 = \frac{\mathcal{E}}{\hbar c}$$

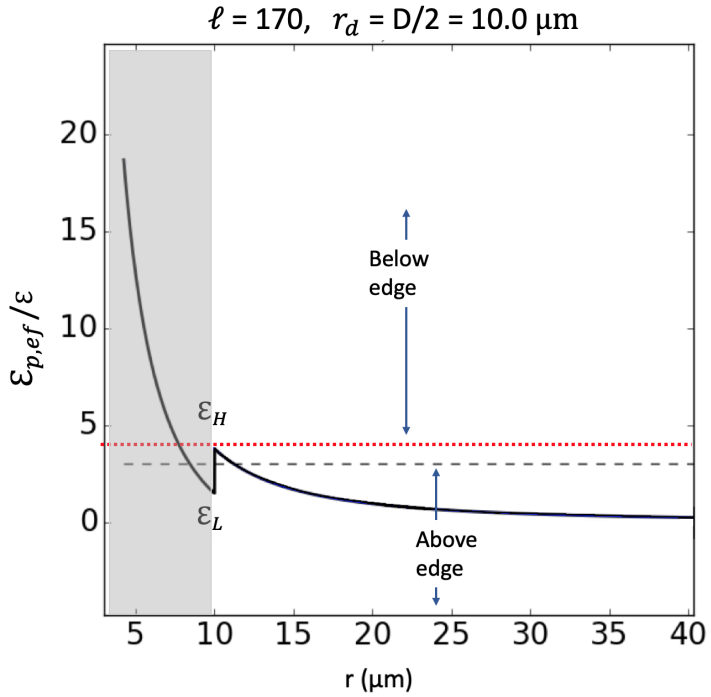

Figure 2.3: The effective potential energy for incident energy $\mathcal{E} = 3.0$ eV – presented by the gray dashed line, $r_d = 10\mu$m and $\ell = 170$. The red dots separate the below-edge from the above-edge zone. The gray rectangle represents the inside of the droplet ($r < r_d$)

There are two solutions for this equation: one (r_0) is for $r < r_d$ and the second (r_2) is for $r > r_d$. Since $r_2 > r_d$, it means the optical index is equal to $n_{air} = 1$. Thus:

$$\begin{cases} n^2 = \dfrac{\hbar^2 c^2 \ell(\ell+1)}{\mathcal{E}^2 r_0^2} & \text{for} \quad r < r_d \\ 1 = \dfrac{\hbar^2 c^2 \ell(\ell+1)}{\mathcal{E}^2 r_2^2} & \text{for} \quad r > r_d \end{cases}$$

This leads to $r_0 = \hbar c\sqrt{\ell(\ell+1)}/(\mathcal{E}n)$ and $r_2 = \hbar c\sqrt{\ell(\ell+1)}/\mathcal{E}$. The barrier thickness is $e = r_2 - r_d = \hbar c/\mathcal{E}\sqrt{\ell(\ell+1)} - r_d$

3. The energy interval $[\mathcal{E}_H, \mathcal{E}_L]$ for which tunneling is expected. One gets the formula of $\mathcal{E}_H$ and $\mathcal{E}_L$ by replacing respectively r_2 by r_d and r_0 by r_d. It ensues:

$$\mathcal{E}_H = \frac{2\hbar c\,[\ell(\ell+1)]^{1/2}}{r_d} \qquad \mathcal{E}_L = \frac{\mathcal{E}_H}{n} \tag{2.30}$$

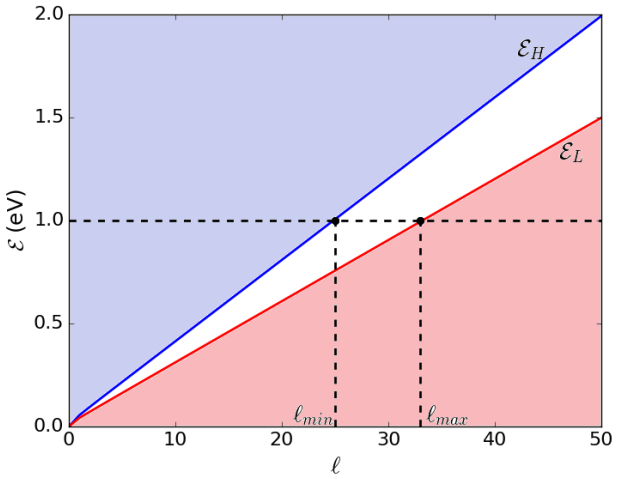

Figure 2.4: Variation of top well and bottom well energies ($\mathcal{E}_H$ and $\mathcal{E}_L$) *vs.* ℓ for $r_d = 10\mu$m and $n = 1.33$

Figure 2.4 gives the variation of $\mathcal{E}_H$ and $\mathcal{E}_L$ within the variation of ℓ for an incident wave energy $\mathcal{E} = 1\,$eV interacting with a droplet of radius $r_d = D/2 = 10\mu$m . The incident wave energy, presented by the horizontal dashed line, intersects with $\mathcal{E}_H$ at $\ell = \ell_{min}$ and with $\mathcal{E}_L$ at $\ell = \ell_{max}$. It ensues that $[\ell_{min}, \ell_{max}]$ is the interval for which TOR can occur (highlighted by the white area in the Figure 2.4).

The blue area $(\mathcal{E} > \mathcal{E}_H)$ corresponds to ℓ-value ($\ell < \ell_{min}$) for which light can enter the droplet by classical refraction while the red area $\mathcal{E} < \mathcal{E}_L$ corresponds to ℓ-value $(\ell > \ell_{max})$ with no light-droplet interaction at all.

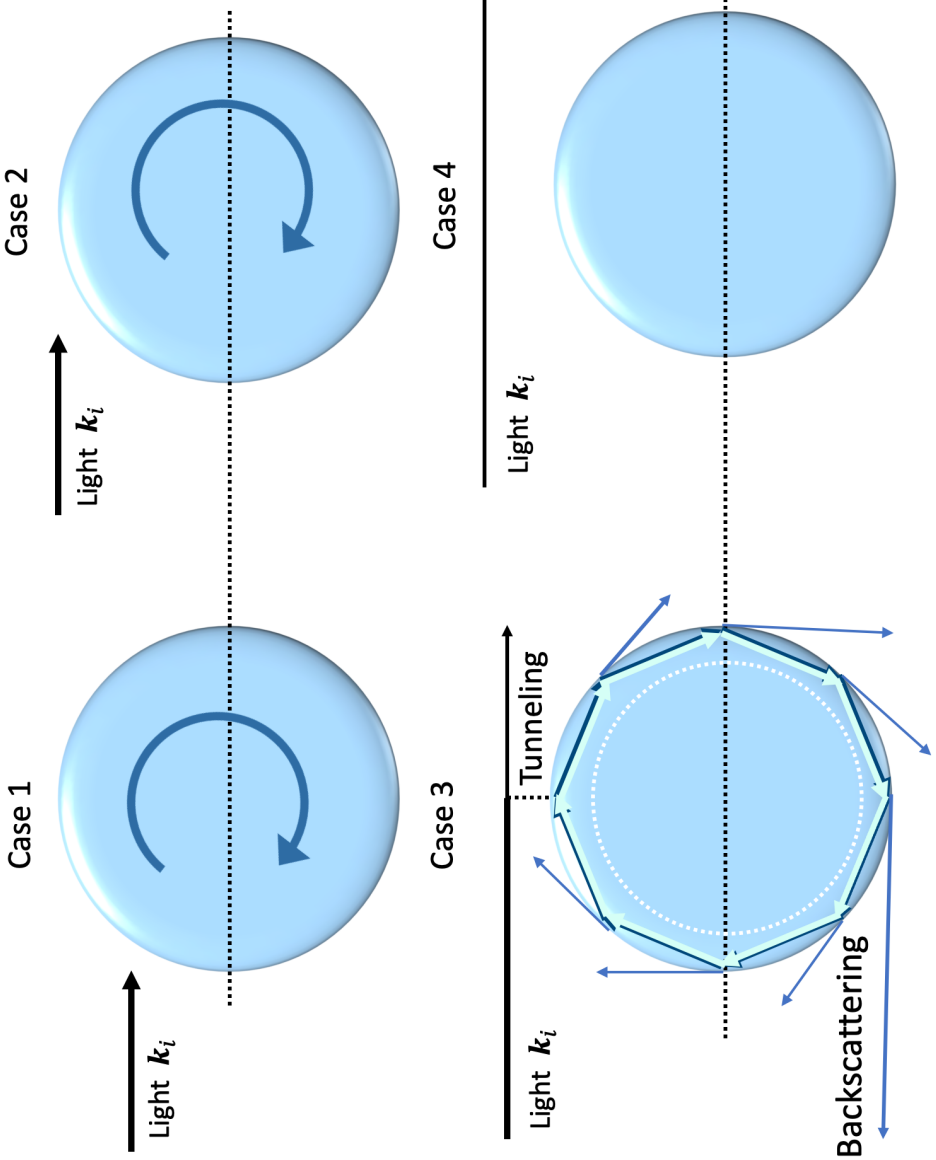

Figure 2.5: The below-edge zone is presented in case (1) and (2) where light can penetrate the droplet (blue sphere) by refraction. Case (3) presents an above-edge situation where light penetrates the droplet by tunneling. The light blue arrow presents a reflected ray inside the droplet and the dark blue arrow presents the refracted rays forming a surface wave, where the forth refracted ray, in this case, is the back-scattered light. The white dots represents the layer in which light is confined (*whispering gallery mode*). Case (4) is an above-edge zone where no absorption is possible.

From the point of view of Newtonian physics, an object with an energy lower than $\mathcal{E}_H$ is not able to overcome the barrier near the interface, whereas in the wave theory, light is able to penetrate the barrier by tunneling, according to the values of D, ℓ, and $\mathcal{E}$.

Figure 2.5 gives a schematic representation of the light interaction according to the ratio $\mathcal{E}/\mathcal{E}_H$. Light, in case 1, is a below-edge case $(\mathcal{E} < \mathcal{E}_H)$, governed by: $\ell < \ell_{min}$. Light "hits" the droplet and refracts to the inside.

The light in case 2 is also a below-edge case, governed by the same properties as the first case $(\ell < \ell_{min}$ and $\mathcal{E} < \mathcal{E}_H)$. This ray "hits" tangentially the droplet and refracts to the inside. Consequently, in the below-edge zone, the light is in direct interaction with the droplet.

The cases 3 and 4 are both above-edge rays. Light in case 3 is close enough to the droplet that it may enter the droplet by tunneling, the ray reflects many times (represented in light blue narrow – inside the droplet) and refracts as a surface wave (presented in dark blue narrow – outside the droplet), where the forth dark blue narrow represents the back-scattered light (scattering angle $\theta = 180°$). The light inside the droplet is confined in a small circle layer (white dots) just below the droplet interface, such mode of resonance are called "*whispering gallery mode*".

Light of case 4 is far away from the droplet, therefore no interaction can occur in this case.

II.2 Scattering amplitude

Scattering by a central interaction, *i.e.* only r- dependent and of $\mathcal{O}(r^{-2})$, as it is the case here, can be efficiently addressed by means of the partial-wave analysis method. This technique is largely used in Physics, *e.g.* to investigate particle collisions as nuclear scattering (Hodgson, 1963), and as we will show hereafter, it is also simple and effective in the present context of light-droplet interaction in atmospheric Optics. In what follows, only the most important results of this method are presented – those useful for atmospheric optics – since many details can be found in standard physics textbooks (Schiff, 1955; Messiah, 1959; Taylor, 1972; Landau and Lifshitz, 1981; Valentin, 1982; Cohen-Tannoudji et al., 1997).

At far distances from the scatterer, the (stationary) wave-function can be written as:

$$\underline{\psi}_{k_0}(r) \propto \exp(ik_0 z) + \underline{f}_{k_0}(\theta)\,\frac{\exp(ik_0 r)}{r} \tag{2.31}$$

where $\exp(ik_0 z)$ represents the incident wave-function and $\underline{f}_{k_0}(\theta)\,\exp(ik_0 r)/r$ is the scattered wave-function. The factor $\underline{f}_{k_0}$ is the amplitude of the scattered light, and also called by

phase function in atmospheric optics.
The asymptotic form ($r \to \infty$) of $\underline{\psi}_{k_0}(r)$ as introduced in Messiah (1959):

$$\underline{\psi}_{k_0}(r) = \sum_{\ell=0}^{\infty} \underline{a}_\ell(k_0) \frac{\sin[k_0 r + \Phi_\ell(k_0)]}{r} P_\ell(\cos\theta) \tag{2.32}$$

where $\Phi_\ell(k_0) = -\ell\pi/2 + \delta_\ell(k_0)$ with δ_ℓ the phase shift and $\underline{a}_\ell$ a coefficient to be determined afterward. These two parameters characterize the interaction (*i.e.* he scattering process) and so the influence of $\mathcal{E}_{p,ef}$. By definition, the square module of the scattering amplitude $\underline{f}_{k_0}$ is equal to the differential cross section of scattering:

$$\sigma_s(\theta) = |\underline{f}_{k_0}(\theta)|^2 \tag{2.33}$$

The total cross section (σ) is then obtained from the optical theorem:

$$\sigma = \frac{4\pi}{k_0} \mathrm{Im}\{\underline{f}_{k_0,\,\ell}(0)\} \tag{2.34}$$

where Im stands for the imaginary part. It can be useful to introduce partial quantities, *i.e.* relative to the wave order ℓ , like the partial scattering amplitude $\underline{f}_{\ell,k_0}(\theta)$ and the partial total cross section σ_ℓ such that:

$$\underline{f}_{k_0}(\theta) = \sum_{\ell} \underline{f}_{\ell,k_0} P_\ell(\cos\theta) \quad \text{and} \quad \sigma = \sum_{\ell} \sigma_\ell \tag{2.35}$$

The second sum over ℓ is due to the orthogonality of the partial scattering amplitudes.
Going back to Equation 2.31: the first element of the equality is presented by

$$\exp(ik_0 z) = \sum_{\ell} \beta_\ell j_\ell(k_0 r) P_\ell(\cos\theta)$$

with $j_\ell(k_0 r)$ is the spherical Bessel functions and β_ℓ a coefficient represented as $(2\ell+1)i^\ell$ since $j_\ell(k_0 r)_{r\to\infty} = \sin(k_0 r - \ell\pi/2)/k_0 r$, it follows:

$$\exp(ik_0 z) = \frac{1}{k_0 r} \sum_{\ell=0}^{\infty} (2\ell+1) i^\ell \sin\left(k_0 r - \frac{\ell\pi}{2}\right) P_\ell(\cos\theta)$$

Combining Equation 2.31 and the final form of $\exp(ik_0z)$, one gets:

$$\exp(ik_0z) + \underline{f}_{\ell,k_0}(\theta)\frac{\exp(ik_0r)}{r} = \sum_{\ell=0}^{\infty}\left[(2\ell+1)i^{\ell}j_{\ell}(k_0r) + \underline{f}_{\ell,k_0}\frac{\exp(ik_0r)}{r}\right]P_{\ell}(\cos\theta) \quad (2.36)$$

Since Equation 2.32 is equal to Equation 2.36, the first element of the equality of the previous equation, is written:

$$\sum_{\ell=0}^{\infty}\underline{a}_{\ell}\frac{\sin(k_0r - \ell\pi/2 + \delta_{\ell})}{r}P_{\ell}(\cos\theta) = \sum_{\ell=0}^{\infty}\left[(2\ell+1)i^{\ell}j_{\ell}(k_0r) + \underline{f}_{\ell,k_0}\frac{\exp(ik_0r)}{r}\right]P_{\ell}(\cos\theta)$$

and by comparing the two expressions, it follows:

$$\underline{a}_{\ell} = i^{\ell}\,\frac{2\ell+1}{k_0}\exp(i\delta_{\ell}) \quad \text{and} \quad \underline{f}_{\ell,k_0} = \frac{2\ell+1}{k_0}\exp(i\delta_{\ell})\sin\delta_{\ell} \quad (2.37)$$

So, by substituting $\underline{f}_{\ell,k_0}(\theta)$ to the Equation 2.35, the term of the scattering amplitude $\underline{f}_{k_0}(\theta)$ is written as:

$$\underline{f}_{k_0}(\theta) = \frac{1}{k_0}\sum_{\ell=0}^{\infty}(2\ell+1)\exp(i\delta_{\ell})\sin\delta_{\ell}P_{\ell}(\cos\theta) \quad (2.38)$$

The cross section of ℓ for elastic diffusion is illustrated by the following equation:

$$\sigma_{\ell} = \frac{4\pi}{k_0^2}(2\ell+1)\sin^2\delta_{\ell} \quad (2.39)$$

This phase shift, which characterizes the influence of $\mathcal{E}_{p,ef}$ and so the scattering process, can be written in function of δ_{ℓ}^{bg} and δ_{ℓ}^{res}, respectively a background contribution and the resonant part:

$$\delta_{\ell} = \delta_{\ell}^{bg} + \delta_{\ell}^{res}$$

precisely δ_{ℓ}^{bg} is a constant phase shift caused by the background noise. Also δ_{ℓ}^{res} increases quickly from 0 to π at resonance and generally traverses value of $\pi/2$. For energies near the resonance energy ($\mathcal{E}_r$): $\delta_{\ell}^{res} = \pi/2 + \pi(\mathcal{E} - \mathcal{E}_r)/2\Gamma$, where Γ is halfwidth of resonance (Taylor, 1972; Valentin, 1982). As Figure 2.6 shows, four different cases are presented. The bottom plots present the corresponding behavior of the variations of the resonant phase shift δ_{ℓ} for $\delta_{\ell}^{bg} = 0,\ \pi/4,\ \pi/2,\ 3\pi/4$ presented in the top plots.

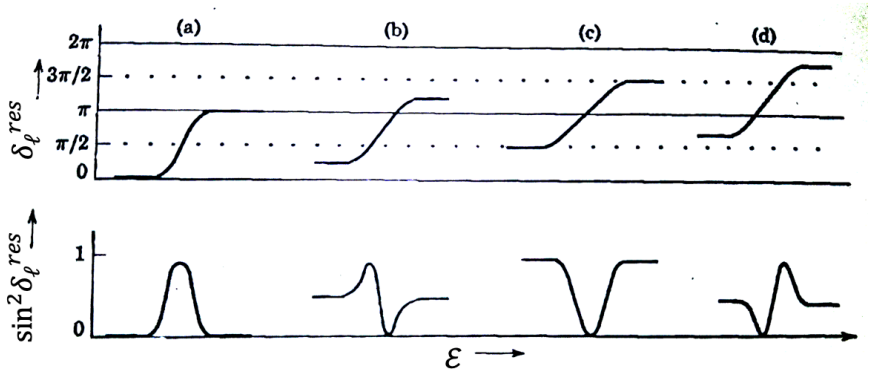

Figure 2.6: Four different resonances, the $\sin^2\delta_\ell^{res}$ present the corresponding behavior of the variations of the resonant phase shift δ_ℓ for $\delta_\ell^{bg} = 0,\ \pi/4,\ \pi/2,\ 3\pi/4$ presented in the upper plots.

For simplicity, in this thesis, the background noise is chosen to be zero (case (a)). In this case, δ_ℓ is:

$$\delta_\ell = \delta_\ell^{res} = \frac{\pi}{2} + \pi\frac{\mathcal{E}-\mathcal{E}_r}{2\Gamma} \qquad \cot\delta_\ell \approx \frac{4}{\pi}\left(\frac{\pi}{2} - \delta_\ell\right) = \frac{2(\mathcal{E}_r-\mathcal{E})}{\Gamma} \tag{2.40}$$

and since $\sin^2 x = (1+\cot^2 x)^{-1}$, the Equation 2.39 gives:

$$\sigma_\ell = \frac{4\pi}{k_0^2}(2\ell+1)\frac{\Gamma^2}{4(\mathcal{E}-\mathcal{E}_r)^2+\Gamma^2} \tag{2.41}$$

This equation is known as "Breit-Wigner" formula (in case of $\delta_\ell^{bg} = 0$). Getting back to the Equation 2.35, the scattering amplitude shall be given as:

$$f(\theta) = -\frac{2\ell+1}{k_0}P_\ell(\cos\theta)\frac{\Gamma}{2(\mathcal{E}-\mathcal{E}_r)+i\Gamma} \tag{2.42}$$

In the presence of inelastic processes (*i.e.* herein absorption), two kinds of partial scattering amplitude have to be considered to describe the total scattering process (Landau and Lifshitz, 1981; Valentin, 1982; Taylor, 1972): one, $\underline{f}_{k,\ell}^{(el)}$, for pure scattering (elastic contribution) and another, $\underline{f}_{k,\ell}^{(ab)}$ for the absorption (inelastic) contribution. For a TOR occurring at energy $\mathcal{E}_r$, these two partial scattering amplitudes for an incident light energy $\mathcal{E}$ are, respectively:

$$f_{k,\ell}^{(e)} = -\frac{2\ell+1}{k_0}\frac{\Gamma_e}{2(\mathcal{E}-\mathcal{E}_r)+i\Gamma}P_\ell(\cos\theta) \tag{2.43}$$

and

$$f_{k,\ell}^{(a)} = -\frac{2\ell+1}{k_0}\,\frac{(\Gamma_e\Gamma_a)^{1/2}}{2(\mathcal{E}-\mathcal{E}_r)+i\Gamma}\,P_\ell(\cos\theta) \tag{2.44}$$

Equations 2.45 are just the application of Equation 2.33 over the equations above. Subsequently the associated scattering and absorption partial cross sections follow straightforwardly:

$$\begin{aligned}\sigma_{s,\ell} &= \frac{4\pi}{k_0^2}(2\ell+1)\,\frac{\Gamma_e^2}{4(\mathcal{E}-\mathcal{E}_r)^2+\Gamma^2}\\ \sigma_{a,\ell} &= \frac{4\pi}{k_0^2}(2\ell+1)\,\frac{\Gamma_e\Gamma_a}{4(\mathcal{E}-\mathcal{E}_r)^2+\Gamma^2}\end{aligned} \tag{2.45}$$

The total partial cross section is thus:

$$\sigma_{e,\ell} = \sigma_{s,\ell} + \sigma_{a,\ell} = \frac{4\pi}{k_0^2}(2\ell+1)\,\frac{\Gamma_e\Gamma}{4(\mathcal{E}-\mathcal{E}_r)^2+\Gamma^2} \tag{2.46}$$

which is again nothing more than the optical theorem $(4\pi/k_0)\,\mathrm{Im}\{f_{k_0,\ell}(0)\}$. In these expressions, Γ_e is the resonance width for the pure scattering component, Γ_a the resonance width due to absorption, and $\Gamma = \Gamma_a + \Gamma_e$.

III. CLOUD OPTICAL THICKNESS & SINGLE SCATTER ALBEDO

Cross sections are also used to solve radiation problems in radiative transfer which deals with the propagation of light in a medium. Such medium can be a cloud for instance. Two parameters are the most used elements in the radiative transfer algorithm, they are highly related to the cross section, especially to the extinction cross section σ_e.

III.1 Cloud optical thickness (COT)

The Cloud Optical Thickness, or simply known as COT and symbolized by τ, is a physical value of the cloud's restraint for absorbing light. It is strongly related to the extinction coefficient (β_e):

$$\beta_e = \beta_a + \beta_s$$

where β_a and β_s are respectively the absorption coefficient and the scattering coefficient. The extinction coefficient is related to σ_e by: $\beta_e = N\,\sigma_e$ where N is the number density

or concentration. Equation 2.47 represents the equation of the cloud optical thickness (τ) between two points (z_1 and z_2) where the distance $|z_1 - z_2|$ is the cloud's thickness . If $z_2 > z_1$, for instance:

$$\tau(z_1, z_2) = \int_{z_1}^{z_2} \beta_e(z)\,\mathrm{d}z = \tau(z_1) - \tau(z_2) \tag{2.47}$$

III . 2 Single scattering albedo

An important parameter related to β_e and β_s , with the aim of highlighting the difference between the degree of scattering and extinction in a medium, is the Single Scattering Albedo (SSA), symbolized by $\tilde{\mathrm{w}}$:

$$\tilde{\mathrm{w}} = \frac{\beta_s}{\beta_e} = \frac{\beta_s}{\beta_a + \beta_s}$$

The values of $\tilde{\mathrm{w}}$ varies between 0 and 1. The zero refers to a complete absorbing medium and the one refers to a complete scattering medium. Thus:

$$\tilde{\mathrm{w}} = \frac{\beta_s}{\beta_e} = \frac{\sigma_s}{\sigma_e}$$

CONCLUSION

In this chapter, we have introduced some of the fundamental formulas of light droplet interaction and we have presented the concept of cross sections. Afterwards, the concept of tunneling optical resonance, shortly named TOR, has been theoretically defined. Such resonances are certain if the light-droplet interaction is treated as one dimensional quantum problem (Taylor, 1972). The existence of light tunneling has been localized and has been identified theoretically.

Therefore some of the localization aspects had been introduced and some of the aspects of TOR variation had been identified. Whereas, the scattering amplitude was slightly given. And our final point in this chapter was about the cloud optical thickness and single scatter albedo two important parameters that characterize the optical properties of the clouds in radiative transfer. In the next chapter, we will present the methodology pursue to solve the theoretically form of TOR given in the present chapter. Also, the scattering amplitude and the cross sections will be presented in a form that suits the tunneling resonance.

CHAPTER 3 Methodology

Despite the fact that the concept of TOR has been explained and theoretically presented but the ways to identify it, numerically, are still hard to attend. In this chapter, we will present an easy and adaptable method to characterizes and locates TOR. This method is the transfer matrix method that consists in finding for which energy $\mathcal{E}_{p,ef}$ these resonances occur and under what conditions. The manner to calculate the halfwidth of these resonances is presented in the second part of this chapter.

I. THE TRANSFER MATRIX METHOD

The transfer matrix method (TMM) is a fast and accurate algorithm that solves the one dimension Schrödinger equation for a constant potential well. The generality and usefulness of this method are based on the fact that the Schrödinger equation is a linear differential equation and on the general relations of continuity of the wavefunction and its first derivatives.

A linear-wise decomposition is also possible. It leads to eigenfunctions as Airy functions instead of exponential functions in a piece-wise decomposition as here. The former decomposition has not been used herein because Airy functions are more complex that exponential ones, the two elementary matrices are not so simple to define, and the well is better modeled by a sharp transition as a step. The two previous reasons explain maybe why the linear-wise-decomposition is not commonly used. For a comparison of these two kinds of decomposition, in favor of the piece-wise decomposition, see Jonsson and Eng (1990).

This valuable tool, stated by Jonsson and Eng (1990), gives not only the correct complex eigenvalues, but also the correct wave functions. The TMM, used for a wide range of 1-dimensional linear problems in quantum mechanics, consists in dividing a potential energy (*i.e.* an interaction) into elementary interactions to identify their associated matrix (Pujol et al., 2014; Kroemer, 1994). This method is also used in several majors such as electronics, mechanics, ray optics and more generally to any system that can be characterized by a linear

response.

Precisely, $\mathcal{E}_{p,ef}$ can be analyzed as being the combination of two elementary profiles:

1. stepped changes (upward or downward) between two adjacent bins of different potential energies, presented in green step color in Figure 3.1b);

2. region of uniform potential energy between two consecutive stepped changes, presented in red step color in Figure 3.1b).

Each of this elementary potential energies can be mathematically represented by an appropriate matrix that connects the complex amplitude of the wavefunction at the input " i " of the elementary potential energy to the complex amplitude of the wavefuntion at the output " o " of the elementary potential energy.
The linearity of the 1D stationary Schrödinger equation leads to express the wave function $\underline{\psi}_j(r)$, in a region j , as follows (Pérez et al., 2013):

$$\underline{\psi}_j(r) = \underline{\psi}_j^+ \exp(ik_j r_j) + \underline{\psi}_j^- \exp(-ik_j r_j) \tag{3.1}$$

where $\underline{\psi}_j^+$ and $\underline{\psi}_j^-$ are respectively the progressive and regressive complex amplitudes of the wave functions, and $\underline{k}_j$ is the complex angular wavenumber:

$$k_j = \left[\frac{2m}{\hbar^2}(\mathcal{E} - \mathcal{E}_{p,j})\right]^{1/2} = k_{rj} + i\kappa_j \tag{3.2}$$

k_j is real in a classically-allowed region and imaginary in a classically-forbidden region (k_j is equal to $i\kappa_j$) .

I . 1 Two different mediums

Figure 3.1a) shows two different mediums. The first medium is presented in white and the second is presented in gray. The complex wave amplitudes, for the first medium, are presented by $\underline{\psi}_i^+$ and $\underline{\psi}_i^-$ in opposite directions, and by $\underline{\psi}_o^+$ and for the second medium $\underline{\psi}_o^-$, also in opposite directions.

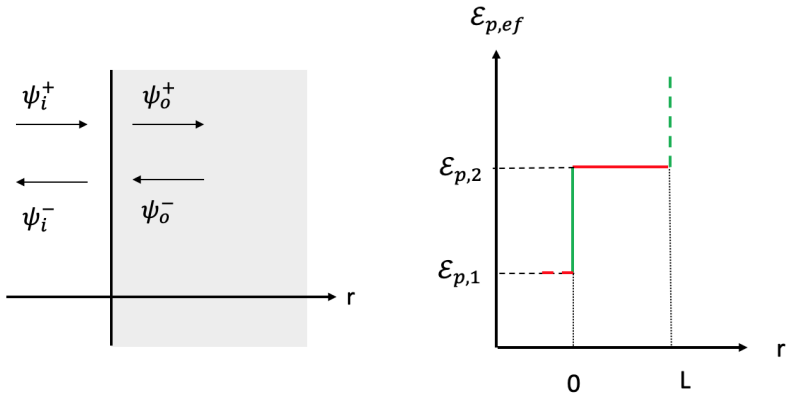

a) *b)*

Figure 3.1: **(a)** An interface between two different mediums and **(b)** Decomposition of the effective potential energy into steps

The Shrödinger equation is linear, so the incoming complex wave amplitudes can be expressed as follow in function of the outgoing complex wave amplitudes:

$$\underline{\psi}_o^+ = a\,\underline{\psi}_i^+ + b\,\underline{\psi}_i^- \qquad \text{and} \qquad \underline{\psi}_o^- = c\,\underline{\psi}_i^+ + d\,\underline{\psi}_i^- \tag{3.3}$$

where a, b, c and d are four complex constants.

The latter equation can be written in the form of the following matrix:

$$\begin{bmatrix} \underline{\psi}^+ \\ \underline{\psi}^- \end{bmatrix}_i = \begin{bmatrix} a & b \\ c & d \end{bmatrix} \begin{bmatrix} \underline{\psi}^+ \\ \underline{\psi}^- \end{bmatrix}_i \tag{3.4}$$

The four complex constants a, b, c and d, are not independent from each other. Therefore, by using the property of reversibility Schrödinger equation, one has:

$$\underline{\psi}_o^+ = d^\star\,\underline{\psi}_i^+ + c^\star\,\underline{\psi}_i^- \qquad \text{and} \qquad \underline{\psi}_o^- = b^\star\,\underline{\psi}_i^+ + a^\star\,\underline{\psi}_i^- \tag{3.5}$$

transformed into the matrix:

$$\begin{bmatrix} \underline{\psi}^+ \\ \underline{\psi}^- \end{bmatrix}_o = \begin{bmatrix} d^\star & c^\star \\ b^\star & a^\star \end{bmatrix} \begin{bmatrix} \underline{\psi}^+ \\ \underline{\psi}^- \end{bmatrix}_i \tag{3.6}$$

So, by comparing the matrix of Equations 3.4 to matrix 3.6, one finds: $a = d^{\star}$ and $b = c^{\star}$.

In case of scattering, a stationary light source is located on one side (in Figure 3.1b) the source is located in medium 1), and the detector is on the opposite side of the barrier (medium 2), therefore $\underline{\psi}_o^- = 0$:

$$\underline{\psi}_o^- = c\,\underline{\psi}_i^+ + d\,\underline{\psi}_i^- = 0 \tag{3.7}$$

The matrix $abcd$ leads to define the complex amplitude of reflection and transmission factors, respectively $\underline{r}$ and $\underline{\tau}$:

$$\underline{r} = \frac{\underline{\psi}_i^-}{\underline{\psi}_i^+} = -\frac{c}{d} \qquad \text{and} \qquad \underline{\tau} = \frac{\underline{\psi}_o^+}{\underline{\psi}_i^+} = \frac{dd^{\star} - cc^{\star}}{d} = \frac{da - cb}{d} \tag{3.8}$$

The complex amplitude of reflection and transmission factors are defined also by the wave theory as follows (Fresnel type relationships):

$$\underline{r} = \frac{k_1 - \underline{k}_2}{k_1 + k_2} \quad \text{and} \quad \underline{\tau} = \frac{2k_1}{k_1 + k_2} \quad \text{with} \quad k_1 = \frac{(2m\mathcal{E})^{1/2}}{\hbar} \quad \text{and} \quad k_2 = \frac{[2m(\mathcal{E} - \mathcal{E}_{p,0})]^{1/2}}{\hbar}$$

If $\mathcal{E} < \mathcal{E}_{p,0}$, k_2 is complex ($k_2 = i\kappa_2$). Since $\underline{r} = -c/d$, c is then proportional to $k_2 - k_1$ and d is proportional to $k_1 + k_2$.

Therefore the two constants are: $c = Q(k_2 - k_1)$ and $d = Q(k_2 + k_1)$, and the transmission factor is:

$$\underline{\tau} = \frac{\underline{\psi}_o^+}{\underline{\psi}_i^+} = \left(\frac{dd^{\star} - cc^{\star}}{d}\right) = QQ^{\star}\left[\frac{(k_2k_1)^2 - (k_2 - k_1)^2}{Q(k_2 + k_1)}\right] = Q^{\star}2k_2\frac{2k_1}{(k_2 + k_1)} = \frac{2k_1}{k_1 + k_2}$$

and since $\underline{\tau} = 2k_1/(k_1 + k_2)$, the constant Q is: $Q^{\star} = 1/2k_2 = Q$. After identifying the four constants a, b, c and d the matrix of Equation 3.4 is written as follow:

$$\begin{bmatrix} \underline{\psi}^+ \\ \underline{\psi}^- \end{bmatrix}_o = \frac{1}{2\underline{k}_2}\begin{bmatrix} k_2 + k_1 & k_2 - k_1 \\ k_2 - k_1 & k_2 + k_1 \end{bmatrix}\begin{bmatrix} \underline{\psi}^+ \\ \underline{\psi}^- \end{bmatrix}_i \tag{3.9}$$

The determinant of this matrix is then:

$$ad - cd = \frac{1}{4k_2^2}\left[(k_2 + k_1)^2 - (k_2 - k_1)^2\right] = \frac{4k_1k_2}{4k_2^2} = \frac{k_1}{k_2} \tag{3.10}$$

The next step consists in adjusting the form of the latter matrix, so that its determinant is

equal to 1. Therefore:

$$\begin{bmatrix} k_1^{1/2}\underline{\psi}^+ \\ k_1^{1/2}\underline{\psi}^- \end{bmatrix}_o = \frac{1}{2(k_1k_2)^{1/2}} \begin{bmatrix} k_2+k_1 & k_2-k_1 \\ k_2-k_1 & k_2+k_1 \end{bmatrix} \begin{bmatrix} k_1^{1/2}\underline{\psi}^+ \\ k_1^{1/2}\underline{\psi}^- \end{bmatrix}_i \tag{3.11}$$

The refraction- reflection R and the transmission T probabilities are given as:

$$R = \frac{|J^-_{p,i}|}{J^+_{p,i}} \quad \text{and} \quad T = \frac{J^+_{p,o}}{J^+_{p,i}} \tag{3.12}$$

with the current probability as:

$$J_{p,j} = \frac{1}{2}\left[\underline{\psi}^*_j\left(\frac{-i\hbar}{m}\frac{\mathrm{d}\underline{\psi}_j}{\mathrm{d}x}\right) + \underline{\psi}_j\left(\frac{-i\hbar}{m}\frac{\mathrm{d}\underline{\psi}_j}{\mathrm{d}x}\right)^*\right] = J^+_{p,j} + J^-_{p,j} \quad \text{with} \quad J^\pm_{p,j} = \pm\frac{\hbar k_j}{m}|\underline{\psi}^\pm_j|^2 \tag{3.13}$$

Therefore the matrix $[\mathcal{R}]$, presented in color green (Figure 3.1b)), is a reflection-refraction matrix that connects the wave function amplitudes just before the step with the wave function amplitudes just after the step:

$$[\mathcal{R}] = \frac{1}{(2k_1k_2)^{1/2}} \begin{bmatrix} k_1+k_2 & k_2-k_1 \\ k_2-k_1 & k_1+k_2 \end{bmatrix}$$

with a determinant that is equal to unity:

$$\det[\mathcal{R}] = \frac{1}{4k_1k_2}\left[(k_2+k_1)^2-(k_2-k_1)^2\right] = 1 \tag{3.14}$$

Therefore the refraction-reflection and transmission probabilities are:

$$R = \frac{|J^-_{p,1}|}{J^+_{p,1}} = \frac{|\underline{\psi}^-_i|^2}{|\underline{\psi}^+_i|^2} = |r|^2 = \left(\frac{c}{d}\right)^2 \tag{3.15}$$

and

$$T = \frac{J^+_{p,3}}{J^+_{p,1}} = \frac{|k_2^{1/2}\underline{\psi}^+_o|^2}{|k_1^{1/2}\underline{\psi}^+_i|^2} = \frac{k_2}{k_1}|\underline{\tau}|^2 = \frac{1}{d^2} \tag{3.16}$$

I . 2 Uniform medium

For a uniform medium, with a distance of L between two consecutive steps, $\underline{\psi}_o^+ = \underline{\psi}_i^+ \exp(ikL)$ and with $\underline{\psi}_o^- = \underline{\psi}_i^- \exp(-ikL)$. The matrix $[\mathcal{T}]$, presented in color red (Figure 3.1b)), is a propagation matrix between two consecutive steps at a distance L from each other:

$$[\mathcal{T}] = \begin{bmatrix} \exp(ikL) & 0 \\ 0 & \exp(-ikL) \end{bmatrix} \tag{3.17}$$

The determinant of the propagation matrix is equal to unity: $\det[\mathcal{T}] = 1$

I . 3 The -*abcd*-matrix

By considering $\mathcal{E}_{p,ef}$ as a succession of stepped changes (Figure 3.1b)), one obtains between the input and the output of $\mathcal{E}_{p,ef}$ a matrix $[\mathcal{M}]$ as the product of the elementary matrices:

$$[\mathcal{M}] = \Pi_i [\mathcal{T}]_i [\mathcal{R}]_i = \begin{bmatrix} a & b \\ c & d \end{bmatrix} \qquad \text{with} \qquad \det[\mathcal{M}] = 1$$

where a, b, c, and d are complex numbers. The determinant of the transfer matrix $[\mathcal{M}]$, is also called the *abcd* matrix. And since: $\det[\mathcal{R}] = \det[\mathcal{T}] = 1$, the $[\mathcal{M}]$ matrix is written as:

$$\begin{bmatrix} k^{1/2}\underline{\psi}^+ \\ k^{1/2}\underline{\psi}^- \end{bmatrix}_o = \begin{bmatrix} a & b \\ c & d \end{bmatrix} \begin{bmatrix} k^{1/2}\underline{\psi}^+ \\ k^{1/2}\underline{\psi}^- \end{bmatrix}_i \tag{3.18}$$

This matrix is written as:

(1) $k_o^{1/2}\,\underline{\psi}_o^+ = a\; k_i^{1/2}\,\underline{\psi}_i^+ + b\; k_i^{1/2}\,\underline{\psi}_i^-$ and **(2)** $k_o^{1/2}\,\underline{\psi}_o^- = c\; k_i^{1/2}\,\underline{\psi}_i^+ + d\; k_i^{1/2}\,\underline{\psi}_i^-$

I . 4 Confined state

The incident wavelength is considered as zero after being captured in the potential well. Because in case of confined (or bound) states, the corresponding complex amplitude of the wavefunction must vanish at the boundaries such as $\underline{\psi}_i^+ = 0$. And since $\underline{\psi}_o^- = 0$, therefore the elements of matrix $[\mathcal{M}]$ in Equation 3.18 are written as:

(1) $k_o^{1/2}\,\underline{\psi}_o^+ = 0 + b\; k_i^{1/2}\,\underline{\psi}_i^-$

(2) $0 = 0 + d\; k_i^{1/2}\,\underline{\psi}_i^-$ and so we conclude that: d must be zero.

Therefore, this matrix is adequate to identify TOR states that are, indeed, quasi-bound state (confined state in the well). For numerical computation, it is more convenient to search for the minimum value of $\ln|d|$ since first d is a complex number and second a null value of d can never be reached rigorously (for any confined state, the value of d is very small compared with that of a non-confined state). For details about the TM approach and its condition of application, see Pujol et al. (2014).

II. DETERMINATION OF THE RESONANCE SHARPNESS

As it was mentioned in the previous chapter, the scattering amplitude is one of the most important parameters that leads to calculate the cross sections and therefore some transfer radiative parameters. And as the Equation 2.42 has illustrated, the scattering amplitude depends on the halfwidth (Γ) of a resonance.

This section is devoted to present the substitute formula of the halfwidth that suits the resonance of TOR.

Guimaraes and Nussenzveig (1994) gave slightly the answers in their article, starting with the formula of complex energy:

$$\underline{\mathcal{E}} = \mathcal{E}_r - i\frac{\Gamma}{2} \tag{3.19}$$

where the real part $\mathcal{E}_r$ corresponds to the position of the resonance, and the imaginary part corresponds to the half of the resonance halfwidth.

According to the hypothesis of Guimaraes and Nussenzveig (1994) and Valentin (1982), a small imaginary refractive index (*i.e.* low absorption) has no effect on the resonance positions. Therefore, in the following, the refractive index is considered to be real while calculating the resonance positions.

Now, considering the halfwidth (Γ), the impact of the imaginary part of $\underline{n}$ (the κ), can be treated in the following way: taking into account a small absorption by the droplet, *i.e.* small value of κ.

Guimaraes and Nussenzveig (1994) have proposed that the halfwidth with no absorption (Γ_{el}) will be added to the quantity: $K\mathcal{E}_r$ where $K = \kappa/n$.

Therefore the final form of Γ_{abs} is that:

$$\Gamma_{abs} = \frac{2\,\mathcal{E}_r\kappa}{n} \tag{3.20}$$

Finally the total halfwidth is then: $\Gamma = \Gamma_{el} + \Gamma_{abs}$ where Γ_{el} and Γ_{abs} are respectively the elastic halfwidth, where the absorption is zero, and the inelastic halfwidth, where absorption is not null.

The computation to find the halfwidth is by fixing the incident energy $\mathcal{E}$ at $\mathcal{E}_r$ and then decreasing it, by an arbitrary small quantity α, according to the following formula: $\mathcal{E}_- = \mathcal{E}_r(1-N\alpha)$, with N an integer number and so, for each value of $\mathcal{E}_-$, $\ln|d|$ is computed. When half of the value of $\ln|d|$ at resonance is reached, the reduction is stopped $(N = N_-)$.

The same process is performed by increasing $\mathcal{E}$ from $\mathcal{E}_r$ and so defining $\mathcal{E}_+ = \mathcal{E}_r(1+N\alpha)$. The increasing process is thus stopped at $N = N_+$.

Resonance width is thus $\Gamma = \mathcal{E}_+ - \mathcal{E}_- = \alpha\,(N_+ - N_-)\mathcal{E}_r$.

CONCLUSION

Chapter 3 offers to deal with the $\mathcal{E}_{p,ef}$ for specific values of ℓ, $\mathcal{E}$ and D, by dividing it into small steps as matrix $[\mathcal{R}]$ and $[\mathcal{T}]$, and so characterizing it by a matrix $abcd$ with a very important rule: $\ln|d|= 0$ correspond to confined state, *i.e.* TOR. This matrix also offers the opportunity to obtain the wave function throughout a define area.

In the second part of this chapter, we have presented the halfwidth method in order to calculate the scattering amplitude of TOR and therefore to calculate the cross sections of TOR. This method will be the base of the most important results presented in the next chapter.

CHAPTER 4 Results

In this chapter, we shall start by presenting an example on the manner to detect and characterize TOR and then, by illustrating the application of the condition ($\ln|d|=0$) cited in chapter 3.

Afterwards, we will show the 1D and 2D plots presenting the light density inside a droplet for different cases (TOR, non TOR) calculated by the TMM and by the Mie theory.

The cross sections (scattering, extinction and absorption) will be compared within two important distributions. Starting with a simple situation for a single isolated droplet and then considering a more realistic situation such as a cloud population and the nine channels of the POLDER instruments. We will calculate the natural light, related to scattering amplitude, for both distributions. We will study the impact of TOR on the satellite observations and on the remote sensing technique when light-spherical scatterer interaction is involved.

I. CASE OF A SINGLE DROPLET

I.1 Algorithm for TOR characterization

We are going to present a new method to identify the position of TOR for a specific value of incident energy ($\mathcal{E}$) and specific diameter (D, or radius $r_d = D/2$) of a droplet.

The procedure to pursue is as follow:

1. We fix the inputs, by considering a wavelength λ, an incident light energy $\mathcal{E}$ and an angular wave-number k_0. Those parameters are related to each other according to the formulas: $\mathcal{E}\,(\text{eV}) \approx 1.239/\lambda(\mu\text{m})$ and $k_0 = \mathcal{E}/(\hbar c)$.

2. The refractive index $\underline{n} = n + i\kappa$ is estimated using the experimental values taken from Hale and Querry (1973). Precisely, in this chapter, the used values of $\underline{n}$ are interpolated in order to find the corresponding value of $\underline{n}$ to the chosen value of $\mathcal{E}$. Figure 4.1 shows the two elements of $\underline{n}$. The first plot presents the real component n

and the second plot represents the imaginary component κ in function of $\mathcal{E}$. In both plots, the blue dots represent the values taken from Hale and Querry (1973) while the red dots represent the interpolated values.

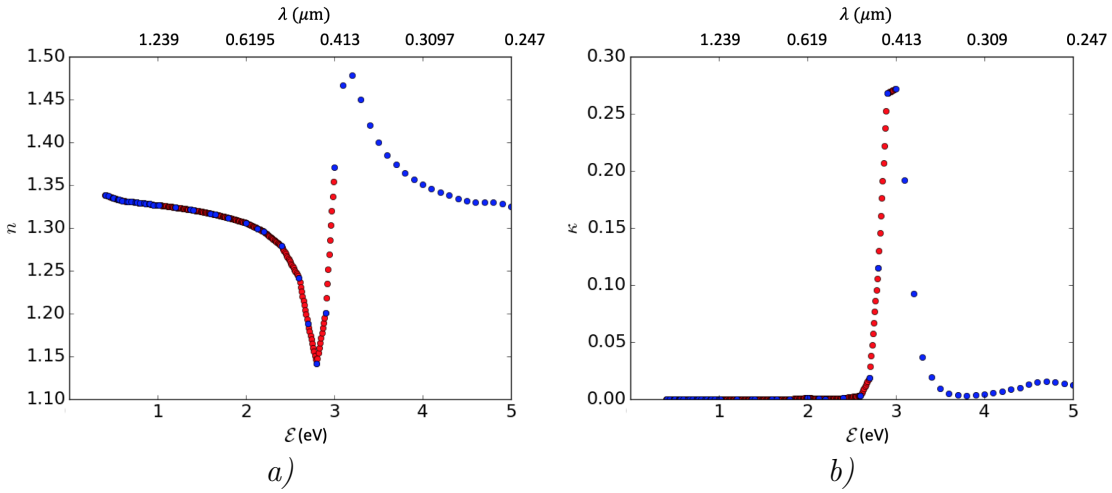

Figure 4.1: Experimental values presented in blue dots and interpolated values presented in red dots (a) of n the real component of $\underline{n}$ and (b) κ the imaginary component of $\underline{n}$

3. Fixing the r-axis: we divide this axis into two arrays, r_1 and r_2, the first array corresponds to the distance from r_{min} to $r_d - \delta_r$, the second one is from $r_d + \delta_r$ to r_{max} where r_d is the radius of the droplet $(r_d = D/2)$ and r_{min}, r_{max} are respectively the limits of the r-axis (depends on the droplet characteristics) and δ_r being a very small number that represents the *steps*.

4. Calculate for each component of r-axis the corresponding $\mathcal{E}_{p,ef}/\mathcal{E}$. For the very precise value of the r-axis r_d, we have to consider two different refractive indices. Therefore, for $r = r_d$, we calculated $(\mathcal{E}_{p,ef}/\mathcal{E})_{before}$ for the index optical that corresponds to the droplet and $(\mathcal{E}_{p,ef}/\mathcal{E})_{after}$ for the optical index that corresponds to the air $(n = 1)$.

5. The potential effective energy $\mathcal{E}_{p,ef}$ is formulated by grouping the arrays:

$$\left[\left(\frac{\mathcal{E}_{p,ef}}{\mathcal{E}}\right)_{r_1}, \left(\frac{\mathcal{E}_{p,ef}}{\mathcal{E}}\right)_{before}, \left(\frac{\mathcal{E}_{p,ef}}{\mathcal{E}}\right)_{after}, \left(\frac{\mathcal{E}_{p,ef}}{\mathcal{E}}\right)_{r_2}\right] \text{ for } r\text{-axis} = \left[r_1, r_d^{before}, r_d^{after}, r_2\right]$$

6. Using the transfer matrix method presented in chapter 3 – TMM – tho solve the radial equation and therefore we determine the $\ln|d|$ *vs.* ℓ.

The identifications of TOR is then easy to find by searching for the local minima – under some conditions – of $\ln|d|$ which will be explained in details later in section I . 2 . The calculated ℓ represents the value of the resonant TOR.

I . 2 Example

Starting with an example for more precision and clearness on how to identify the TOR: after applying the procedure written in the previous subsection (subsection I . 1), Figure 4.2 displays the variation of $\ln|d|$ *vs.* ℓ , for diameter $D = 26.5\mu$m and an incident energy $\mathcal{E} = 1.0156\,$eV . And for not complicating things (and as it is proven in chapter 3) $\underline{n}$ is taken as real $(n = 1.3237)$ since the imaginary part κ is in order of 10^{-5} (κ will be taking into account later). The blue dots correspond to the integer values of ℓ , and as we can see there are three minima of $\ln|d|$, those minima are presented in blue stars. TOR corresponds to those minima for which ℓ is an integer since ℓ , by definition, is the partial wave. But from a numerical point of view, it is rare to have a minimum of $\ln|d|$ for an exact integer value of ℓ . Therefore, after testing a variety of constant values that depend on the depth of the resonance and on the distance that separates the minimum from the closest integer value, we established a TOR under the two (in this order) next circumstances:

- the closest integer (the blue dots) should be located at less than $\epsilon = 0.03$ from the value of ℓ for which $\ln|d|$ is minimum (the blue stars) – (see Figure 4.3);

- the associated value of $\ln|d|$, namely that corresponds to the closest integer value, must be close enough to the local minimum of $\ln|d|$. Precisely, in Figure 4.3, the distance AB must be greater than $AC/2$.

After comparing these two criteria to Figure 4.2, only the minimum at $\ell = 77$ responds to both of the two criteria, and therefore $\ell = 77$ is considered as the only TOR for $D = 26.5\mu$m and $\mathcal{E} = 1.0156\,$eV . The minimum, located at $\ell \approx 83$ (as the Figure 4.3 shows) satisfies the second criterion $AB > AC/2$, but does not satisfy the first one. The same case is applied to the minimum located at $\ell \approx 72$. Therefore those two minima are not considered as TOR.

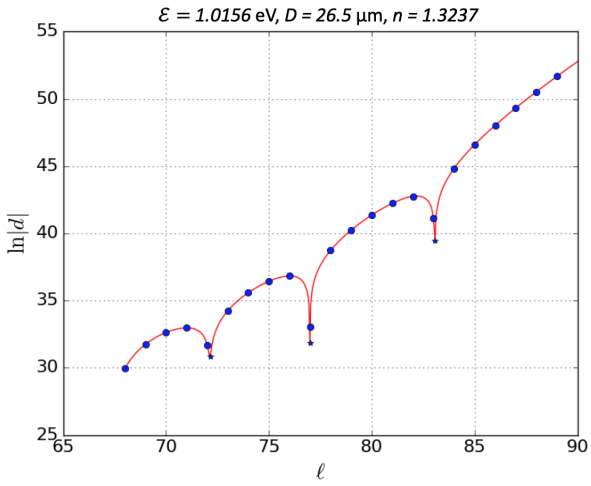

Figure 4.2: Variation of $\ln|d|$ *vs.* ℓ for a droplet of diameter $D = 26.5\mu$m and an incident energy $\mathcal{E} = 1.0156\,$eV. Blue dots are associated with integer values of ℓ. The three stars indicate the three local minima (Adapted with permission from Yaacoub et al. (2019) ©The Optical Society of America).

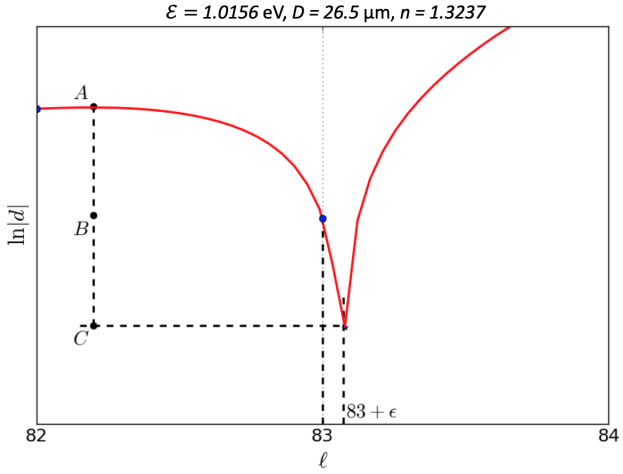

Figure 4.3: Sketch for the criterion determination of a TOR using the example $\ell = 83$). The distance between the minima – blue star and the closest integer – blue dot should be lower than $\epsilon = 0.03$. The second conditions is $AB > AC/2$ where point A represents the closest highest integer, B is the position of the closest integer and point C is the minima. The first criterion $\epsilon < 0.03$ is not satisfied. The second criterion $AB > AC/2$ is satisfied (Adapted with permission from Yaacoub et al. (2019) ©The Optical Society of America).

From the *abcd*-matrix, the square modulus of the radial wave-function $|rR_\ell|^2$, which is related to radial light energy density, can be determined and compared to the radial wave function calculated by the Mie theory. To puzzle out the difference between the absorption

by a TOR and by a non-TOR and the difference between the TMM and the Mie theory, the next 4 Figures (4.4, 4.5, 4.6, 4.7) suit different values of ℓ for the same example presented in Figure 4.2 (for $D = 26.5\mu$m and $\mathcal{E} = 1.0156\,$eV). The different values of ℓ are inspired by the different types of light-droplet interactions presented in Figure 2.5 in Chapter 2 (so while reading till the end of this section you might want to take a look at it).

Each figure will contain three subplots where the curves in red are calculated by the TMM, the curves in black are calculated by the Mie theory and the green curves are the difference between the red and black curves. Note that the scale between the curves and the figures might changes. The associated optical potentials $\mathcal{E}_{p,ef}$ are shown in color blue and the incident energies $\mathcal{E}$ are presented by black dashed lines. And as a reminder the characteristics of $\mathcal{E}_{p,ef}$ are presented in Figure 2.3. The unit of $r^2|R|^2$ is $a.u$ arbitrary unit since the light density is normalized.

The first figure (Figure 4.4) presents the TOR value of $\ell = 77$ found in the previous example of Figure 4.2 (case 3 in Figure 2.5). The resonance by tunneling appears clearly by a significant and sharp peak of light density that indicates a substantial amount of light inside the droplet, in the red curve, calculated by TMM. Whilst the light density outside the droplet, in the TMM calculation does not exceed $0.1\,a.u$ which is considered as a low value compared to the light density inside the droplet. The Mie theory illustrates, in the second plot, the contrary of what the TMM predicted, where the amount of light inside and outside the droplet is almost neglect. The green curve highlights the importance of the resonance inside the droplet where the square modulus of the wave-function attains $0.4\,a.u$. The light density, outside the droplet, is low in both calculation, the green plot shows a small difference in between.

The second figure (Figure 4.5) represents a non-TOR value, $\ell = 79 \in [\mathcal{E}_L, \mathcal{E}_H]$. The TMM and the Mie theory match and give the same results with no absorption of light inside the droplet. The two calculation also match in the calculation outside the droplet. The green curve shows that the difference between the two methods is equal to zero inside the droplet, and that the difference outside the droplet doesn't exceed the $0.005\,a.u$ which is considered as null.

The third figure (Figure 4.6) represents a non-TOR, $\ell = 60$. This value belongs to the below edge zone that produces a light resonance inside the droplet which is not related to tunneling. This is due to a "direct" interaction between the light and the droplet (cases 1 and 2 in Figure 2.5), the TMM calculation and the Mie theory predictions agree very well with some tiny differences outside the droplet ($0.004\,a.u$).

The last figure (Figure 4.7) represents a non-TOR, case 4 in Figure 2.5 where there is no interaction between the light. Figure 4.7 shows that there is no light inside the droplet and that both of TMM and Mie theory predictions are in very good agreement, with the difference between the two methods lower than $0.006\,a.u$.

These 4 figures represent all the possible cases of interaction light-droplet (TOR, non-TOR, below-edge, above-edge). And as these figures show the TMM and the Mie theory give the same results (with an irrelevant difference) in the case of non-TOR with a difference equal to zero inside the droplet and a value that does not exceed the $0.005\,a.u$ outside the droplet. Or in the case of TOR, the TMM showed a sharp important light density due to tunneling inside the droplet.

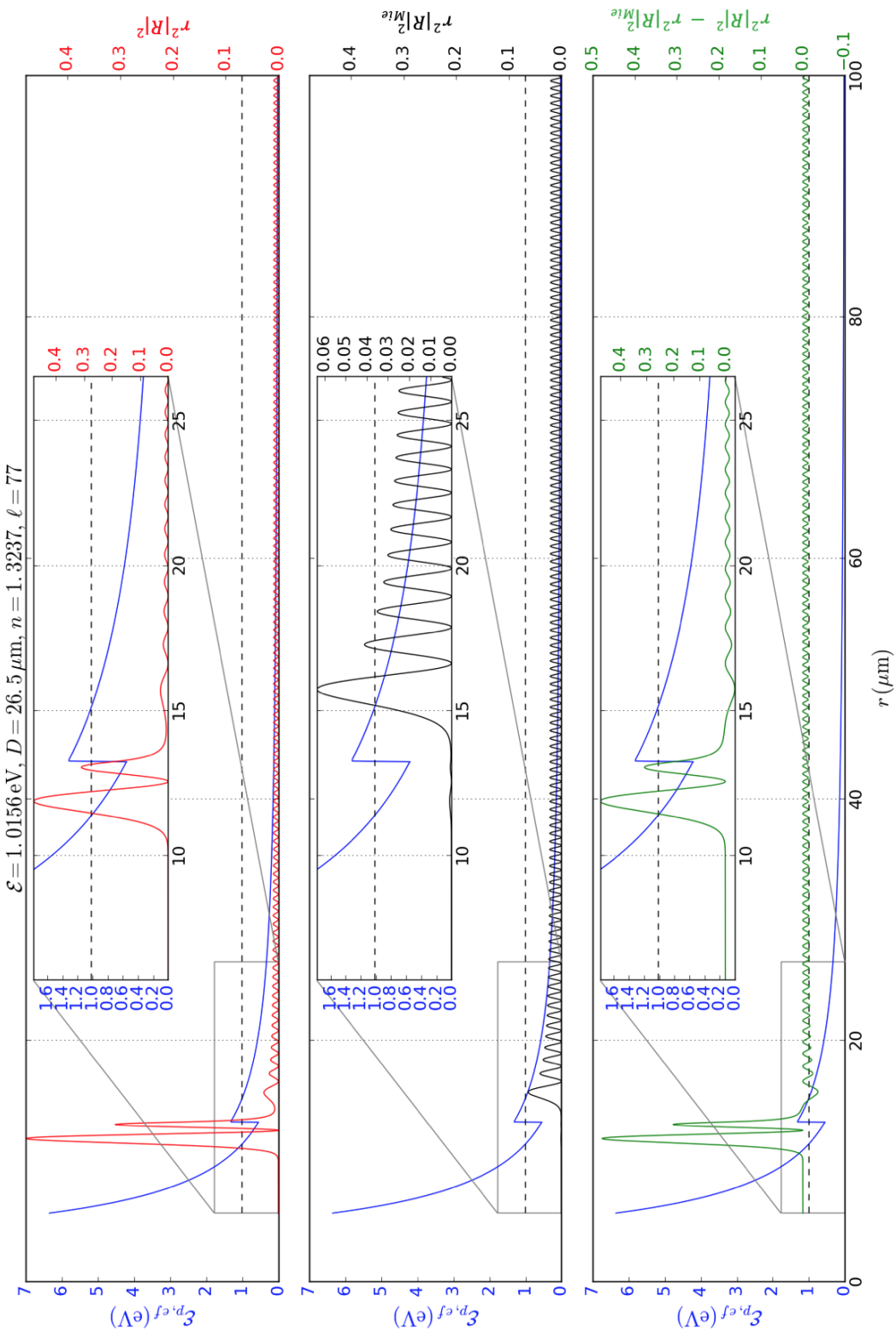

Figure 4.4: Square modulus of the radial wave-function $r^2|R|^2$ showing light energy density (normalized, arbitrary unit) for $\ell = 77$. The red plot is calculated using the TMM, the black plot is calculated using the Mie theory and the green plot is the difference between the first two plots. The profile $\mathcal{E}_{p,ef}$ is drawn in blue and $\mathcal{E}$ is indicated by black dashed horizontal lines (Adapted with permission from Yaacoub et al. (2019) ©The Optical Society of America).

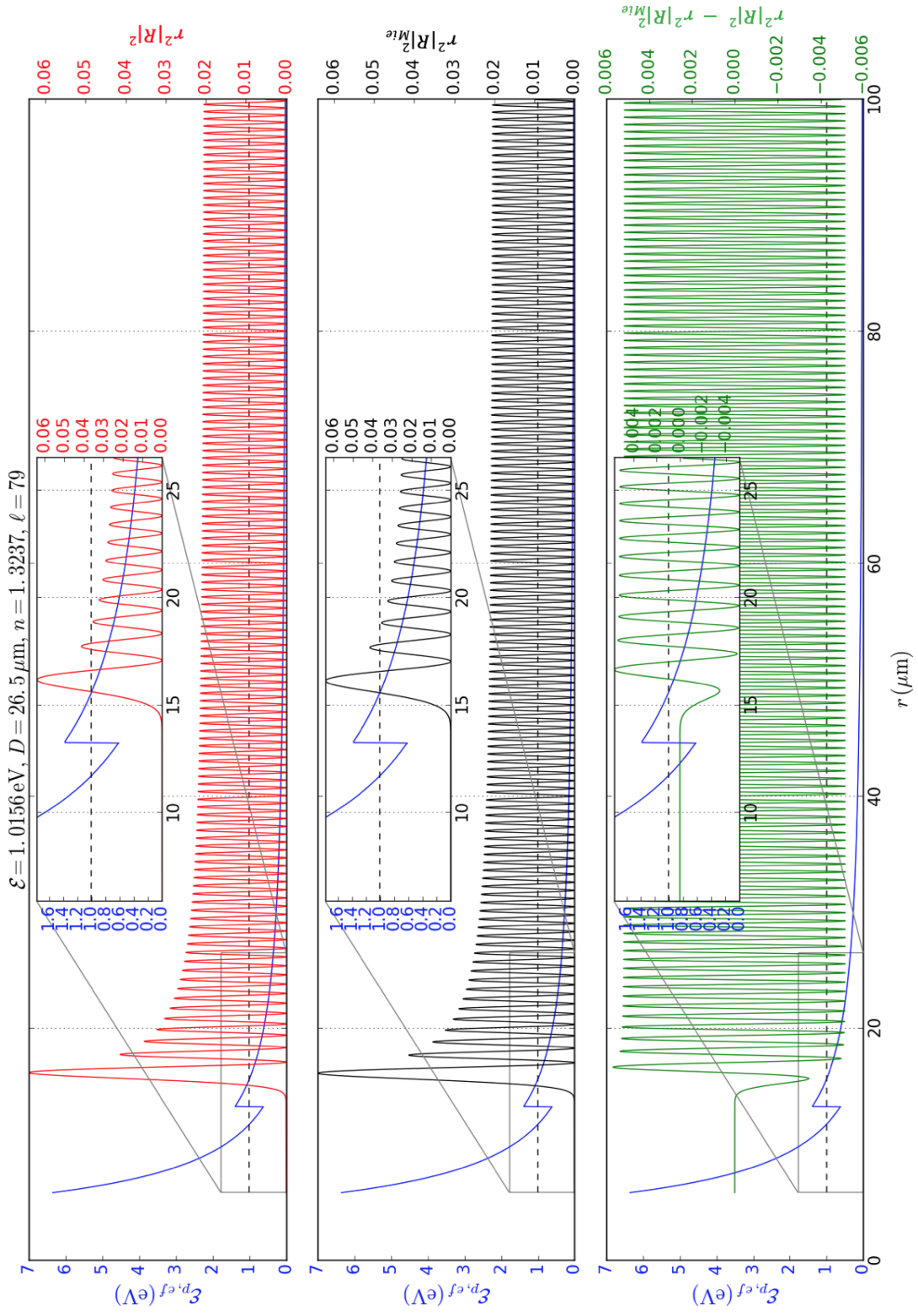

Figure 4.5: Same as Figure 4.4 but with $\ell = 79$ (Adapted with permission from Yaacoub et al. (2019) ©The Optical Society of America).

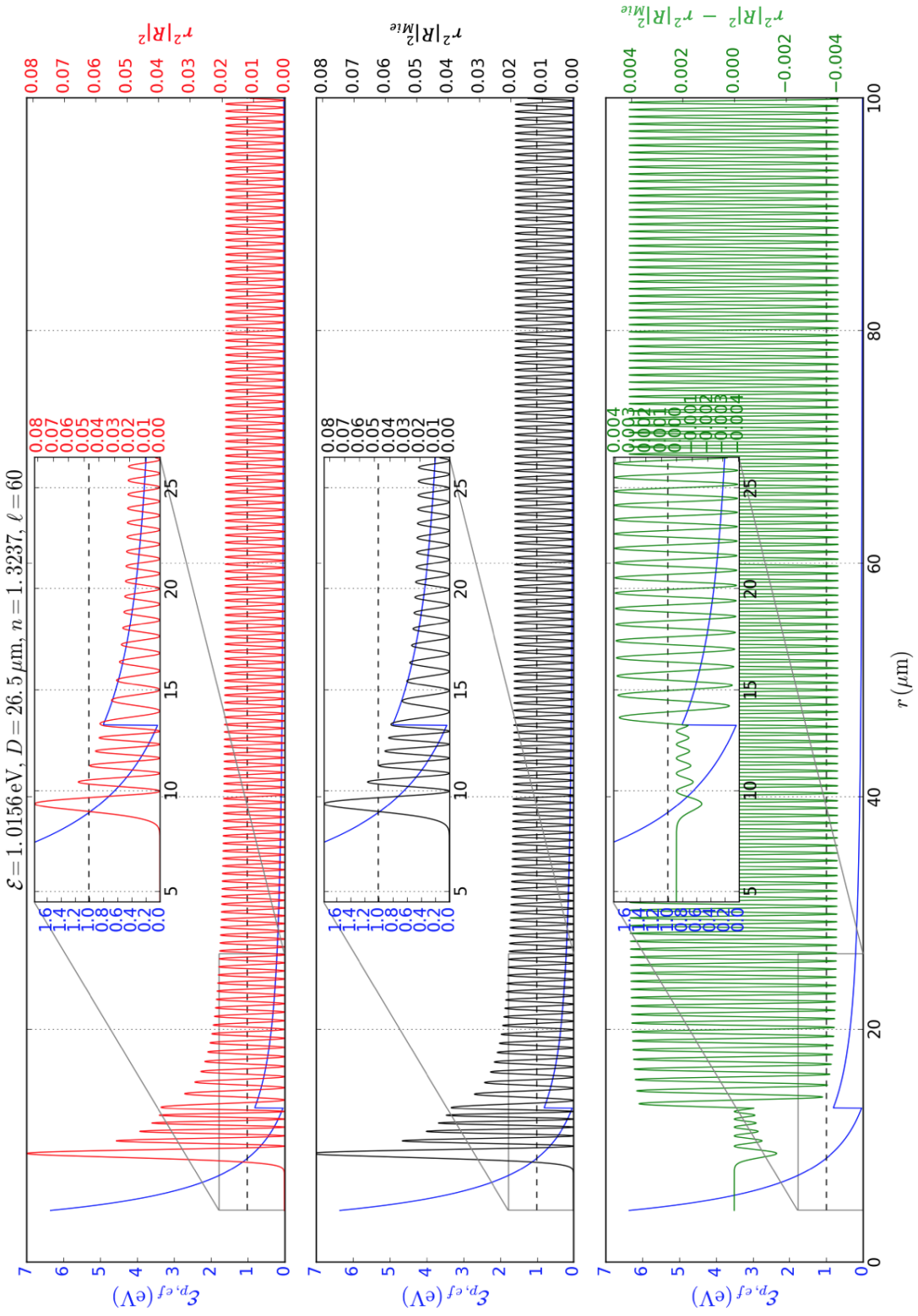

Figure 4.6: Same as Figure 4.4 but with $\ell = 60$ (Adapted with permission from Yaacoub et al. (2019) ©The Optical Society of America).

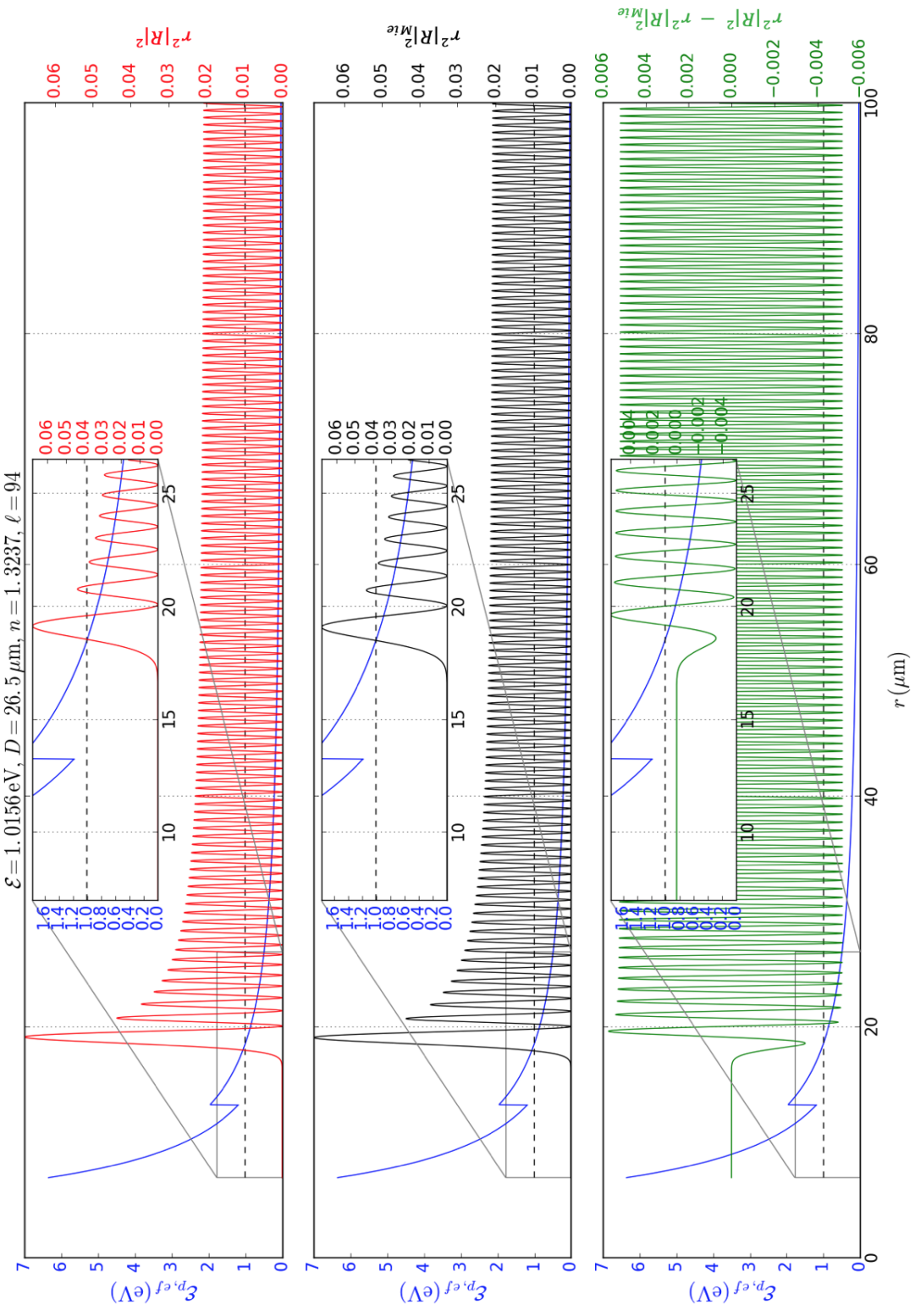

Figure 4.7: Same as Figure 4.4 but with $\ell = 94$ (Adapted with permission from Yaacoub et al. (2019) ©The Optical Society of America).

II. LIGHT DENSITY IN 2D

The last section has introduced the radial part of the light density. The light density, in two dimensional (2D) Cartesian plane, is presented by Equation 2.9, formed of the radial part $R(r)$ and the associated spherical harmonics $Y_\ell(\theta, \phi)$, the latter is presented in Equation 2.10. Therefore the same examples taken in section I.2 are treated in this section. So the next 4 figures (Figures 4.8, 4.9, 4.10 and 4.11), are obtained by adding the associated spherical harmonics Y_{77}, Y_{79}, Y_{60}, and Y_{94} to their radial part R_{77}, R_{79}, R_{60} and R_{94} respectively, forming the light density $\psi_\ell(r, \theta, \phi)$ in 2D.

The droplet is presented by a black circle of diameter D, with the center located at $x = y = 0$. The light densities are shown inside the droplets by some small dots with the correspondent values presented in the colorbar. For each figure, cited above, three illustrations are presented, the one on left belongs to the TOR calculation, the middle illustration belongs to the Mie calculation and the last illustration represents the difference between the two calculation. Note that the scale, even in the same figure (from plot to plot) might change.

The first figure (Figure 4.8) is for $\ell = 77$, a TOR value. It shows an obvious sharp light density inside the droplet for the TMM calculation with a very important value $|\psi|^2 = 0.56\, a.u$. The light density outside the droplet, in case of TMM calculation, is lower than the inside. In the second illustration, there is no trace of light density inside the droplet; instead, the light density – outside the droplet – is clearly shown. The illustration at right shows the important difference between both calculation for inside the droplet with a value of difference of $0.56\, a.u$, and for outside the droplet with a negative value. This figure agrees completely with the figure of light density 1D for the same value of ℓ (Figure 4.4).

The second figure (Figure 4.9) is for $\ell = 79$ that corresponds to a non-TOR. There is no light density inside the droplet for the TMM calculation and for Mie prediction. Both of these illustrations show a high value of light density outside the droplet. The last illustration shows the agreement of those calculation with a value that does not exceed the $\pm 0.0045\, a.u$. This figure synchronizes completely with the figure of light density 1D for the same value of ℓ (Figure 4.5).

The third figure (Figure 4.10) represents a non-TOR with $\ell = 60$. The light density is presented in high values inside the droplet for both calculation (where there is resonance but not related to tunneling, caused by a "direct" interaction between the droplet and light *i.e.* ray 1 and 2 in Figure 2.5). The light density outside the droplet using the TMM matches

the one calculated by the Mie theory. This figure agrees completely with the figure of light density 1D for the same value of ℓ (Figure 4.6).

And for the last figure (Figure 4.11) in the group of 2D, $\ell = 94$, there is no light density inside the droplet for the two calculation (TOR and Mie). The difference in light density outside the droplet does not exceed $\pm 0.002\, a.u$.

As it has been shown, the associated spherical harmonics do not impact the radial dependence (presented in Figures 4.4, 4.5, 4.6 and 4.7), but it has definitely changed the overall value of light density $|\psi|^2$. Obviously, the light density is still the highest inside the droplet in the case of a TOR, there is still no resonance for a non-TOR in the above-edge zone and there is always light density inside the droplet for the below-edge zone.

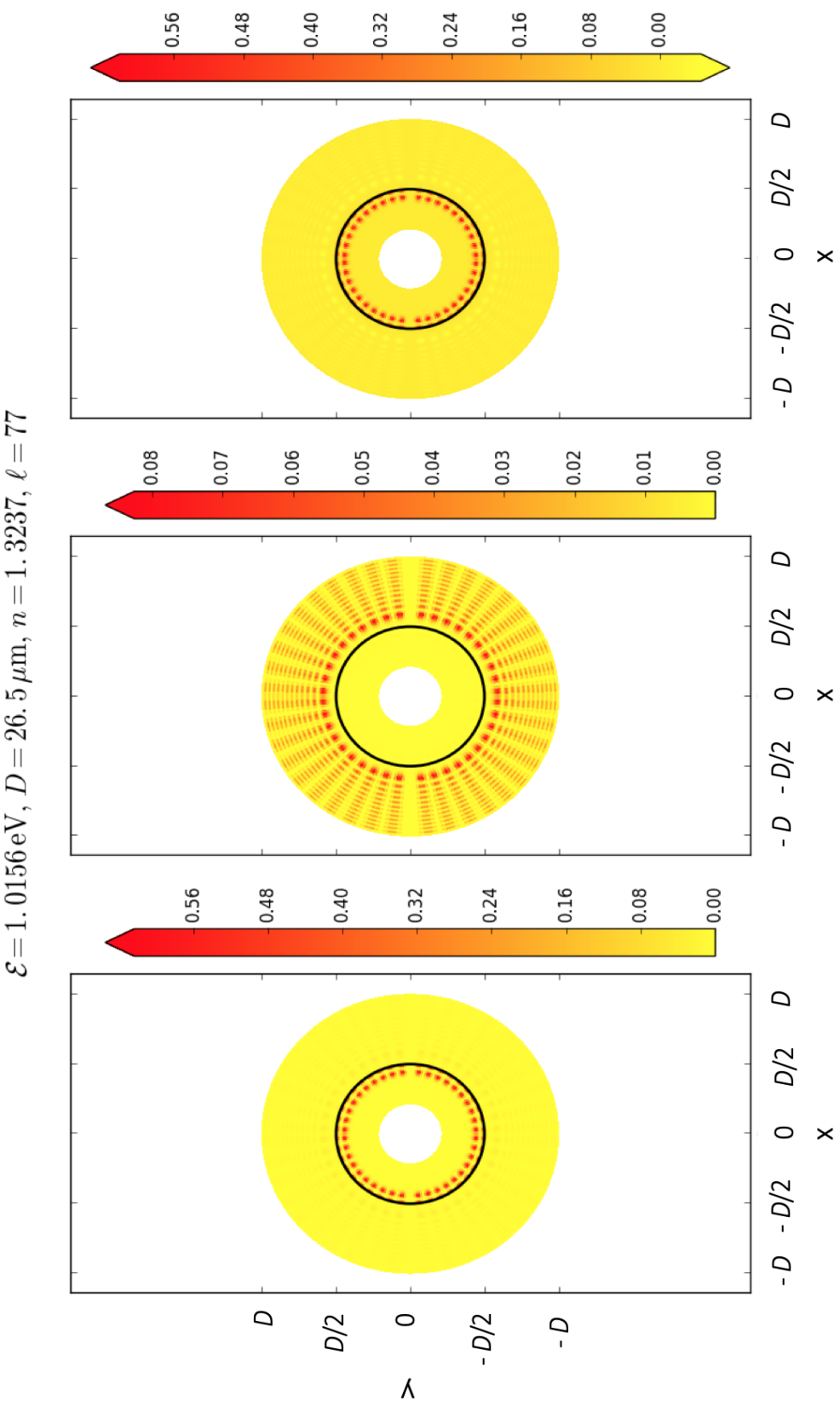

Figure 4.8: 2D-Cartesian representation of light density $|\psi|^2$ where $\psi = RY_{77}$, for a droplet presented in a black circle with $\mathcal{E} = 1.0156$ eV, $D = 26.5\mu$m and $\ell = 77$. To be compared with Figure 4.4.

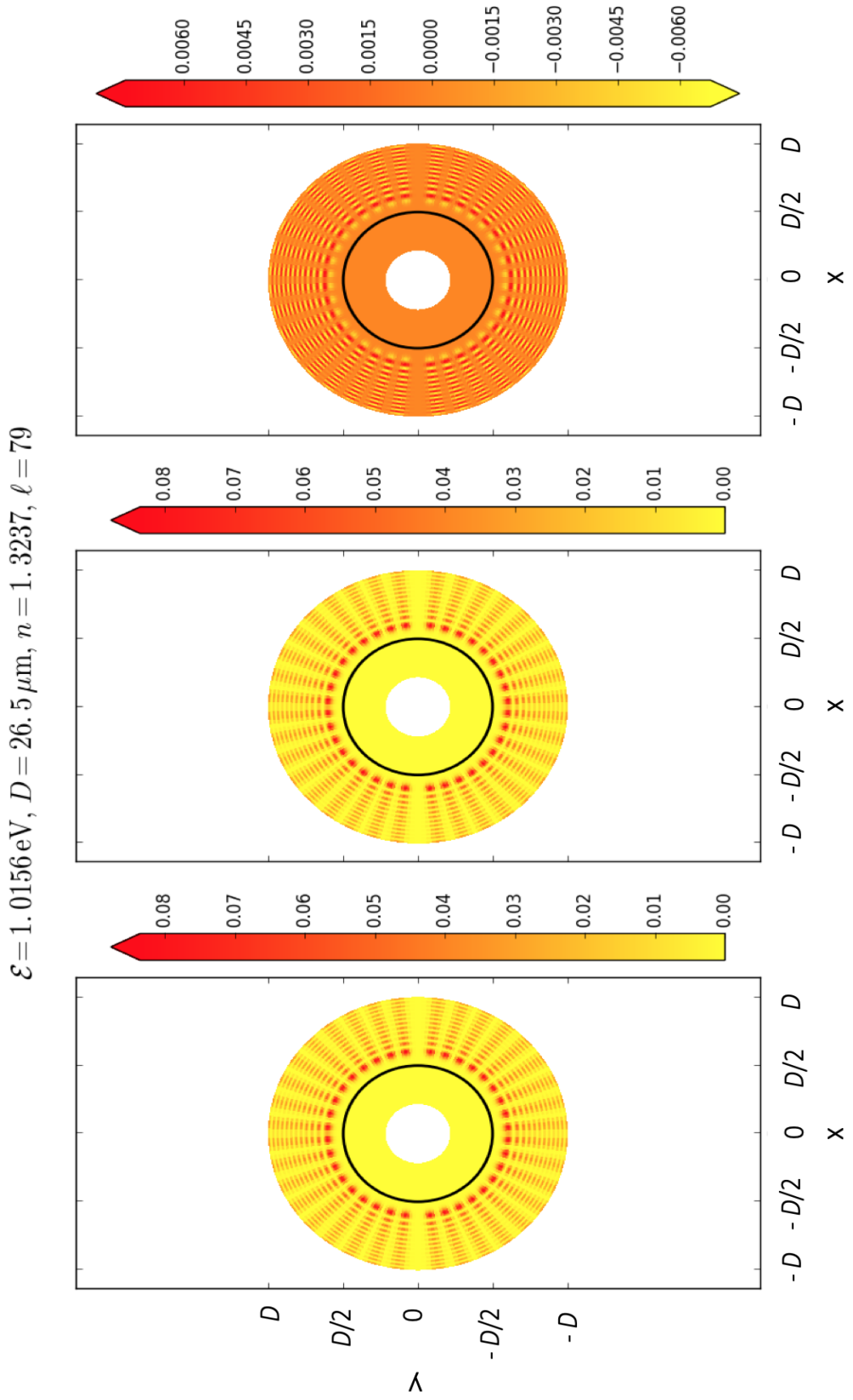

Figure 4.9: Same as Figure 4.8 but with $\ell = 79$. To be compared with Figure 4.5.

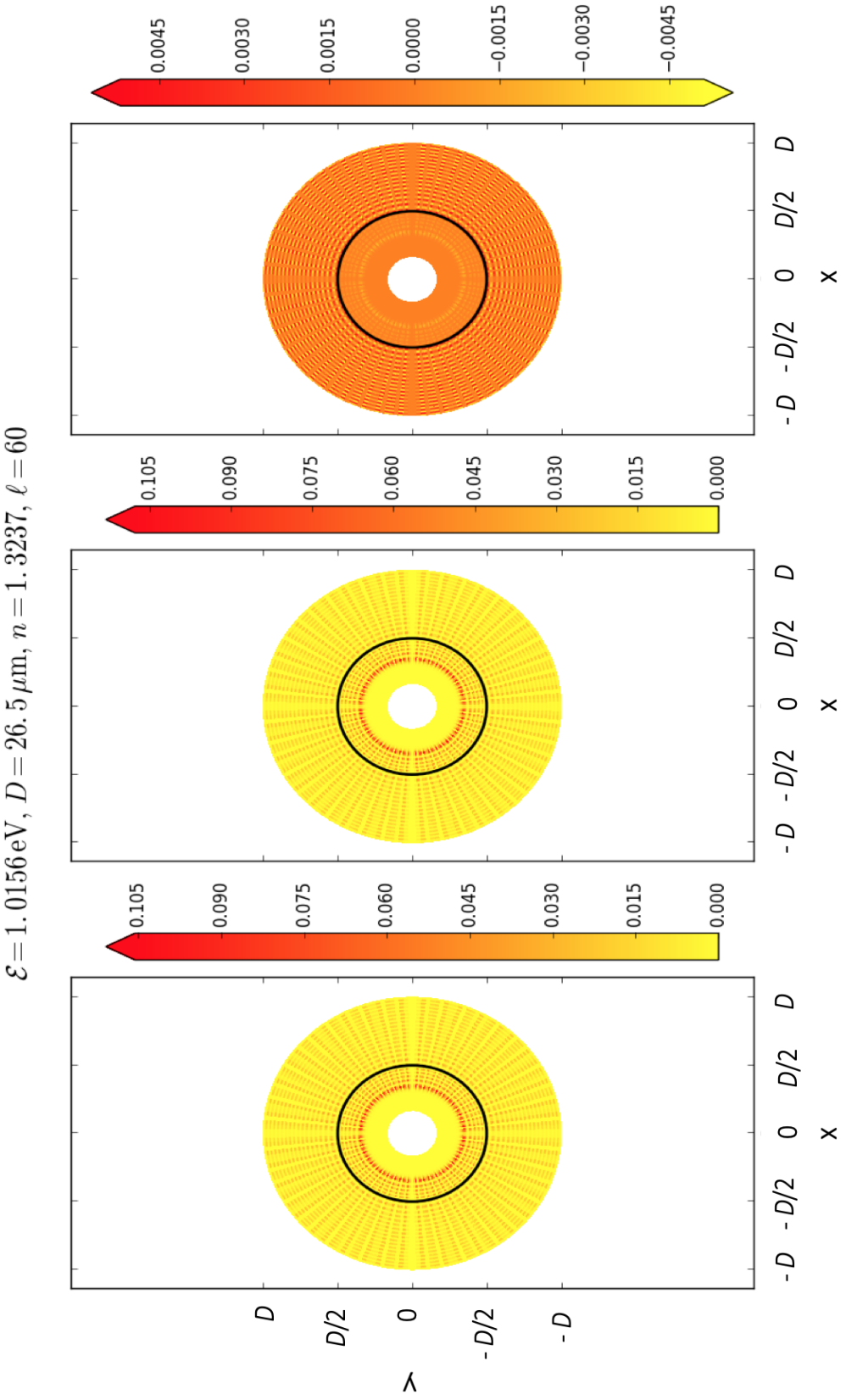

Figure 4.10: Same as Figure 4.8 but with $\ell = 60$. To be compared with Figure 4.6.

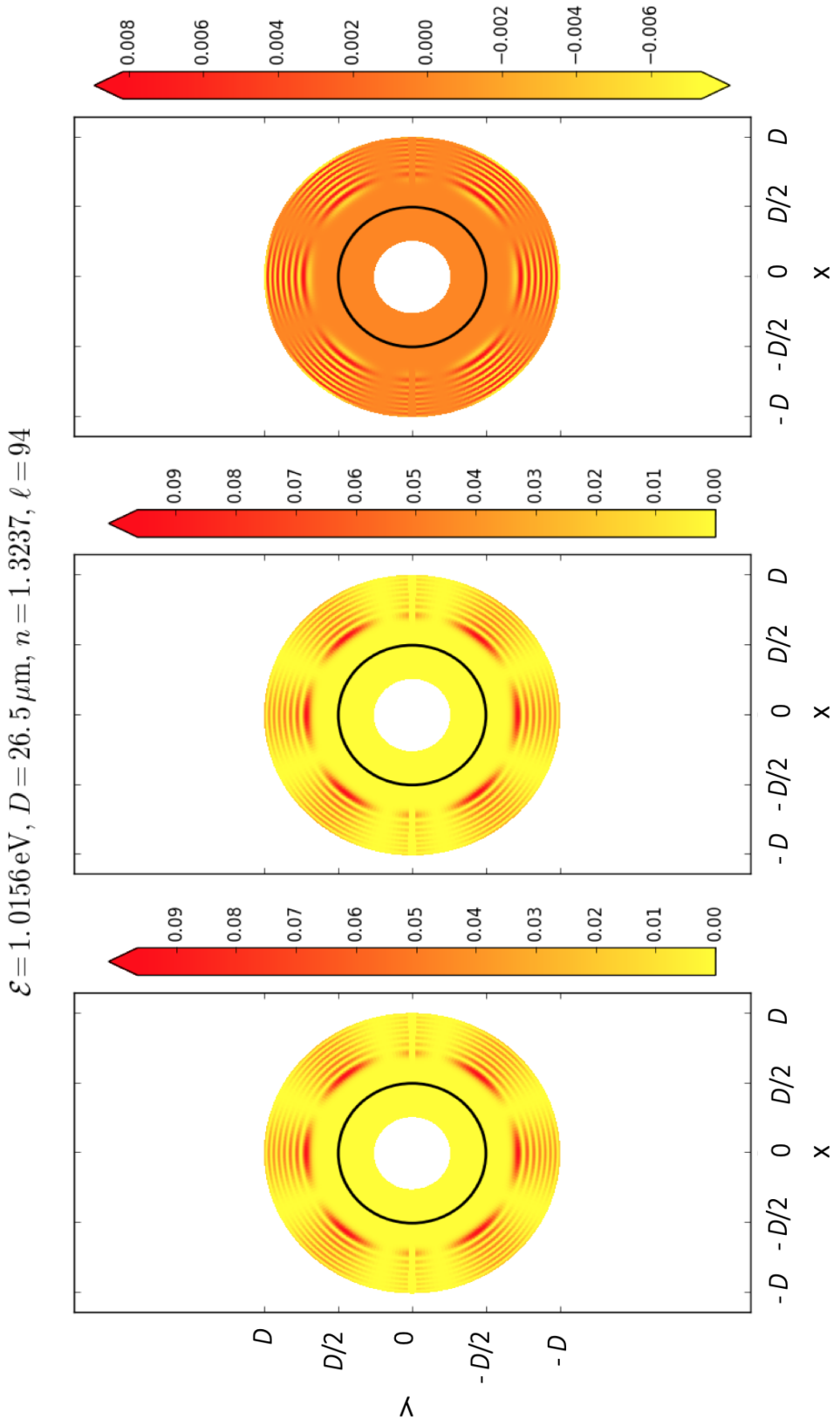

Figure 4.11: Same as Figure 4.8 but with $\ell = 94$. To be compared with Figure 4.7.

II . 1 TOR occurrences

After setting the criteria to choose the TOR and after confirming that the TMM is in total consistency with the Mie theory predictions in a non-TOR case, the occurrences of TOR are then calculated for some different values of diameters D and of incident energy $\mathcal{E}$ by running the same code made for one droplet (computation made in subsection I . 2), but this time for a wider range of incident energy $(\mathcal{E})$ and droplet diameter (D) .

The various values of D , from 5 to 30μm with step $= 0.5\mu$m , are chosen based on the typical diameters of the droplet in a warm cloud. The values of the incident energy $\mathcal{E}$ are chosen from $0.4\,$eV to $3.1\,$eV (equivalent to the values of λ from $2.478\,\mu$m to $0.354\,\mu$m) deciding to go from UV to IR. The values of n and κ for $\mathcal{E}$ are calculated as explained in the beginning of this chapter. The code consists in calculating the TOR occurrences by fixing one value of the incident energy $\mathcal{E}$ and one value of diameter D .

To summarize, we introduce for the first time Figure 4.12 that provides a synthetic representation, indicating the TOR occurrences (values of ℓ colorbar) for D and $\mathcal{E}$, where the range of ℓ is almost from 10 to 260 . This figure holds more than 860 values of TOR occurrences for different values of the triplet ($\mathcal{E}$, D and ℓ).

It is worth mentioning that from now on we refer by the "TOR" value or "TOR occurrences" to the value for which $|\ln d|$ is a minimum and obey the two criteria presented in I . 2 ; the TOR occurrences are always referred to as the partial wave ℓ .

For a given droplet (D is fixed), the lowest values of ℓ are associated to the lowest values of the incident energy $\mathcal{E}$. Conversely, for a fixed value of ℓ , the lower the energy correspond to the higher diameter. These results are consistent with the tunneling interpretation and with Equation 2.30 that mathematically demonstrates: if the value of ℓ increases, $\mathcal{E}$ will increase too, and if D increases, $\mathcal{E}$ will decrease (considering $\mathcal{E}_H$ because $\mathcal{E} \in [\mathcal{E}_L, \mathcal{E}_H]$).

Figure 4.13 represents the halfwidth (Γ) for the couple $(\mathcal{E}$, $D)$ of the resonances TOR presented in Figure 4.12. It appears, clearly, that resonance widths are at low values, ranging from less than $0.001\,$eV up to values 10 times higher. This indicates that $\mathcal{E}_r/\Gamma \sim 10^2 \rightarrow 10^3$.

Visibly, the higher D and/or $\mathcal{E}$ the sharper the resonance will get. In other words, the highest values of Γ (*viz.* the less sharp the resonance) concern energies lower than $1\,$eV , *i.e.* the IR region of the electromagnetic spectrum.

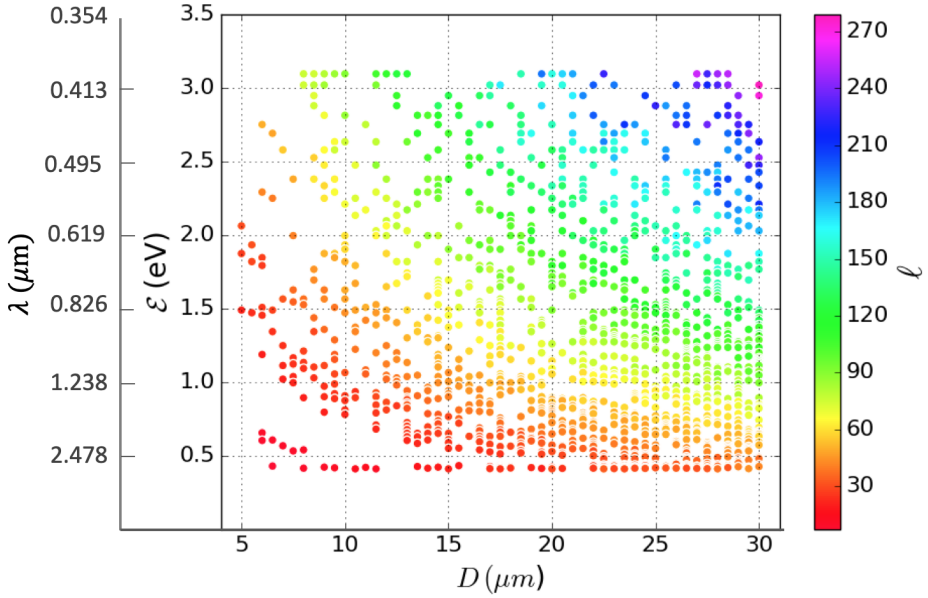

Figure 4.12: TOR occurrences according to the triplet $(\mathcal{E}, D, \ell)$ (Adapted with permission from Yaacoub et al. (2019) ©The Optical Society of America).

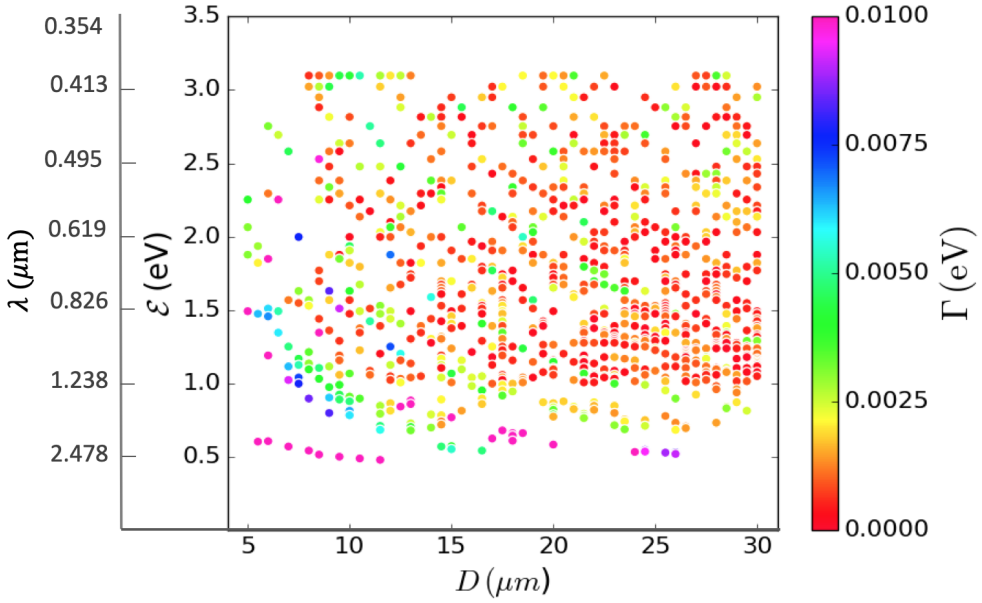

Figure 4.13: Resonance width Γ *vs.* the couple $(\mathcal{E}, D)$ for the TOR occurrences presented in Figure 4.12 (Adapted with permission from Yaacoub et al. (2019) ©The Optical Society of America).

II . 2 Comparison of cross section

As presented in chapter 2, the formulas of cross sections are related to the resonance width Γ. Since the manner to localize TOR has been identified and it is handy to calculate their corresponding widths, the cross sections can be computed using Equations 2.45 and 2.46, and compared with those given by the Mie theory (Equation 2.25). Precisely, for each diameter D and energy $\mathcal{E}$, the cross section $\sigma_\alpha(D, \mathcal{E}) = \sum_0^{\ell_{max}} \sigma_{\alpha,\ell}(D, \mathcal{E})$, where α stands for "s" (scattering), "e" (extinction) or "a" (absorption), is computed and compared to the corresponding Mie theory cross section (Equation 2.25). In case of TOR, the partial cross sections ($\sigma_{\alpha,\ell}$) are computed using Equations 2.45 and 2.46 if the ℓ-value corresponds to a TOR or using Equation 2.25 otherwise.

Comparisons between the cross sections of TOR and Mie are made considering the following ratio: $r_\alpha(\%) = (\sigma_\alpha^{TOR} - \sigma_\alpha^{Mie})/\sigma_\alpha^{Mie}$. In the sequel, these ratios will be given in percentage (%): the ratios r_α are always greater than 1 so, for simplicity, if r_α is equal to 10%, it means that σ_α^{TOR} is 10% higher than σ_α^{Mie}, *i.e.* $\sigma_\alpha^{TOR} = 1.10\,\sigma_\alpha^{Mie}$.

It is important to present the absolute values of Mie theory cross sections in order to understand if the high ratios are associated to high absolute values. This is shown in the next three figures (Figures 4.14, 4.15 and 4.16).

Figures 4.14, displays the ratio TOR/Mie and the Mie theory absolute values for the scattering cross sections. Figure 4.15 and Figure 4.16 are both presented in the same way as Figure 4.14, but they respectively display the extinction cross section and the absorption cross section.

It shows that scattering and extinction cross sections, Figure 4.14a) and Figure 4.15a), are a few percents higher than those predicted by the Mie theory, and in some cases can get up to 15% that correspond to $\sigma_{e,s}^{Mie} \approx 50\mu\text{m}^2$ for small diameter and for $\sigma_{e,s}^{Mie} \approx 688\mu\text{m}^2$ for higher diameter $(D = 20\mu\text{m})$.

The ratios r_s and r_e at low energy $(\mathcal{E} < 1.5\,\text{eV})$ and for small droplet $(D < 15\mu\text{m})$ reach 12%. For larger diameters, scattering and extinction ratios are between 5% and 8%.

The ratios r_e and r_s are small (lower than 2%) for the largest diameters and the highest energies (*i.e.* in the blue and UV regions of the electromagnetic spectrum). The smallest values of r_e and r_s correspond to the highest value of extinction and scattering cross section calculated using the Mie theory.

The case of absorption (σ_a) presented in Figure 4.16a) can be twenty times higher than Mie's absorption cross section. This figure has two colorbars, the multicolored one presents

the ratios in percentage from 0% to 15%, and the black-white colorbar represents the ratios with a higher value than 15%. The values of the black-white colorbar goes from 2 till 20.

There is no obvious distribution for the values of the cross sections that might depend on the couple ($\mathcal{E}$ and D). Most of the values shown in the Figure 4.16a) are of color pink (*vs.* in order of 15%) and of color black (*vs.* values range from 2 till 7). Although the absorption cross section calculated by the Mie theory shows almost a uniform and constant distribution of the values (around $5\mu\text{m}^2$).

These unexpected high values of absorption cross sections are explained by the fact that light energy can be very important inside a droplet in the case of TOR.

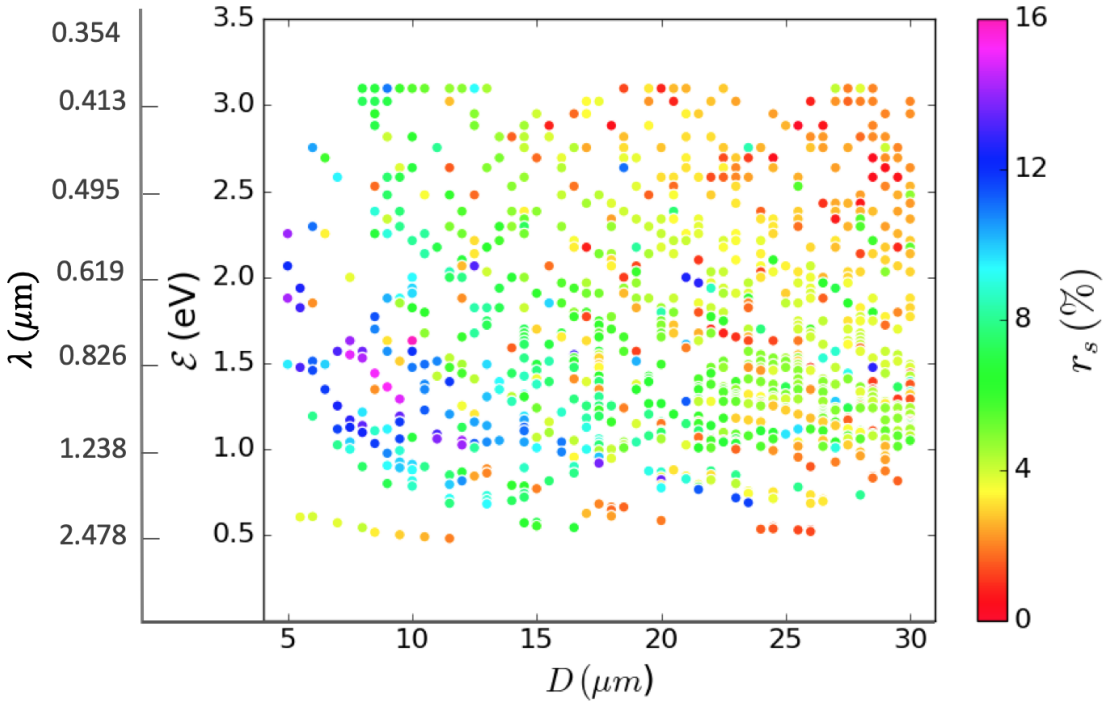

a) The ratio r_s (TOR/Mie) for the scattered cross section (Reprinted with permission from Yaacoub et al. (2019) ©The Optical Society of America)

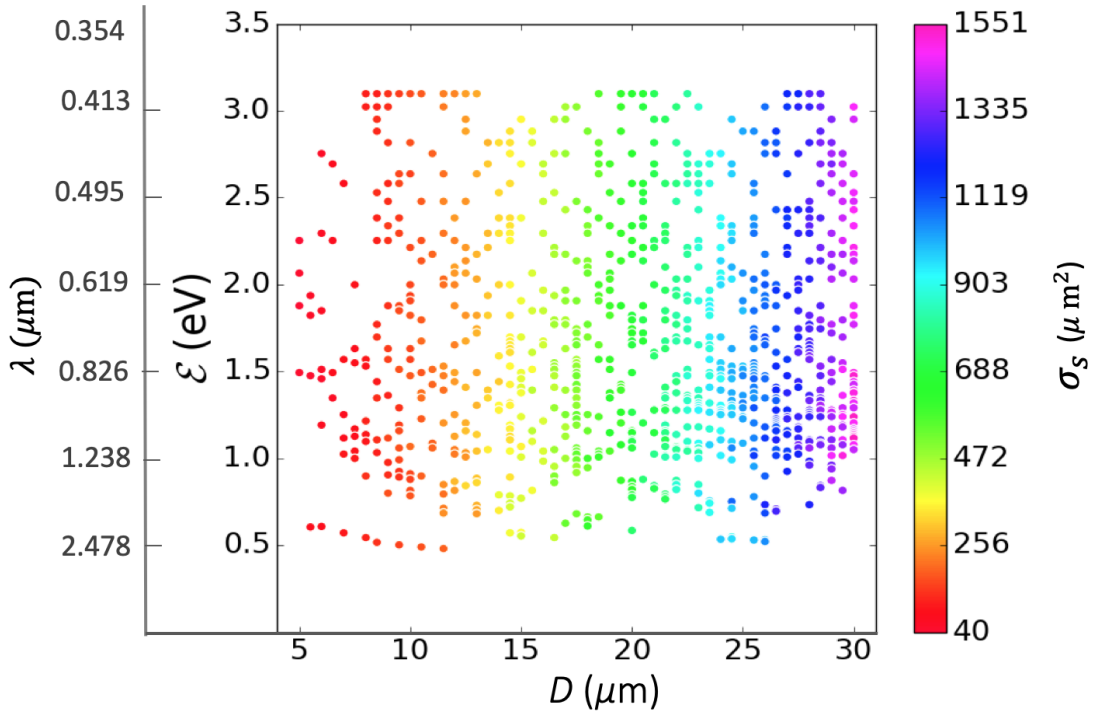

b) The scattered cross section given by the Mie theory

Figure 4.14: **(a)** Scattering cross section ratios in percentage (%) and **(b)** scattering cross section calculated using the Mie theory

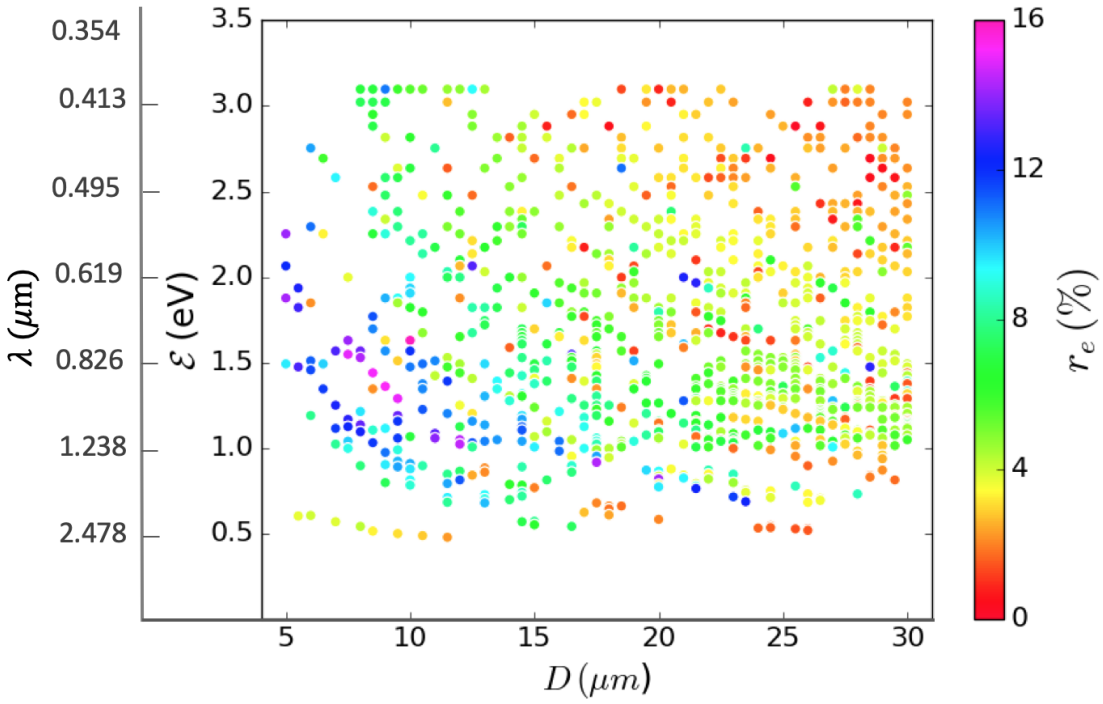

a) The ratio r_e (TOR/Mie) for the extinction cross section (Reprinted with permission from Yaacoub et al. (2019) ©The Optical Society of America)

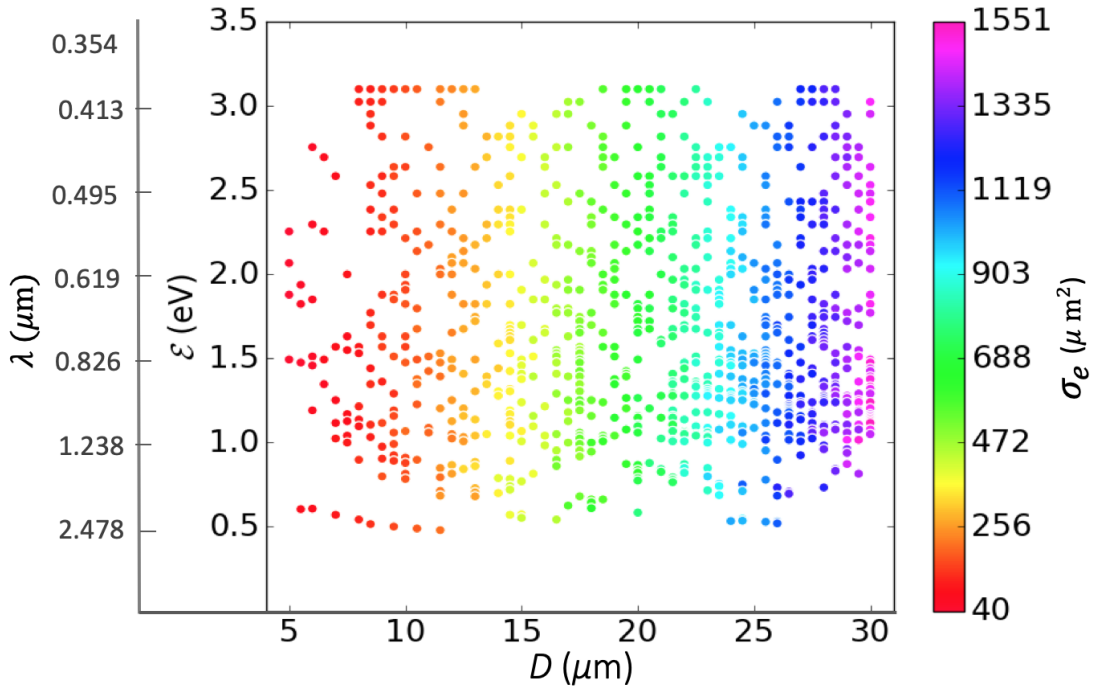

b) The extinction cross section given by Mie theory

Figure 4.15: Similar to Figure 4.14 but for the extinction cross sections

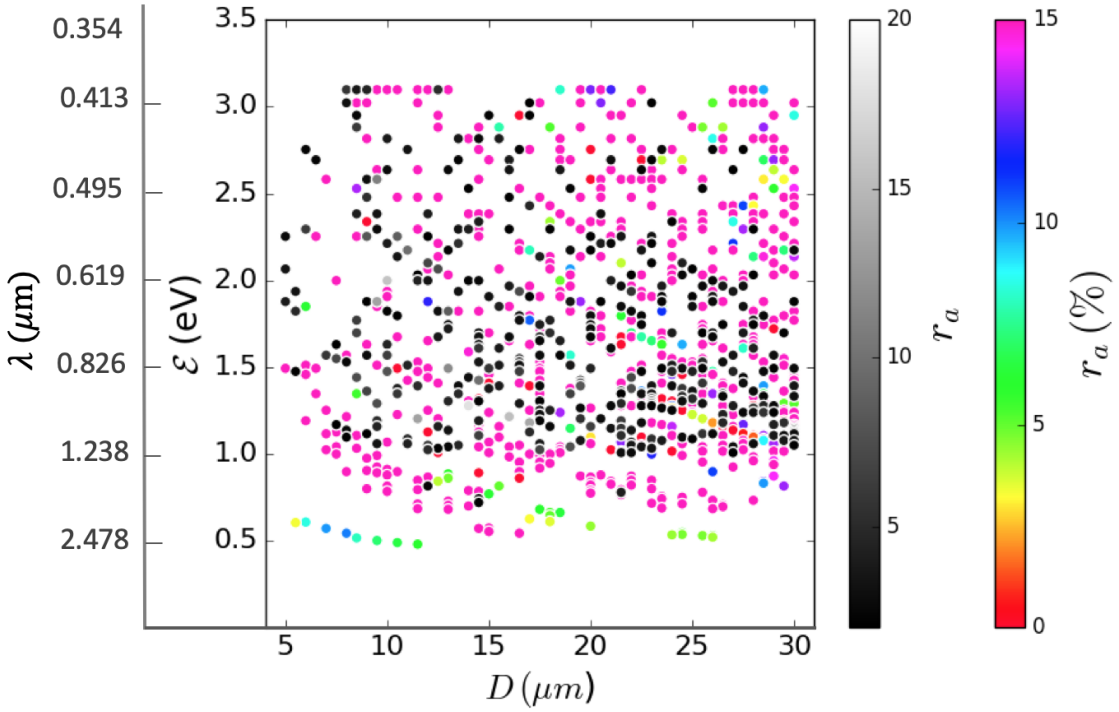

a) The ratio r_a (TOR/Mie) for the absorbed cross section (Reprinted with permission from Yaacoub et al. (2019) ©The Optical Society of America)

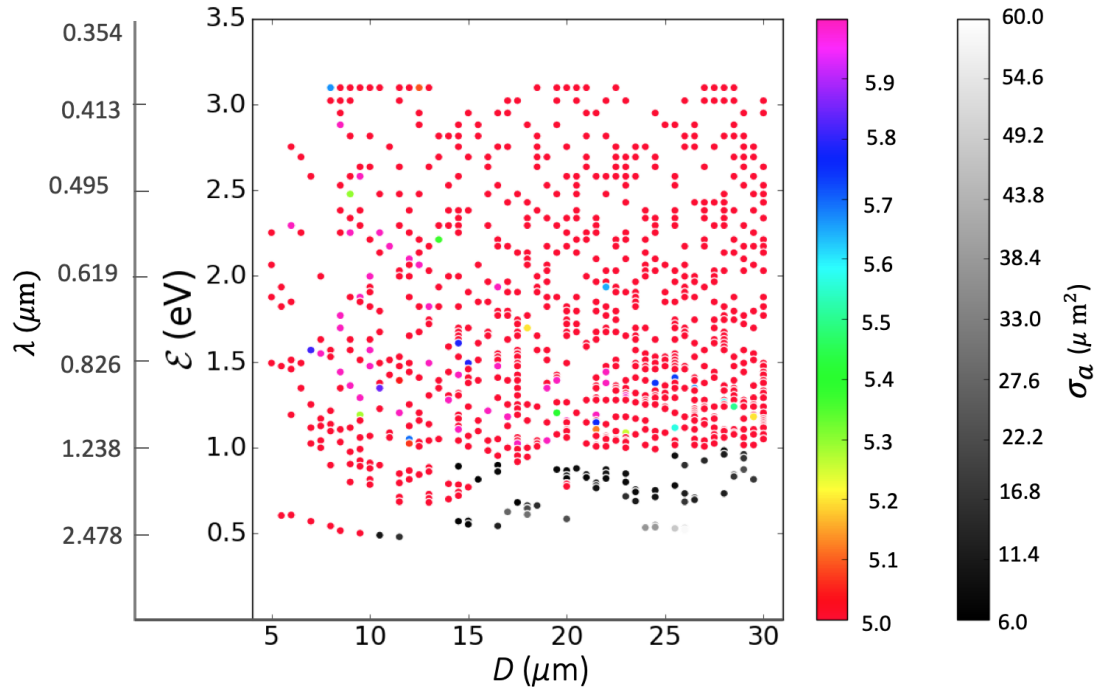

b) The absorbed cross section given by the Mie theory

Figure 4.16: Similar to Figure 4.14 but for the absorption cross sections

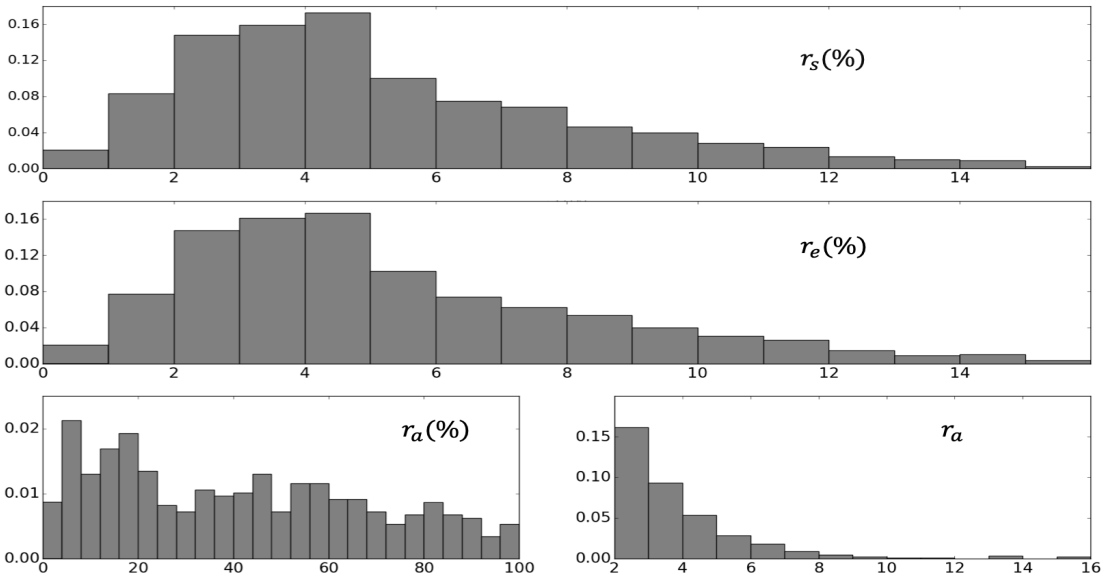

Figure 4.17: Probability density functions of the cross section ratios for scattering, extinction and absorption (Reprinted with permission from Yaacoub et al. (2019) ©The Optical Society of America).

Figure 4.17 displays the probability density functions (pdf) of r_s, r_e and r_a of the previous Figures 4.15, 4.14 and 4.16 and so shows how dispersed are the values of these ratios in the (simulated) sample considered herein. For the first two histograms, the scattering and the extinction, the ratios start to increase highly up to reaching their maximum around $[3\%, 5\%]$, then decrease slightly until they reach a value of 16% with a very small value of pdf.

Absorption ratios are divided into two histograms: one that presents the ratios lower than 100% and another for higher ratios (*i.e.* greater than 100%). The first histogram is more uniform from the previous histograms. The second histogram shows a quick decrease of the pdf values.

II . 3 Comparison of the differential cross sections

The natural intensity of light is one of the most important elements in atmospheric optics. This importance manifests in the proportional relation between the natural intensity of light and the scattering amplitude.

The parallel and perpendicular scattered intensities of light respectively, $I_{\parallel}^{(s)}$ and $I_{\perp}^{(s)}$ are the components of the normalized natural intensity, and as the formulas 2.26 and 2.27 show, the scattering amplitude is integrated over the range ℓ. For TOR natural intensity, ℓ_{TOR}

is treated as a TOR, and all the other ℓ are treated with the Mie theory. For Mie natural intensity, the whole range of ℓ is calculated using the Mie theory.

For the droplet considered before ($D = 26.5\mu$m and $\mathcal{E} = 1.0156\,$eV) one value of resonance has occurred at $\ell = 77$. To calculate the natural light intensity by taking into account TOR for this droplet, it is sufficient to replace the Mie's partial light intensity at $\ell = 77$ by TOR calculation and add all the other ℓ calculated by the Mie theory.

Figure 4.18 displays the ratios (and the logarithmic ratios presented in the frame) of $I_{TOR}(\theta)/I_{Mie}(\theta)$ of the scattered light intensity *vs.* the scattering angle θ. Intensities $I_{TOR}(\theta)$ and $I_{Mie}(\theta)$ are easily calculated from the scattering amplitudes introduced in section II . 2 and by the Mie theory (see (Born and Wolf, 2006)) respectively. Since the scattered intensity is directly proportional to the differential scattering cross section, these ratios can be considered as the ratios of the scattering cross section.

The absolute value of the scattered intensity is helpful to understand the ratios, and to examine if high ratios belong to high absolute values.

Figure 4.19 illustrates the absolute value of the logarithmic intensity of Mie theory for the same droplet ($D = 26.5\mu$m and $\mathcal{E} = 1.0156\,$eV) presented in figure 4.18. Figure 4.19 underlines the difference between the calculated values of I_{TOR} and I_{Mie}. The latter curves match perfectly the usual Mie intensities encountered by the literature. The choice of the logarithmic scale is due to the fact that the scattered light intensity of Mie is used to be presented in logarithmic scale.

As Figure 4.18 illustrates, $I_{TOR}(\theta)/I_{Mie}(\theta)$ is often higher than 1 and, on average, the ratio increases with θ. For very low scattering angle ($\theta < 3°$), $I_{TOR}/I_{Mie} \approx 1$ such value of θ correspond to corona. The highest values of the natural intensity are around $\theta = 170, 180$. This result is in total agreement with the Nussenzveig (2002)'s assumption that the glory, which is mainly a back-scattering effect, has a tunneling origin. The oscillating behavior observed in this plot is not surprising: it comes from the angular dependence of the scattered intensity of the Legendre polynomials.

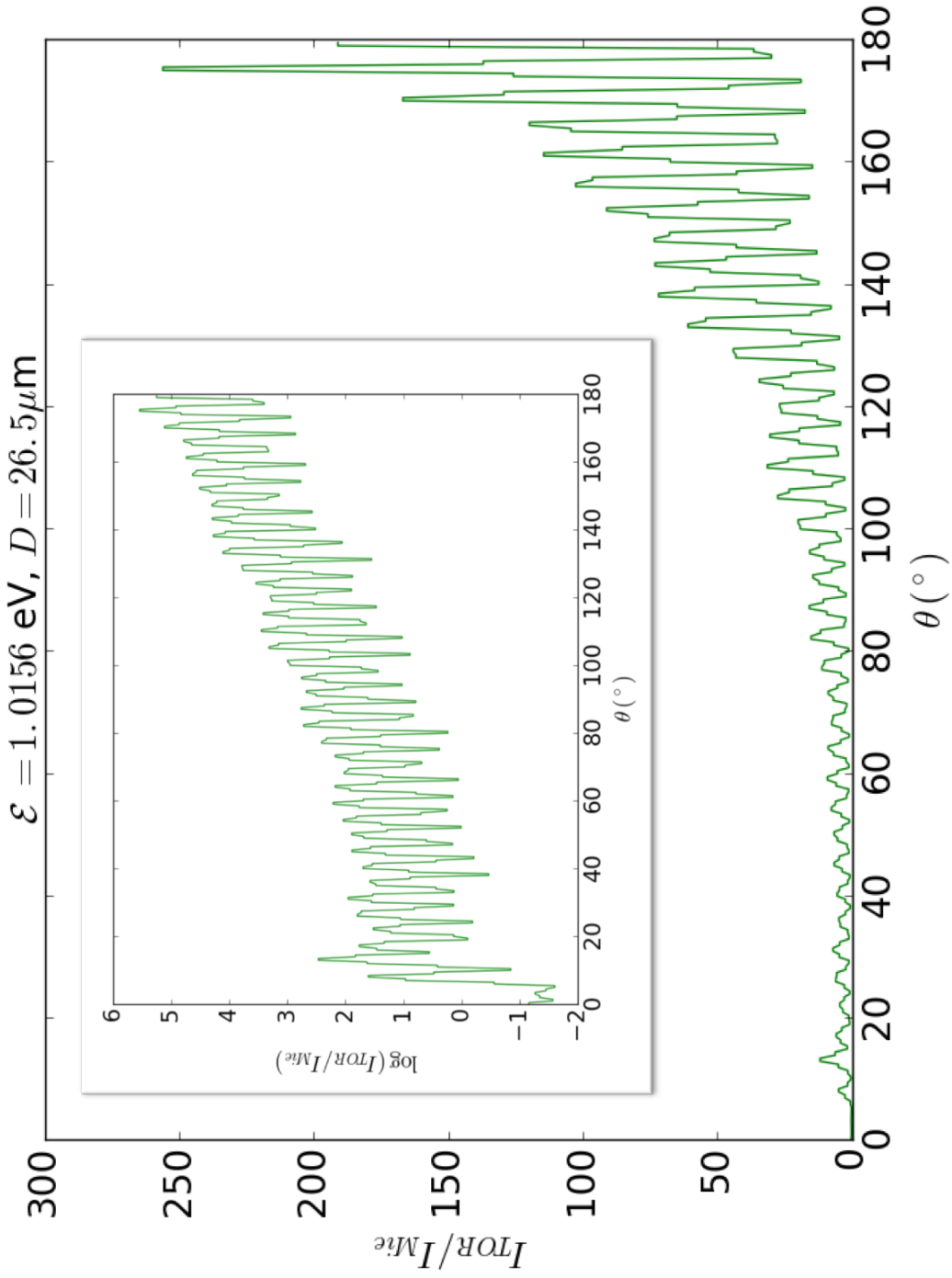

Figure 4.18: Ratio of the scattered intensity $I_{TOR}(\theta)/I_{Mie}(\theta)$ (and in the inside frame the logarithmic ratio of the scattered intensity $\log(I_{TOR}(\theta)/I_{Mie}(\theta))$ is presented) *vs.* scattering angle θ, for a droplet of diameter $D = 26.5\mu$m and an incident energy $\mathcal{E} = 1.0156\,\text{eV}$.

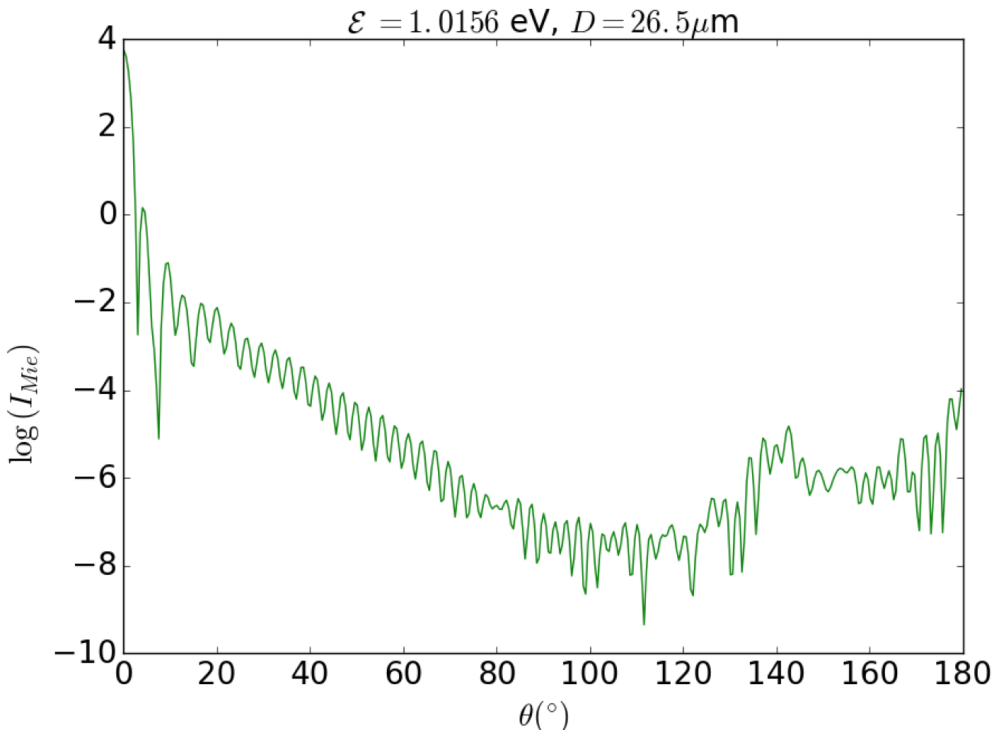

Figure 4.19: The logarithmic scattered intensity of Mie calculation I_{Mie} *vs.* θ of Figure 4.18.

One of the most illustrative results is given in Figure 4.20. This figure presents the polar diagram of the scattered light as predicted by Mie theory (presented in color blue, first row) and with TMM calculation (presented in color red, second row). Note that it is the same results of I_{TOR} and I_{Mie} calculated in this segment, but presented in polar plot. The first plot in each row presents the original plot of I_{Mie} and I_{TOR} and the followed plots are zoomed-in to show better the shape and the difference between the two calculation. Plot (a) shows the insignificant scattered light at back-scattered angles. Contrary to what plot (d) shows, the scattered light around $\theta = 0^\circ$ similar to the back-scattered angles with a remarkable intensity. The first three plots show the form of scattered light that match very well the regular scattered light intensity of Mie calculation. While the last three plots introduce a new, uniform and more intense, form of scattered light for the TMM calculation – an intense light intensity that can explain the existence of glory.

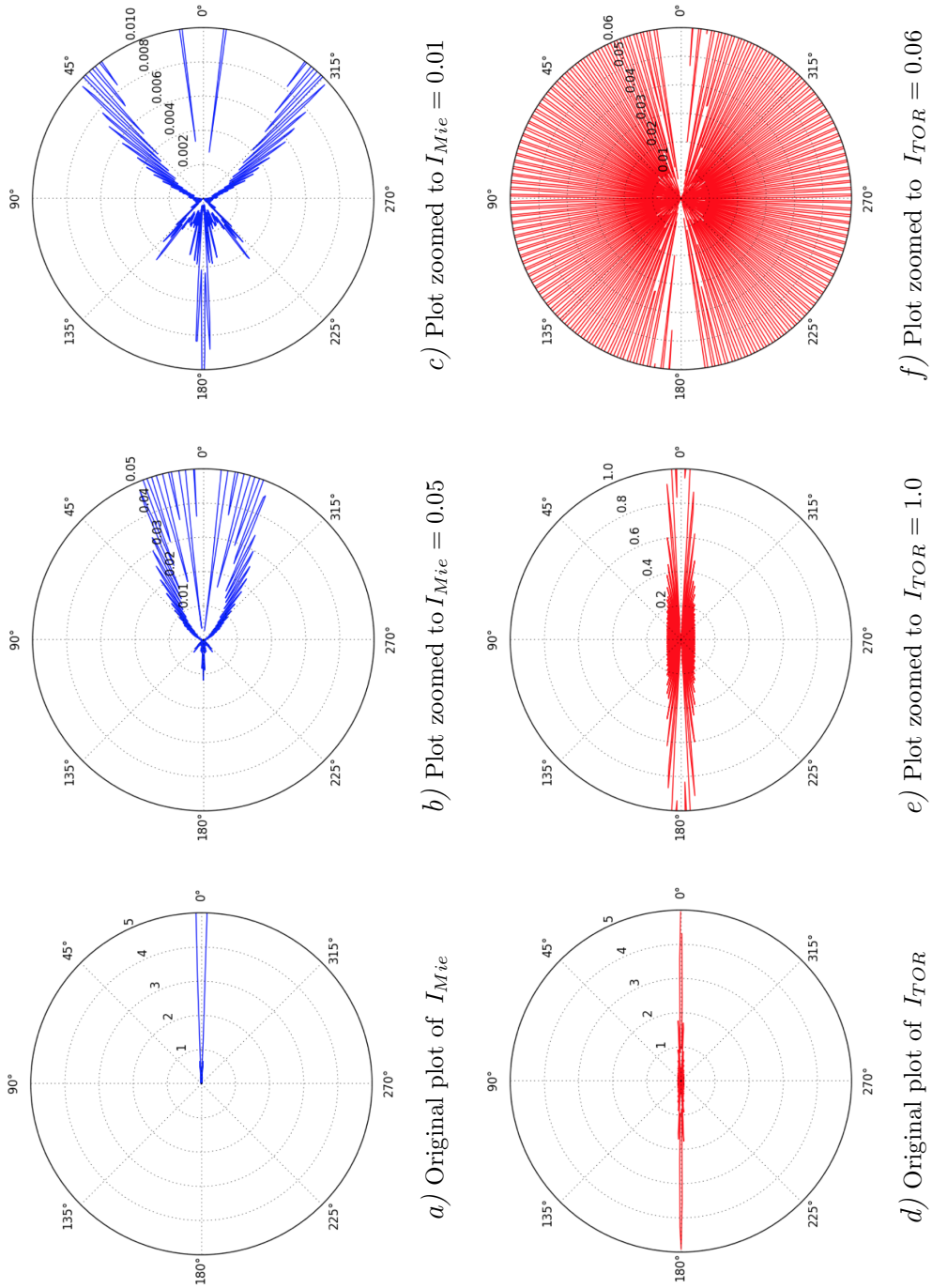

a) Original plot of I_{Mie} *b)* Plot zoomed to $I_{Mie} = 0.05$ *c)* Plot zoomed to $I_{Mie} = 0.01$

d) Original plot of I_{TOR} *e)* Plot zoomed to $I_{TOR} = 1.0$ *f)* Plot zoomed to $I_{TOR} = 0.06$

Figure 4.20: the light intensity *vs.* θ calculated for a droplet of diameter $D = 26.5\mu$m and an incident energy $\mathcal{E} = 1.0156\,\text{eV}$ **(first row)** within Mie prediction and **(second row)** within the TMM.

III. THE CLOUD DISTRIBUTION

In the case of POLDER, or other similar satellite (as 3MI) and also airborne or ground-based, cloud observations, light scattering does not concern only a single droplet but instead a population of numerous droplets with various diameters and refractive indices. In order to quantify the impact of TOR occurrences in such a context, the cross sections when TOR are taken into account are compared to those when TOR are not considered (by applying Mie theory). The values of refractive index are calculated by interpolation as mentioned in subsection I . 1 .

III . 1 Droplet population

Different droplet size distributions (DSD) can be chosen to characterize a droplet population. A realistic DSD, typical of warm clouds, is the gamma modified distribution (Pruppacher and Klett, 1997):

$$N_d(D) = 10^{-4} A \left(\frac{D}{2}\right)^2 \exp\left(\frac{-B\,D}{2}\right) \tag{4.1}$$

where A and B are two constants. The quantity $N_d(D)$ represents the number (per unit volume) of droplets of diameter D. The two constants are, if ρ_w denotes liquid water density (taken at $1\,\mathrm{g\,cm^{-3}}$: $A = 2.27 \times 10^{-8}\, W_l/(\rho_w\, \overline{D}^6)$ and $B = 6/\overline{D}$, $W_l\,(\mathrm{g\,cm^{-3}})$ being the mass liquid water content and $\overline{D} = 2.14 \times 10^{-7}\, W_l/(\rho_w\, N_t)^{1/3}$ the mean diameter of the DSD – $N_t\,(\mathrm{cm^{-3}})$ is the total number of droplets. Thus, giving N_t and W_l, which are readily measurable physical quantities, and the range of droplet diameters D, the DSD is completely determined. The maximum diameter is chosen at 30μm (warm cloud droplet). Figure 4.21a displays an example of such a DSD (Equation 4.1).

For the next calculation, it has been assumed that: (1) each droplet is a homogeneous dielectric (the TMM and Mie theory can be used); (2) each droplet is optically independent from the other (clouds are completely disorganized media); (3) droplets present the same optical index (same temperature, same pressure, and no aerosols are dissolved or included in the droplets); (4) droplets are centered at the same point. This assumption is only for convenience in the management of the calculation. It is not a severe assumption since, at remote distances of observation, the exact positions of each droplet inside the resolution volume is not of crucial importance.

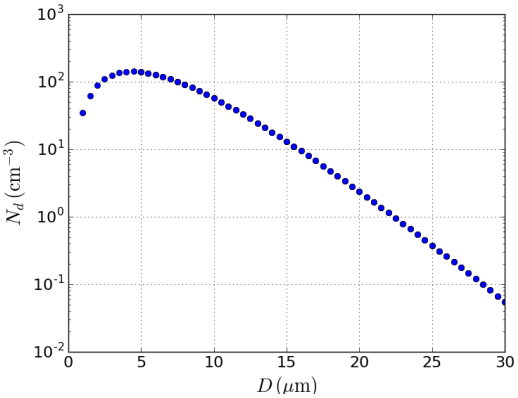

a) Warm cloud droplet size distribution

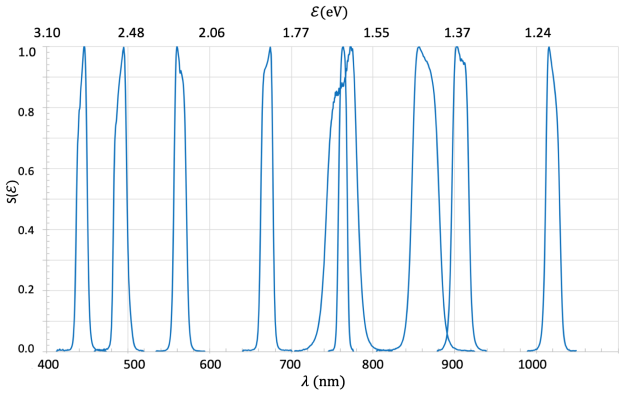

b) Polder instrument response

Figure 4.21: **(a)** Warm cloud droplet size distribution (Equation 4.1) with $N_t = 574\,\mathrm{cm}^{-3}$ and $W_l = 0.2\,\mathrm{g\,cm}^{-3}$, **(b)** POLDER instrument responses $S(\mathcal{E})$ in % for the nine channel of POLDER

III . 2 Cross section comparisons

Since droplets are optically independent from each other, the cross section of the droplet population, at a given incident light energy $\mathcal{E}$, is the *sum* of each individual (droplet) cross section. The energies $\mathcal{E}$ considered hereafter are those of the nine POLDER channels (Figure 4.21b). These channels present a width (full width at half maximum) between 10 and 40 nm around, *viz.* a width in terms of energy of the order of 0.1 ev approximately. Since TOR width Γ are around 10^{-3} eV, each POLDER channel is expected to have several values of TOR. For each POLDER channel, the procedure for cross section computations is the following:

1. A POLDER channel is initially chosen and, for each energy $\mathcal{E}$ in this channel, TOR are searched for the droplet population. To do that, each diameter in the DSD is considered separately; for a given D, the values of ℓ that give rise to a TOR are determined using the methodology defined in Section I.. Let us denote these values, for instance, ℓ_1, ℓ_2 (2 TOR occurrences). Resonance widths are also obtained.

2. Cross sections are then computed for the population according to:

$$\sigma_\alpha(\mathcal{E}) = \sum_i N_d(D_i) \sum_{\ell=0}^{\ell_{max}} \sigma_{\alpha,\ell}(D_i,\, \mathcal{E})$$

where α stands for 's' (scattering), 'a' (absorption) and 'e' (extinction). The series $\sum_\ell \sigma_{\alpha,\ell}$ has to distinguish the value of ℓ that give rise to a TOR from those that do not. For the former, Equations 2.45 and 2.46 are used, while for the latter, Mie theory (Equation 2.25) are obviously used. It follows, if there are, for instance, 2 TOR occurrences at ℓ_1 and $\ell_2 > \ell_1$, $(D_i, \mathcal{E})$ being fixed:

$$\sum_{\ell=0}^{\ell_{max}} \sigma_{\alpha,\ell} = \sum_{\ell=0}^{\ell_1-1} \sigma_{\alpha,\ell}^{(Mie)} + \sigma_{\alpha,\ell_1}^{TOR} + \sum_{\ell_1+1}^{\ell_2-1} \sigma_{\alpha,\ell}^{(Mie)} + \sigma_{\alpha,\ell_2}^{TOR} + \sum_{\ell_2+1}^{\ell_{max}} \sigma_{\alpha,\ell}^{(Mie)} \tag{4.2}$$

3. The cross section for the population considered is then multiplied by the POLDER instrument response $S(\mathcal{E})$ of the wavelength in order to weight the contribution of $\sigma_\alpha(\mathcal{E})$ in the POLDER channel. So the total cross section is written:

$$\sigma_\alpha = \sum_j \left[S(\mathcal{E}_j) \sum_i N_d(D_i) \sum_{\ell=0}^{\ell_{max}} \sigma_{\alpha,\ell}(D_i, \mathcal{E}_j) \right] \tag{4.3}$$

4. The points (1), (2), and (3) are repeated *without* taking into account any TOR, and so using only the Mie theory. That gives:

$$\sigma_\alpha^{(Mie)} = \sum_j \left[S(\mathcal{E}_j) \sum_i N_d(D_i) \sum_{\ell=0}^{\ell_{max}} \sigma_{\alpha,\ell}^{(Mie)}(D_i, \mathcal{E}_j) \right] \tag{4.4}$$

The ratio $r_\alpha = \sigma_\alpha / \sigma_\alpha^{(Mie)}$ quantifies the impact of TOR occurrences. Since the COT is directly proportional to the total cross section, one deduces: $COT/COT_{Mie} = r_e$. In addition, the SSA is such that: $SSA/SSA_{Mie} = r_s/r_e$.

As mentioned in the section of one droplet (especially in the subsection II . 2), the comparison between the cross sections of the TMM and the Mie theory is by presenting the ratios between the two calculation. The illustration of an absolute value leads to more comparable values.

Table 4.1 summarizes the ratios of cross sections obtained for each POLDER channel. It appears clearly that absorption is much more important when considering TOR, since the values of r_a range from 3.5% to 27.1%. Such percentages are easily understandable since tunneling resonances lead to substantial increases of the light energy inside the droplet, and so potentially to important absorption. These values are consistent with that obtained in Nussenzveig (2003). Although the absolute values calculated by Mie (σ_a^{Mie}) are relatively

small, which is related to the small imaginary part (κ) of the optical index $(\underline{n})$.

The ratio of extinction r_e is of the same order of r_s because Mie absorption cross section is relatively low in the spectral domain considered. In fact, since $\sigma_e = \sigma_s + \sigma_a$, one has:

$$r_e\,\sigma_e^{(Mie)} = r_s\,\sigma_s^{(Mie)} + r_a\,\sigma_a^{(Mie)}$$
$$r_e = r_s\,\frac{\sigma_s^{(Mie)}}{\sigma_s^{(Mie)} + \sigma_a^{(Mie)}} + r_a\,\frac{\sigma_a^{(Mie)}}{\sigma_s^{(Mie)} + \sigma_a^{(Mie)}} \approx r_s$$

since $\sigma_a^{(Mie)} < \sigma_s^{(Mie)}$. As a final remark, note that no general tendency emerges from these values: for a given droplet population, the behaviors of the ratios *vs.* the energy are very difficult to predict since they depend on the TOR strength at a given energy and on the sensitivity of the receiver channel at the location of the TOR. Some TOR can be very strong but with a small contribution to the spectral band because spectral responses for this TOR is very low, and *vice versa*.

Similar orders of magnitudes have been obtained with other DSD. These values concern also the new space-borne instrument 3MI since it has the same spectral bands of observation as POLDER. Only POLDER channels 2 and 4 are not in 3MI. This last instrument can also perform observations in the following extra spectral bands (central wavelengths): 410 nm (3.022 eV), 555 nm (2.232 eV), 754 nm (1.643 eV), 1 370 nm (0.904 eV), 1 650 nm (0.750 eV), and 2 130 nm (0.582 eV). As for POLDER, the bandwidths (full width at half maximum) of these bands ranges from 10 to 40 nm. Detailed data of sensitivity were not available at the time of writing this manuscript to calculate explicitly, as above for POLDER, the different ratios r_e, r_s, and r_a. However, values of the same order of magnitudes, or higher, can reasonably be expected, since (1) 3MI spectral band main characteristics are not substantially different from that of POLDER and (2), as seen above (*e.g.* Figure 4.12), TOR proliferate for such spectral interval these bands.

III . 3 Ratio of the angular distribution of the scattered intensity

As we explained in subsection II . 3 : the scattered intensity is integrated over the range ℓ, so we used in this section the same methodology used previously to calculate the intensity for one single droplet: for TOR natural intensity, ℓ_{TOR} is treated as a TOR – we used the formulas of the scattering amplitudes given by the section II., and all the other ℓ are treated as Mie – we used the formulas given by the Mie theory (see (Born and Wolf, 2006)), and for

Channel number	$\lambda_{\text{interval}}$(nm)	$\mathcal{E}_{\text{interval}}$(eV)	r_s (%)	r_a (%)	r_e (%)	$\sigma_s^{Mie}(\mu m^2)$	$\sigma_e^{Mie}(\mu m^2)$	$\sigma_a^{Mie}(\mu m^2)$
1	412 – 473	2.262 – 3.01	0.942	13.6	0.942	7.82×10^5	7.82×10^5	0.2694
2	535 – 594	2.09 – 2.32	0.980	21.1	0.980	6.05×10^6	6.05×10^6	2.278
3	879 – 939	1.32 – 1.41	1.007	26.5	1.010	8.84×10^6	8.84×10^6	489.58
4	989 – 1049	1.18 – 1.25	0.932	25.5	0.935	6.66×10^6	6.67×10^6	1588.79
5	705 – 824	1.51 – 1.76	1.030	26.9	1.031	1.48×10^7	1.48×10^7	198.05
6	745 – 776	1.60 – 1.66	1.048	27.1	1.049	4.197×10^6	4.197×10^6	56.77
7	459 – 520	2.39 – 2.70	0.932	18.8	0.932	6.22×10^6	6.22×10^6	1.13
8	640 – 701	1.77 – 1.94	1.00	3.5	1.00	6.07×10^6	6.07×10^6	13.64
9	804 – 924	1.34 – 1.54	1.070	26.1	1.072	1.349×10^7	1.349×10^7	380.48

Table 4.1: Ratios r_s, r_a, and r_e and the absolute values of Mie calculation σ_s, σ_e and σ_a obtained for each POLDER channel – see text for details (Adapted with permission from Yaacoub et al. (2019) ©The Optical Society of America).

Mie natural intensity, the whole range of ℓ is calculated as Mie (we used the formulas given by the Mie theory).

Similarly to the previous subsection III . 2 , each droplet contribution is weighted by the population $N_d(D)$ and the POLDER channel responses $S(\mathcal{E})$.

Figure 4.23 displays the ratios (and the logarithmic ratios, presented in the frame) of $I_{TOR}(\theta)/I_{Mie}(\theta)$ of the scattered light intensity *vs.* scattering angle θ for the droplet population considered before in Figure 4.21a for all the POLDER channels. The goal of presenting the logarithmic ratios of I_{TOR} and I_{Mie} serves the Figure 4.22. Although the logarithmic ratios of TOR and Mie need the absolute values of scattering intensity to illustrate the difference and to examine if the high ratios belong to high absolute values. Therefore Figure 4.22 presents the absolute values of scattering intensity of Mie, to be compared with the inside frame of Figure 4.23. The choice of the logarithmic scale is due to the fact that the scattered light intensity of Mie is used to be presented in logarithmic scale.

The ratios I_{TOR}/I_{Mie} increase (not monotonically) with the increases of θ . At very low scattering angles ($\theta < 3°$) the ratio $I_{TOR}/I_{Mie} \approx 1$. The pronounced difference in ratios shows at the scattering angles $\theta > 60°$ corresponds to low values of $\log(I_{Mie})$. A remarkable decrease of ratios at $\theta = 140°$, which corresponds to the rainbow; where I_{Mie} presents a peak (a caustic), which is relatively close to I_{TOR} .

The ratio I_{TOR}/I_{Mie} increases rapidly again after $\theta = 140°$ especially for back-scattering angles $\theta > 170°$ (the interval fo diffusion angles between $170°$ and $180°$ correspond to the glory). This is in agreement with the Nussenzveig (2002)'s assumption that the glory, which is mainly a back-scattering effect, has a tunneling origin. For scattering angles far from forward scattering, $I_{Mie}(\theta)$ is relatively low, especially for $\theta > 80°$, so that it is not surprising to get large values of I_{TOR}/I_{Mie} . The oscillating behavior observed in this plot is not surprising: it comes from the angular dependence of the scattered intensity on the Legendre polynomials.

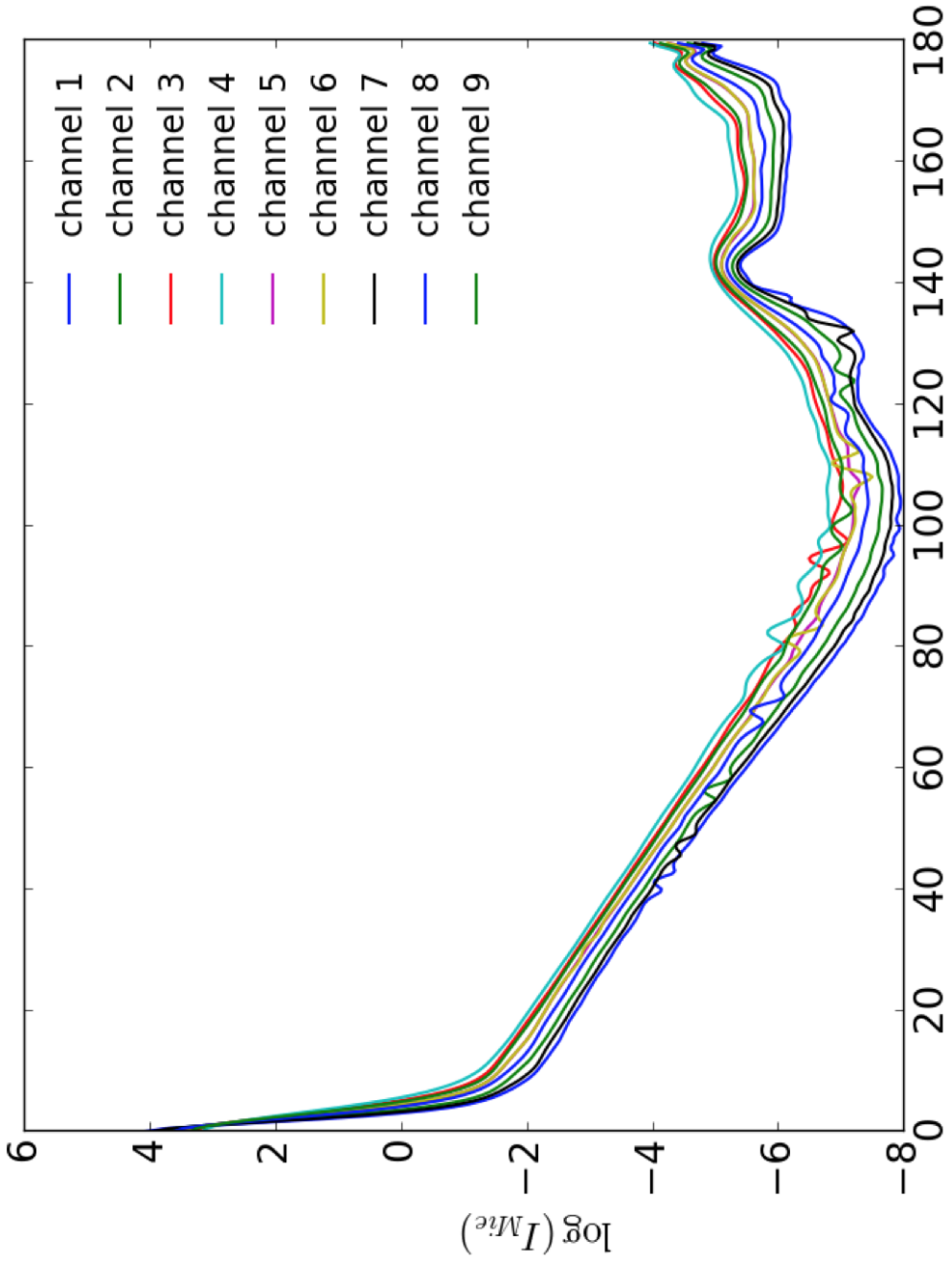

Figure 4.22: The logarithmic scattered light intensity $I_{Mie}(\theta)$ *vs.* scattering angle θ, for distribution 4.21a for the nine channel of POLDER

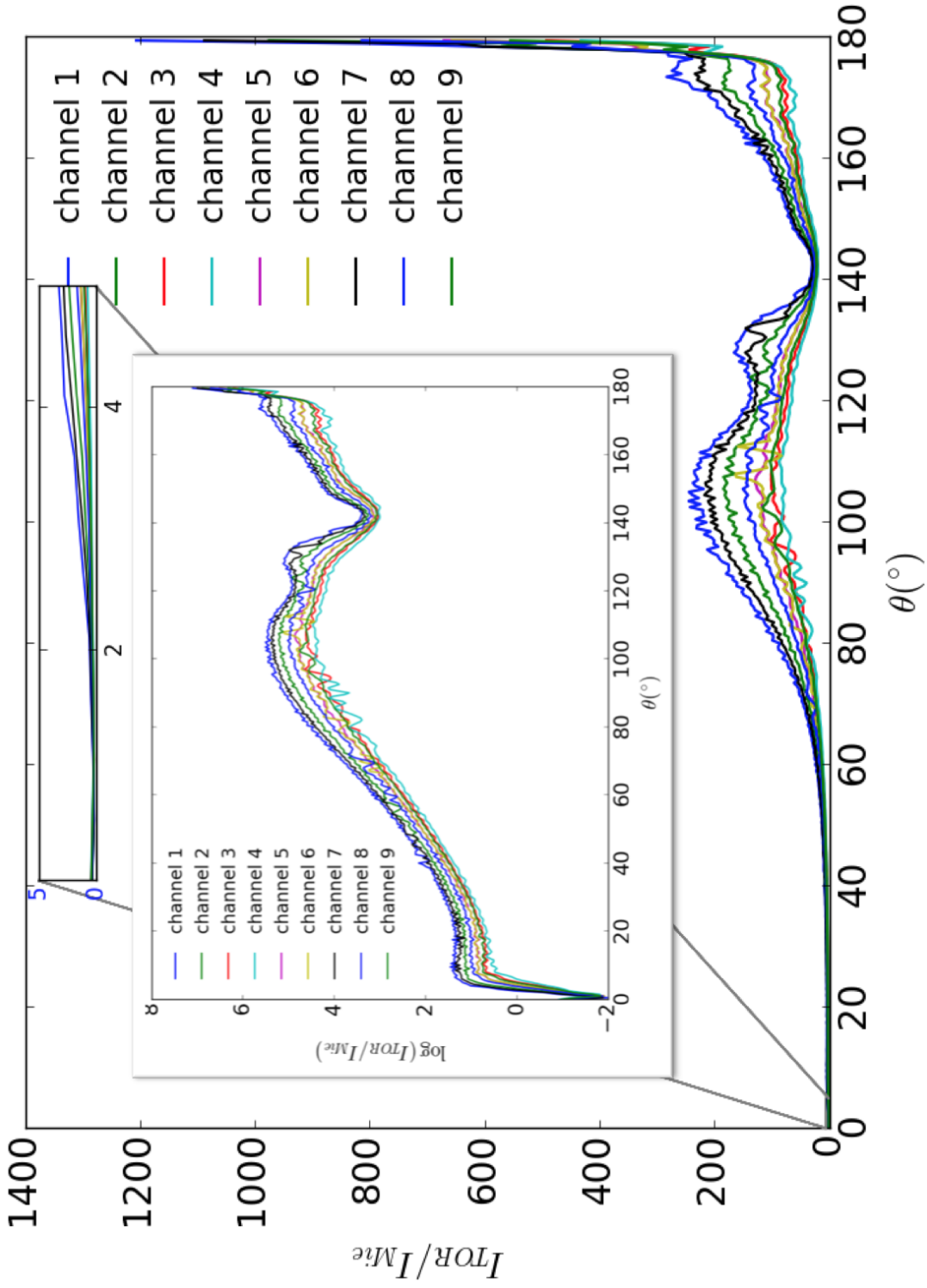

Figure 4.23: Ratio of the scattered intensity $I_{TOR}(\theta)/I_{Mie}(\theta)$ *vs.* scattering angle θ. The inside frame is $\log(I_{TOR}(\theta)/I_{Mie}(\theta))$ *vs.* scattering angle, for distribution 4.21a for the nine channel of POLDER (Reprinted with permission from Yaacoub et al. (2019) ©The Optical Society of America)

CONCLUSION

This chapter presented the solution of the TMM that has been introduced in the previous chapter, where some characteristics, criteria and some conditions were set to identify and localize the resonances of TOR. Subsequently, we have tested those criteria while calculating the light energy for a TOR and non-TOR, by the TMM and the Mie theory. The light density was calculated in one dimensional and two dimensional. This illustration has showed the resonance of tunneling origin.

A novel part is achieved, presenting the TOR occurrences and corresponding of the couple $\mathcal{E}(\text{eV})$ and $D(\mu\text{m})$. This chapter has a substantial part of comparison between the TMM calculation and the Mie calculation, starting with a simple case of one droplet and then using a specific cloud droplet distributions for the nine channels of POLDER. We have calculated, with TMM and Mie prediction, the cross sections, the cloud optical thickness, the single scatter albedo and finally the scattered light. The calculation in both cases led to one result: the TOR impact the different cross sections of a droplet and of a cloud droplet distribution, in the visible and the infrared. The absorption cross sections of TMM can be 30% more than the Mie calculation.

CHAPTER 5 Synthesis & perspectives

The tunneling effect has been recently proposed to explain the atmospheric glory, *viz.* the strong near back-scattering signal of illuminated droplets that manifests by a circular iridescence around the projected shadow over a liquid cloud of any illuminated object. Tunneling occurrences produce very sharp resonances that we have called tunneling optical resonances (TOR). The work presented in this manuscript is further off the atmospheric glory and emphasized on light-droplet interaction when taking into account TOR. Precisely, the aim of this study is to develop an efficient method that allows the calculation of TOR occurrences and the characteristics of this kind of resonances for spherical water droplets. In addition, the impact of TOR on remote sensing, like POLDER observations of cloud droplet population, has been estimated and presented in order to obtain the deserved attention.

Because the glory provided us with the pretext to examine the importance of TOR and so to revise the usual practices in atmospheric optics, a general introduction of the glory has been presented. First we have recalled the history of this spectacular phenomenon which inspired painters and poets at the very beginning and we have indicated the several scientific attempts to explain it. In addition, we have showed photos of the glory from the POLDER/PARASOL satellite confirming this way that the glory is not due to ice-light-interactions but rather involves the pure liquid phase.

Regarding the theoretical aspects, we have presented some of the fundamental formulas of light-droplet interactions and the important notion of cross section. In particular, we have envisioned the Helmholtz's equation of the stationary radial wave function as a one dimensional Schrödinger equation and introduced the effective potential energy or "optical potential" to characterize the light-droplet interaction. In particular, the partial wave analysis has been introduced, since it is useful for symmetrical interactions, like this case herein of light-droplet scattering. This approach has been underlined in this manuscript. Among these

solutions, the concept of TOR has been detailed and we have illustrated the parameters for which TOR depend on such as the incident light energy (or wavelength in vacuum), the partial wave order, and the droplet diameter. The scattering amplitude and the cross sections expressions corresponding to the TOR have been given explicitly. Two derived parameters used in atmospheric optics for practical uses have also been recalled: the cloud optical thickness and the single scatter albedo.

In order to find the solutions of the radial wave equation, and especially to identify TOR, the transfer matrix method (TMM) has been introduced. This technique is used in various domains of Physics because of its efficiency to deal with one-degree-of-freedom linear problems. In the present context of light-droplet scattering, the TMM consists in dividing the "optical potential" into elementary steps, each one is characterized by a 2×2 matrix of determinant one. Two consecutive steps are separated by a region of uniform potential energy characterized in a similar way by 2×2 matrix of unit determinant. The judiciously ordered product of these two elementary matrices gives a matrix, called the *abcd*-matrix, which contains all the information that correspond to the light-droplet interaction. Especially, the nullity of the fourth element d of this matrix – or for numerical convenience the minimum of $\ln|d|$ – identifies the quasi bound (or confined) states (*i.e.* the TOR energy location). The TMM also informs about the sharpness of the TOR by enabling the determination of the halfwidh. By construction, the *abcd*-matrix allows to obtain the wave function and so the light density over the whole space. At the end, from these different information, the TMM permits to calculate the scattering amplitude and the different cross sections.

After illustrating this approach for one droplet and defining two important numerical criteria for the TOR identification, the TOR for different droplets (for typical sizes from 5 to $30\,\mu$m) and different light energy (from the UV to the IR of the electromagnetic spectrum) have been characterized. TOR are particularly characterized by a very important sharpness and, as expected, by a strong enhancement of the light density inside the droplet compared to the Mie theory. In the last part of this manuscript, the realistic situation of a cloud droplet population, as it would be observed by the POLDER radiometer, has been considered. Especially, considering each of the nine POLDER channels, with their true response profiles, the cross sections when taking into account TOR and without taking into account TOR have been compared for typical warm cloud droplet diameter distributions. We have concluded that TOR leads to substantial enhancement with respect to the Mie theory, especially for the differential cross section (*i.e.* light intensity *vs.* scattering angle) at large angles,

especially near the back-scattering domain and for the absorption cross section which can be strengthened by at most 30%. Scattering and extinction cross sections are also higher than those of the Mie theory but in a less extent, although not negligible. The conclusion of this study, which has been recently accepted in JOSA, is that tunneling resonances should be considered more explicitly and systematically in atmospheric optics, namely in radiative transfer calculation and remote sensing. No tendency emerges that would help to quantify the precise impact of TOR on observations and modeling, because it depends on the strength of the resonance, its sharpness, and its position with respect to the spectral responses of the instrument.

To conclude this work, some perspectives are presented below:

1) In this manuscript, we have considered only optically homogeneous droplets of micrometric size. Non spherical objects are not concerned. However, the approach may be used for scatterers for which an appropriate equivalent sphere can be defined and for scatterers of almost-spherical approximated shape. In these cases, one has to keep in mind the error in the scatterer shape that is introduced at the beginning of the analysis. Obviously, the spherical assumption is all the more restrictive than deviations from the spherical geometry are important. Moreover, although the optical index was that of liquid water, the same methodology holds for ice crystals and aerosols provided that they can be assumed spherical. In addition, this approach is also convenient for heterogeneous spherical scatterers, as for instance: (1) a spherical wet aerosol, *i.e.* covered by a thin film of water, (2) a multilayered scatterer, *i.e.* made of several concentric spherical layers of different optical index, (3) scatterers with $r-$dependent optical index $\underline{n}(r)$. Cases (1) and (2) are illustrated in Figure 5.1; the effective potential energy is:

$$\mathcal{E}_{p,ef} = \begin{cases} 1 - n_i^2 + \dfrac{\ell(\ell+1)}{k_0 r^2} & r_{i-1} < r < r_i \\ \dfrac{\ell(\ell+1)}{k_0 r^2} & r > r_N \end{cases} \tag{5.1}$$

with $i = 1, ..., N$, with N the number of layers ($N = 2$ for case (1)).

For case (3), n is substituted by $n(r)$. The case of aerosol-polluted droplets (*e.g.* by soots) is important: it is expected to significantly increase absorption Zender and Talamantes (2006). Optical index gradients at the scatterer edge, *viz.* between the scatterer and surrounding can also be addressed. For example, in the realistic case of a droplet surrounded by a thin layer of water vapor, with a gradient of absolute humidity, the effective potential energy should vary

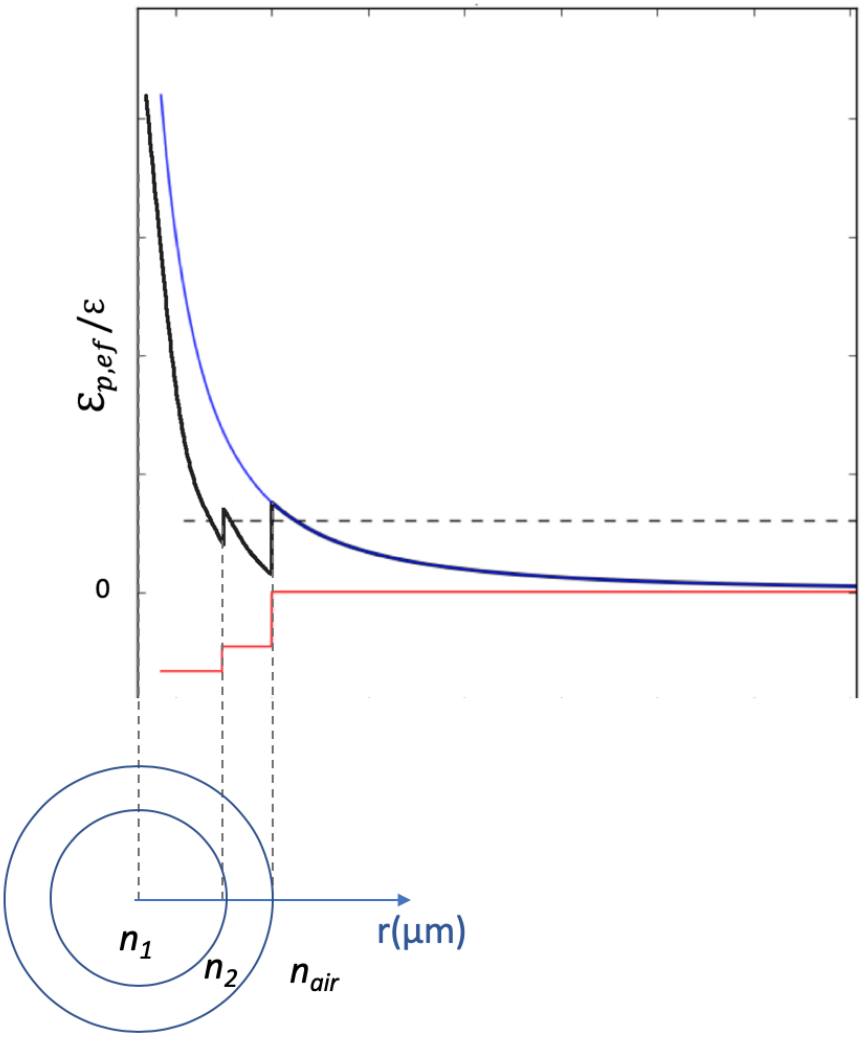

Figure 5.1: Effective potential energy for the case 1 and, similarly for the case 2.

continuously from inside the droplet to its outside. Tunneling resonances (position, width) are impacted by all of these effects. Generally speaking, the methodology and the results presented in this work pave the way to further studies about more complex scatterers (in terms of shape and physical heterogeneity). From what have been obtained in this thesis with respect to TOR importance, it is desirable that further studies focus on other scatterers since they are also suject to TOR (*e.g.* Bi et al., 2015, for ice crystals).

2) Another important result is that TOR location is very accurate since halfwidths are typically $\Gamma \sim 10^{-2}\,\mathrm{eV}$ at most, *i.e.* $\Delta\lambda_0 \sim 2\,\mathrm{nm}$ if $\lambda_0 = 500\,\mathrm{nm}$ and $\Delta\lambda_0 \sim 8\,\mathrm{nm}$ at $\lambda_0 = 1\,\mu\mathrm{m}$. Such values are lower than the usual bandwidths of the commonly used instruments (*e.g.*

40 nm for POLDER channels). It follows that this work requires also a higher spectral resolved future instrument at a judiciously chosen spectral band taking into account the tunneling resonances. In agreement with what other authors indicated (*e.g.* Zender and Talamantes, 2006; Nussenzveig, 2003), neglecting sharp resonances in the instrumental bands of observation (or narrower) can cause substantial biases in remote sensing retrievals.

3) In this work, no attempt has been made to invert the signal coming from the glory, nor to exploit the signal from TOR. An appropriate inversion method would be welcome in the future to retrieve the "optical potential", *i.e.* the optical index and the size of the scatterers. The Gelfan-Levitan-Marchenko equation (*e.g.* Newton, 2002) could be helpful. For the time being, and from a practical point of view, the ratios introduced in this manuscript can be used as look-up tables in order to correct cross sections in atmospheric optics algorithm.

4) Finally, the impact of TOR on radiative transfer, in particular stochastic algorithms (including 3D effects/multiple scattering) should be analyzed, as well as the coherent features of the incident light.

Appendix

2076 Vol. 36, No. 12 / December 2019 / Journal of the Optical Society of America A

Research Article

Journal of the Optical Society of America A

OPTICS, IMAGE SCIENCE, AND VISION

Tunneling optical resonances in light–droplet interactions: simulations of spaceborne cloud droplet observations

Rouba Yaacoub, Olivier Pujol,* and Philippe Dubuisson

Université de Lille, Laboratoire d'optique atmosphérique, 59655 Villeneuve d'Ascq, France
**Corresponding author: olivier.pujol@univ-lille.fr*

Received 31 July 2019; revised 7 October 2019; accepted 22 October 2019; posted 23 October 2019 (Doc. ID 374028); published 25 November 2019

A fruitful approach for light–droplet interaction in atmospheric optics, the quantum optical analogy combined with partial wave analysis, is used to characterize (location, width) very sharp tunneling optical resonances (TORs). For this purpose, a fast and flexible technique of computation, the transfer matrix method, has been developed; it is described herein. This paper proposes explicit calculations of TORs, considering isolated droplets and a droplet population, and so goes further than earlier studies. Applied in the context of POLDER observations, from the visible to the near infrared, it is shown that TORs enhance cross sections with respect to Mie's theory as currently computed in atmospheric optics. Precisely, for a typical warm cloud droplet population, this enhancement can reach almost 30% in the case of absorption. Scattering and extinction cross sections are also higher than those of Mie's theory, but to a lesser extent. As a conclusion, it is suggested that tunneling should be taken into account more explicitly when addressing light scattering by droplets. No scattering inversion technique is investigated in this paper, but for the time being, the results presented can be used as look-up tables (at least orders of magnitude) for practical computations in atmospheric remote sensing. Finally, the approach presented herein is proposed as a perspective to be used in different situations involving other spherical (or almost spherical) scatterers that otherwise should be addressed approximately.

https://doi.org/10.1364/JOSAA.36.002076

1. INTRODUCTION

In atmospheric optics, Mie's theory [1,2] is commonly dedicated to deal with light interaction with a dielectric spherical scatterer (e.g., cloud droplet) of known characteristics (diameter D, optical index $\underline{n} = n + i\kappa$) and so to calculate the optical properties of a population of such scatterers, as, for instance, the cloud optical thickness (COT) or the single scattering albedo (SSA). Such calculations are based on the different cross sections σ (extinction "e," scattering "s," absorption "a"):

$$\sigma_e = \frac{2\pi}{k_0^2}\mathrm{Re}\left\{\sum_\ell (-i)^{\ell+1}\ell(\ell+1)({}^eB_\ell + {}^mB_\ell)\right\}, \quad (1)$$

$$\sigma_s = \frac{2\pi}{k_0^2}\sum_\ell \frac{\ell(\ell+1)^2}{2\ell+1}\left(|{}^eB_\ell|^2 + |{}^mB_\ell|^2\right), \quad (2)$$

$$\sigma_a = \sigma_e - \sigma_s, \quad (3)$$

where i is the imaginary unit ($i^2 = -1$), Re stands for the real part, ℓ is an integer (the meaning will be explained further), and k_0 (in rad m^{-1}) is the angular wavenumber (in vacuum), i.e., $k_0 = 2\pi/\lambda_0$, λ_0 being the wavelength (in m). The complex factors ${}^eB_\ell$ and ${}^mB_\ell$ are expressed in terms of the spherical Bessel function ψ_ℓ and of the spherical Hankel function $\zeta_\ell^{(1)}$ [1]:

$${}^eB_\ell = i^{2\ell+1}\frac{2\ell+1}{\ell(\ell+1)}\frac{\underline{n}\psi'_\ell(\beta)\psi_\ell(\underline{n}\beta) - \psi_\ell(\beta)\psi'_\ell(\underline{n}\beta)}{\underline{n}\zeta_\ell^{(1)'}(\beta)\psi_\ell(\underline{n}\beta) - \underline{n}\zeta_\ell^{(1)}(\beta)\psi'_\ell(\underline{n}\beta)},$$

$${}^mB_\ell = i^{2\ell+1}\frac{2\ell+1}{\ell(\ell+1)}\frac{\underline{n}\psi_\ell(\beta)\psi'_\ell(\underline{n}\beta) - \psi'_\ell(\beta)\psi_\ell(\underline{n}\beta)}{\underline{n}\zeta_\ell^{(1)}(\beta)\psi'_\ell(\underline{n}\beta) - \underline{n}\zeta_\ell^{(1)'}(\beta)\psi_\ell(\underline{n}\beta)}, \quad (4)$$

with $\beta = k_0 D/2$ the size factor. The prime symbol ($'$) indicates derivation with respect to the argument. Equation (3) is deduced from light energy conservation during light–matter interaction. Conversely, Mie's theory is also used for inverse problems in remote sensing to retrieve physical properties of scatterers.

However, the common usage of Mie's theory in atmospheric optics does not consider (to our knowledge) a complete light–droplet interaction by missing some resonances: light in the surrounding of a droplet can penetrate into it and excite very

1084-7529/19/122076-13 Journal © 2019 Optical Society of America

(a) (b)

Fig. 1. Glories observed: (a) photo by Olivier Pujol from an airplane and (b) photo by Philippe Dubuisson from the top of a mountain.

sharp resonances. An evidence of such resonances, which we will call tunneling optical resonance (TOR), is the atmospheric glory [3], viz., the circular iridescence around the projected shadow of an object on a cloud of water droplets, as we can observe in the photos taken by two of the authors (Fig. 1). The glory exists also in the near infrared [4] and can be observed from spaceborne instruments. As an illustration, Fig. 2(a) is an image from the radiometer POLDER (POLarization and Directionality of the Earth's Reflectances; see [5] and [6]), on the PARASOL satellite, showing a glory over a field of liquid clouds. Scattering angles of the glory are close to 180° [backscattering, Fig. 2(b)].

The Brazilian physicist Nussenzveig was the first to attribute a tunneling origin to the meteorological glory [3], and to say that tunneling resonances are misrepresented in the common practices of atmospheric optics, though such resonances could substantially increase the total absorption of water droplets and so of liquid clouds [7]. The argument is that optical computations are performed with a size factor step $\Delta\beta \sim 0.1$ and considering averaged spectral bands—instead of the true spectral response of a detector—determined using only the central wavelength. The example of only *one* droplet of radius 10 μm [7] has roughly estimated that the spectrally averaged increase of the total absorption due to tunneling is around 20%. Another argument for misrepresentation is that TOR has been parameterized (e.g., [8]) without catching the main features of these resonances (viz., high sharpness) ([7]). The importance of $\Delta\beta$ to resolve sharp resonances has also been underlined by [9].

This paper aims at analyzing the impact of TOR in the case of a typical liquid cloud droplet population (and not only one droplet) by taking into account the true spectral response of a detector, herein the different channels of the passive radiometers POLDER and future 3MI (Multi-viewing, Multi-channel, Multi-polarization Imager; see [10]). POLDER (3MI) measurements are (will be) used to retrieve various cloud quantities, e.g., the droplet Mie effective radius [11]. Explicit calculations are made, and no parameterization is introduced herein. To do that, the conditions for which TORs occur are investigated, and TORs are characterized precisely, i.e., the energy $\mathcal{E}_r$ (or wavelength—in vacuum—$\lambda_r = hc/\mathcal{E}_r$, where $h = 6.62607015 \times 10^{-34}$ Js is the Planck's constant and $c = 299792458$ ms^{-1} the Einstein's constant) of a resonance (the subscript "r" refers to resonance) and its corresponding width Γ are determined. For that, an algorithm based on the transfer matrix method (TMM), which is particularly suitable to solve linear one-dimensional (1D) wave propagation

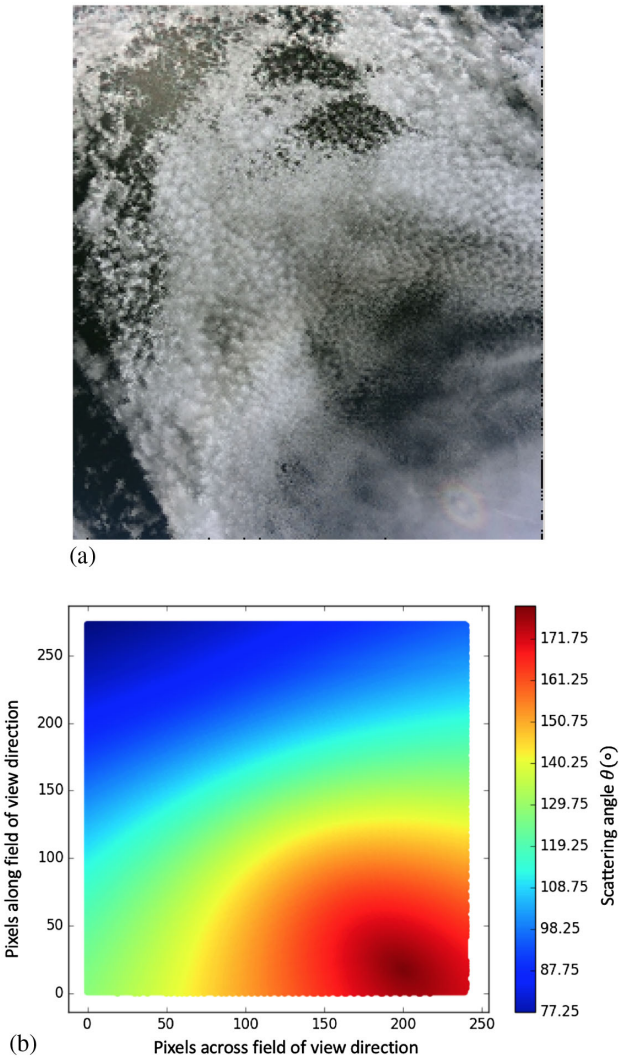

Fig. 2. (a) Glory on the bottom right observed over a field of liquid clouds by the spaceborne radiometer POLDER (May 10th, 2010, over the Eastern Pacific Ocean 13°S, 93°W offshore Chile). The image is around 1500 km × 2000 km. (b) Corresponding POLDER angles of observation (or scattering angles).

problems [12], is proposed. Indeed, as explained thereafter, the question of light interaction with a spherical scatterer is finally a 1D problem. The TMM algorithm is efficient and fast enough (in terms of computer time) to allow covering the whole electromagnetic spectrum usual in atmospheric optics (i.e., from ultraviolet up to infrared) as well as a complete droplet population. These results are then used to explicitly estimate the impact of TOR on satellite cloud liquid observations. Precisely, departures from Mie cross sections will be illustrated, and so the importance that TOR might have will be highlighted.

It is worth mentioning that tunneling resonances are not an unknown topic in physics, and some methods (sometimes cumbersome and hard to manage, e.g., [13]) exist to identify them. However, in this paper, (1) their probable importance is shown in atmospheric optics; (2) TORs are identified and characterized over the visible and infrared, i.e., the whole electromagnetic spectrum used in atmospheric optics; (3) their impact is explicitly quantified for both an isolated droplet and a realistic warm cloud droplet population; (4) application on

concrete POLDER (and 3MI) devices is made; (5) an efficient algorithm, easy and flexible, is proposed.

The plan is the following. Section 2 presents some important theoretical features relative to light interaction with a spherical scatterer: the wave equation, the quantum optical analogy (QOA), and the partial wave analysis (PWA) of scattering. These features are, herein, recalled because they are common topics in physics, but some of them deserve deeper explanations, since they are not frequently used (for not saying unused) in atmospheric optics. Especially, in Section 2, emphasis is placed on the QOA and the PWA, under which the present paper is based on. The methodology for the TOR characterization is explained in Section 3. The two next sections are an exposition of the results: Section 4 is relative to only one single droplet, and Section 5 deals with a droplet population. In this last section, the impact of TOR on POLDER and future 3MI measurements is assessed. Note that, for the present paper, it concerns only simulations. No attempt has been made to invert satellite measurements taking into account TORs. Conclusion and perspectives are the topics of Section 6.

2. THEORETICAL FEATURES

A. Light–Droplet Interaction

Light interaction with matter can be solved with Maxwell's equations that lead to the vectorial wave equations ($\boldsymbol{E}$ and $\boldsymbol{B}$ are the electric and magnetic fields, resp.):

$$\nabla^2\boldsymbol{E} - \underline{n}^2\frac{\partial^2\boldsymbol{E}}{\partial(ct)^2} = \boldsymbol{0}, \qquad \nabla^2\boldsymbol{B} - \underline{n}^2\frac{\partial^2\boldsymbol{B}}{\partial(ct)^2} = \boldsymbol{0}. \tag{5}$$

In these equations, t is time. Since these equations are linear, there is no loss of generality by assuming an exponential time dependence $\exp(-i\omega t)$ of the field (ω in rad s^{-1} is the angular frequency), so that $\partial^2\boldsymbol{E}/\partial(ct)^2 = -(\omega/c)^2\boldsymbol{E}$, and so to consider the Helmholtz equation $\nabla^2\boldsymbol{E} + \underline{n}^2k_0^2\boldsymbol{E} = \boldsymbol{0}$ (the same for $\boldsymbol{B}$). Such an equation is equivalent to

$$\nabla^2\Pi + \underline{n}^2k_0^2\Pi = 0, \tag{6}$$

where Π is the Debye potential, from which the electromagnetic field can be derived (e.g., [14,15]). Precisely, there are two independent components for Π, ${}^e\Pi$, and ${}^m\Pi$ (see [1] for details). We are thus dealing with two scalar wave equations (one for ${}^e\Pi$ and one for ${}^m\Pi$) instead of two vectorial wave equations (i.e., six components), which is of great advantage from a technical point of view. Vector $\boldsymbol{r}\Pi$ is the radial Hertz vector, $\boldsymbol{r}$ being the position vector whose origin is taken as arbitrary. For a spherical scatterer, it is naturally at the center of the sphere.

B. Wave Equation in Spherical Coordinates (r, θ, ϕ)

Since a droplet is a spherical scatterer, the solution of Eq. (6) can be expressed as $R(r)Y_\ell^{m_\ell}(\theta,\phi)$, i.e., the product of a radial function $R(r)$ by a spherical harmonic $Y_\ell^{m_\ell}(\theta,\phi)$:

$$Y_\ell^{m_\ell}(\theta,\phi) = (-1)^{m_\ell}\sqrt{\frac{2\ell+1}{4\pi}\frac{(\ell-m_\ell)!}{(\ell+m_\ell)!}}P_\ell^{m_\ell}(\cos\theta)\exp(im_\ell\phi), \tag{7}$$

where $P_\ell^{m_\ell}$ is an associate Legendre polynomial, and $m_\ell = -\ell, -(\ell-1), \ldots, 0, \ldots, \ell-1, \ell$.

The radial function is the solution of the following second-order differential equation:

$$\left[\frac{\mathrm{d}^2}{\mathrm{d}r^2} + \underline{n}^2k_0^2 - \frac{\ell(\ell+1)}{r^2}\right]U_R(r) = 0 \quad \text{with}$$

$$U_R(r) = r\,R(r). \tag{8}$$

C. Quantum-Optic Analogy

Strikingly, Eq. (8) is formally analogous to the 1D Schrödinger equation after introducing the effective potential energy $\mathcal{E}_{p,ef}$ and the energy $\mathcal{E} = \hbar c k_0$ of the incident wave [$\hbar = h/(2\pi)$ is the reduced Planck's constant], i.e.,

$$\left[\frac{\mathrm{d}^2}{\mathrm{d}r^2} - k_0^2\left(\frac{\underline{\mathcal{E}}_{p,ef}}{\mathcal{E}} - 1\right)\right]U_R(r) = 0, \tag{9}$$

with $\underline{\mathcal{E}}_{p,ef} = (1-\underline{n}^2)\mathcal{E} + \ell(\ell+1)\mathcal{E}/(k_0^2r^2)$. The expression of $\underline{\mathcal{E}}_{p,ef}$ is the sum of two terms: the r-independent constant term $(1-\underline{n}^2)\mathcal{E}$ and the centrifugal term $\ell(\ell+1)\mathcal{E}/(k_0^2r^2)$. Outside of a droplet, $\underline{n}$ is assumed to be 1. For more general problems, $\underline{n}$ can be assumed r-dependent (non-homogeneous droplet) or/and different from 1 outside of a droplet: for instance, the sharp transition at the droplet boundary can be replaced by a smooth transition modeling water vapor gradients around the droplet. Due to this formal identity, light–droplet interaction (radial part precisely) can be considered as the problem of a quantum object of energy $\mathcal{E}$ and wavefunction $U_R(r)$, under the field of potential energy $\underline{\mathcal{E}}_{p,ef}$. The specific point of this problem, compared to similar problems in quantum mechanics, is that $\underline{\mathcal{E}}_{p,ef}$ depends on the characteristics of the incident wave ($\mathcal{E}$ or k_0 and ℓ) and on the droplet (D, $\underline{n}$), $\underline{n}$ being dependent on $\mathcal{E}$ [16]. This is why light–droplet interaction can be considered as a morphology-dependent scattering problem. The potential energy $\underline{\mathcal{E}}_{p,ef}$ is sometimes called the "optical potential". As noted by [17], "the Schrödinger equation [i.e., Eq. (9)] for such a potential exactly reproduces the scattering of light by a medium of complex refractive index." Figure 3 is a sketch of $\mathcal{E}_{p,ef}$ ($\underline{n}$ has been taken as real) that clearly exhibits a potential well for which quasi-bound states that result from light tunneling can occur. Envisaged in this way, the existence of TORs is undoubtable. Their characteristics (strength, width) depend obviously on $\underline{\mathcal{E}}_{p,ef}$. Important characteristics of $\mathcal{E}_{p,ef}$ for given $\mathcal{E}$, ℓ, and D are ($\underline{n}$ is assumed to be a real number)

- well depth $\Delta = (n^2-1)\mathcal{E}$,
- barrier thickness $e = (\hbar c/\mathcal{E})[\ell(\ell+1)]^{1/2} - D/2$,
- energy interval $\mathcal{E}_H - \mathcal{E}_L$ for which TOR is expected, where

$$\mathcal{E}_H = \frac{2\hbar c}{D}[\ell(\ell+1)]^{1/2}, \qquad \mathcal{E}_L = \frac{\mathcal{E}_H}{n}. \tag{10}$$

The level $\mathcal{E}_H$ divides the energy interval into two regions: the below edge ($\mathcal{E} > \mathcal{E}_H$) and the above edge ($\mathcal{E} < \mathcal{E}_H$). In the ray optic approximation, the first (second) one corresponds to rays

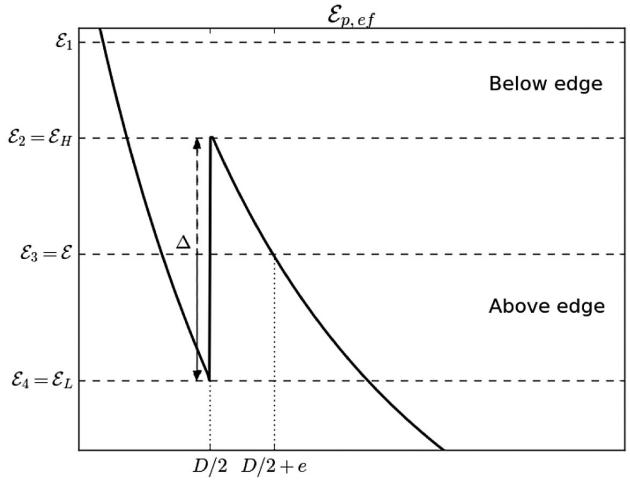

Fig. 3. Effective potential energy $\mathcal{E}_{p,ef}$ and its main characteristics. Clearly, light can penetrate inside a droplet (diameter D) by tunneling. The discontinuity of height Δ (well depth) at $D/2$ represents the droplet–air interface; the barrier thickness is e at incident light energy $\mathcal{E}=\mathcal{E}_3$.

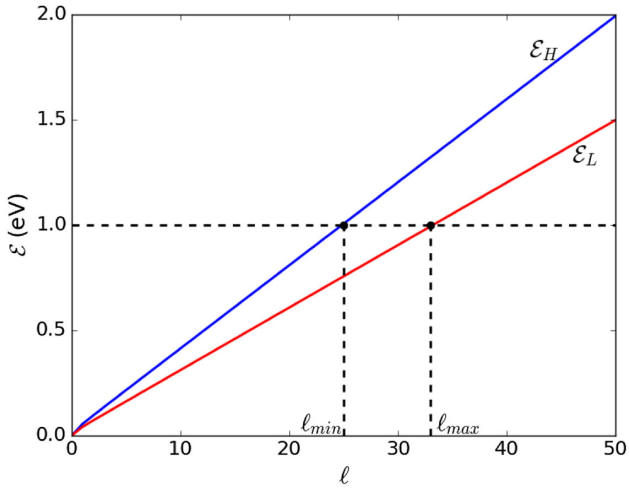

Fig. 4. Variation of top well and bottom well energies ($\mathcal{E}_H$ and $\mathcal{E}_L$, resp.) versus ℓ for $D=10$ μm and $n=1.33$.

of impact parameter lower (higher) than the droplet radius. So, in the above edge region, rays propagate away from the droplet and thus do not interact with it. Figure 4 displays $\mathcal{E}_H$ and $\mathcal{E}_L$ versus ℓ for $D=10$ μm and $n=1.33$. The area between the two curves indicates the space where TOR can be encountered. If $\ell<\ell_{\min}$, $\mathcal{E}>\mathcal{E}_H$: light can enter the droplet and give rise to some resonances that are not related to tunneling. If $\ell>\ell_{\max}$, $\mathcal{E}<\mathcal{E}_L$, and so there is no interaction with the considered droplet. For instance, with an incident wave energy $\mathcal{E}=1$ eV, TORs are expected in the interval $[\ell_{\min},\ell_{\max}]$, with $\ell_{\min}=25$ and $\ell_{\max}=33$. These values have been obtained by solving Eq. (10) for ℓ.

A generally accepted (but arbitrary) value of $\ell_{\max}$, i.e., the number of terms in the series $\sum_\ell$ [Eqs. (1) and (2)], is β or, sometimes better, $\beta+4\beta^{1/3}+2$, according to the droplet size [18]. Such empirical limits have been determined by analyzing the convergence of the series and for the specific goal of having fast algorithms for scattering computations. For the example above ($D=10$ μm, $\mathcal{E}=1$ eV), $\beta\approx 25$, and so, according to [18], $\ell_{\max}\approx 39$, which is comparable to the value given above (33). However, it is worth noting that the QOA gives a natural ceiling value for ℓ without any assumption about convergence or data fitting criteria.

D. Scattering and Partial Wave Analysis

Scattering by a central interaction, i.e., only r-dependent and of $O(r^{-1})$, as is the case here, can be efficiently addressed by means of the PWA. This technique is largely used in physics, e.g., to investigate particle collisions as nuclear scattering [19], and as we will show hereafter, it is also simple and efficient in the context of light–droplet interaction in atmospheric optics. In this paper, only the most important results of this method are presented—those useful for atmospheric optics—since many details can be found in standard physics textbooks (e.g., [17,20–24]).

At large distances from the scatterer, the (stationary) wavefunction can be written as

$$\underline{\psi}_{k_0}(r)\propto\exp(ik_0r\cos\theta)+\underline{f}_{k_0}(\theta)\frac{\exp(ik_0r)}{r},$$

where $\underline{f}_{k_0}$ is known as the scattering amplitude. The differential cross section of scattering is

$$\sigma_s(\theta)=|\underline{f}_{k_0}(\theta)|^2, \tag{11}$$

and the total cross section is given by the optical theorem

$$\sigma=\frac{4\pi}{k_0}\mathrm{Im}\{\underline{f}_{k_0}(0)\}, \tag{12}$$

where Im stands for the imaginary part. It can be useful to introduce partial quantities, i.e., relative to the wave order ℓ, such as the partial scattering amplitude $\underline{f}_{k_0,\ell}$ and the partial total cross section σ_ℓ, such that

$$\underline{f}_{k_0}(\theta)=\sum_\ell \underline{f}_{k_0,\ell}(\theta)\qquad \sigma=\sum_\ell\sigma_\ell. \tag{13}$$

The sum over ℓ in the expression of σ is due to the orthogonality of the partial scattering amplitudes. Note that $\sigma_s(\theta)$ is *not* the sum of the partial $\sigma_{s,\ell}(\theta)$, since interference effects must be taken into account:

$$\sigma_s(\theta)=\sum_\ell\left|\underline{f}_{k_0,\ell}\right|^2+2\sum_\ell\sum_{\ell'}\mathrm{Re}\left\{\underline{f}_{k_0,\ell}(\theta)\underline{f}^{\star}_{k_0,\ell'}(\theta)\right\}. \tag{14}$$

In the presence of inelastic processes (i.e., herein absorption), two kinds of partial scattering amplitude have to be considered [22,23] to describe the total scattering process: one, $\underline{f}^{(el)}_{k_0,\ell}$, for pure scattering (elastic contribution), and another, $\underline{f}^{(ab)}_{k_0,\ell}$, for the absorption (inelastic) contribution. For a TOR of energy $\mathcal{E}_r$, these two partial scattering amplitudes are, for an incident light energy $\mathcal{E}$, respectively,

$$\underline{f}^{(el)}_{k_0,\ell} = -\frac{2\ell+1}{k_0}\frac{\Gamma_{el}}{2(\mathcal{E}-\mathcal{E}_r)+i\Gamma}P_\ell(\cos\theta) \quad (15)$$

and

$$\underline{f}^{(ab)}_{k_0,\ell} = -\frac{2\ell+1}{k_0}\frac{(\Gamma_{el}\Gamma_a)^{1/2}}{2(\mathcal{E}-\mathcal{E}_r)+i\Gamma}P_\ell(\cos\theta). \quad (16)$$

In these expressions, Γ_{el} is the resonance width for the pure scattering component, Γ_a the resonance width due to absorption, and $\Gamma = \Gamma_a + \Gamma_{el}$.

The associated scattering and absorption partial cross sections follow directly by using Eq. (11):

$$\sigma_{s,\ell} = \frac{4\pi}{k_0^2}(2\ell+1)\frac{\Gamma_{el}^2}{4(\mathcal{E}-\mathcal{E}_r)^2+\Gamma^2}, \quad (17)$$

$$\sigma_{a,\ell} = \frac{4\pi}{k_0^2}(2\ell+1)\frac{\Gamma_{el}\Gamma_a}{4(\mathcal{E}-\mathcal{E}_r)^2+\Gamma^2}. \quad (18)$$

The total partial cross section is thus

$$\sigma_{e,\ell} = \sigma_{s,\ell} + \sigma_{a,\ell} = \frac{4\pi}{k_0^2}(2\ell+1)\frac{\Gamma_{el}\Gamma}{4(\mathcal{E}-\mathcal{E}_r)^2+\Gamma^2}, \quad (19)$$

which is again nothing more than the optical theorem $(4\pi/k_0)\mathrm{Im}\{\underline{f}^{(el)}_{k_0,\ell}(0)\}$.

3. METHODOLOGY FOR TOR CHARACTERIZATION

From what precedes, it is clear that the knowledge of ℓ and the TOR characteristics ($\mathcal{E}_r$, widths) lead to the optical quantities of importance. Hereafter, an efficient approach for the characterization of TOR is proposed.

A. Transfer Matrix Method

1. Definition of the Transfer Matrix (or *abcd* Matrix)

The transfer matrix approach is a general method used for a wide range of 1D linear problems in quantum mechanics, which consists in dividing the $\mathcal{E}_{p,ef}$ profile into a series of steps [12,25] [Fig. 5(a)]. Precisely, $\mathcal{E}_{p,ef}$ can be analyzed as being the combination of two elementary profiles: (1) stepped changes (upward or downward) between two adjacent bins of different potential energies; (2) region of uniform potential energy between two consecutive stepped changes. Each of these elementary profiles can be mathematically represented by an appropriate matrix that connects the complex amplitude of the wavefunction at the input (i) of the elementary potential energy to the complex amplitude of the wavefuntion at the output (o) of the elementary potential energy. For a stepped change (1), using the notations in Fig. 5(b),

$$\begin{bmatrix} \underline{k}_2^{1/2}\underline{\psi}^+ \\ \underline{k}_2^{1/2}\underline{\psi}^- \end{bmatrix}_o = [R]\begin{bmatrix} \underline{k}_1^{1/2}\underline{\psi}^+ \\ \underline{k}_1^{1/2}\underline{\psi}^- \end{bmatrix}_i, \quad (20)$$

with $[R] = \frac{1}{(2\underline{k}_1\underline{k}_2)^{1/2}}\begin{bmatrix} \underline{k}_1+\underline{k}_2 & \underline{k}_2-\underline{k}_1 \\ \underline{k}_2-\underline{k}_1 & \underline{k}_1+\underline{k}_2 \end{bmatrix}$.

For case (2), with the notations in Fig. 5(c),

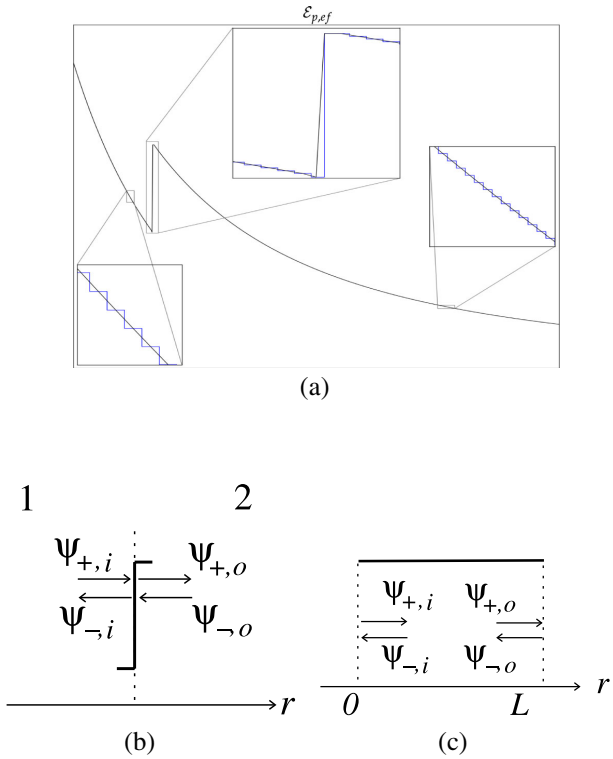

Fig. 5. (a) Decomposition of $\mathcal{E}_{p,ef}$ into a succession of steps at three different positions. (b) Elementary step and notations. Subscripts "i" and "o" stand for, respectively, input and output, i.e., just before the step (in the region numbered 1) and just after the step (in the region numbered 2). Wavenumbers in these regions are denoted $\underline{k}_1$ and $\underline{k}_2$. (c) Region of uniform potential energy over length L, separating two successive steps, and notations. This time, input and output ("i" and "o") mean precisely at the beginning and at the end of the uniform region, respectively. Wavenumber in this region is $\underline{k}$.

$$\begin{bmatrix} \underline{k}^{1/2}\underline{\psi}^+ \\ \underline{k}^{1/2}\underline{\psi}^- \end{bmatrix}_o = [T]\begin{bmatrix} \underline{k}^{1/2}\underline{\psi}^+ \\ \underline{k}^{1/2}\underline{\psi}^- \end{bmatrix}_i, \quad (21)$$

with

$$[T] = \begin{bmatrix} \exp(i\underline{k}L) & 0 \\ 0 & \exp(-i\underline{k}L) \end{bmatrix}.$$

By considering $\mathcal{E}_{p,ef}$ as a succession of stepped changes [Fig. 5(a)], one obtains, between the input and the output of the whole $\mathcal{E}_{p,ef}$, a matrix $[M]$ that is the product of the elementary matrices

$$[M] = \Pi_i[T]_i[R]_i = \begin{bmatrix} a & b \\ c & d \end{bmatrix}, \quad (22)$$

where a, b, c, and d are complex numbers. The matrix $[M]$ is also called, sometimes, the *abcd* matrix.

2. Confined State

For confined (or bound) states, the corresponding complex amplitude of the wavefunction must vanish far from the boundaries, and so a little algebra indicates that d must be zero. The matrix $[M]$ is therefore useful to identify TOR states that, to

remind, are quasi-bound states. For numerical computation, it is more convenient to search for the minimum value of $\ln|d|$, since (1) d is a complex number, and (2) a null value of d can never be reached rigorously (for any confined state, the value of d is very small compared with that of a non-confined state).

For details about the TMM and its condition of applicability, see [12].

3. Determination of the Wavefunctions

It follows directly, from the above definitions of the elementary matrices $[R]$ and $[T]$, that the complex amplitude of the wavefunction can be determined over the whole range of the coordinate r, viz., throughout the whole $\mathcal{E}_{p,ef}$ profile or, in other words, for a given pair $(\mathcal{E}, \ell)$, inside and outside the droplet considered. For that, only the wavefunction at whatever position r (the most natural one is far from the scatterer) must be given.

4. TOR Width Γ

Once a TOR is located, i.e., the couple $(\mathcal{E}_r, \ell_r)$ identified as described above, a complete characterization requires the determination of the resonance width Γ. For that, the incident energy $\mathcal{E}$ is decreased, starting from $\mathcal{E}_r$, by an arbitrary small quantity α, so that $\mathcal{E}_- = \mathcal{E}_r(1 - N\alpha)$, with N an integer, and, for each value of $\mathcal{E}_-$, $\ln|d|$ is computed. When half of the value of $\ln|d|$ at resonance is reached, the decrease is stopped ($N = N_-$). The same process is performed by increasing $\mathcal{E}$ from $\mathcal{E}_r$ and so by defining $\mathcal{E}_+ = \mathcal{E}_r(1 + N\alpha)$. The increase is thus stopped at $N = N_+$. Resonance width is thus $\Gamma = \mathcal{E}_+ - \mathcal{E}_- = (N_+ + N_-)\alpha\mathcal{E}_r$. The error in the determination of Γ is so $\Delta\Gamma = 2\alpha\mathcal{E}_r$. TORs have a very small width; a reasonable value of α is 10^{-6}: such a value permits to assess Γ with enough precision and low computing time (~ 1 min).

In order to simplify numerical computations, it is easier to consider, in the TMM, the real value of $\underline{n}$, and so to get $\mathcal{E}_r$ and Γ_{el}. Since the imaginary part of $\underline{n}$ always remains very small compared to the real part, one assumes that $\mathcal{E}_r$ is not substantially modified and that $\Gamma_a = 2\mathcal{E}_r \mathrm{Im}\{\underline{n}\}/\mathrm{Re}\{\underline{n}\}$ [13].

4. CASE OF A SINGLE DROPLET

A. TOR Characterization Algorithm

The algorithm to characterize TOR for only one droplet (diameter D) is the following: (1) considering a wavelength λ, incident light energy $\mathcal{E}$ and wavenumber k_0 are fixed using $\mathcal{E}(\mathrm{eV}) \approx 1.239/\lambda(\mu\mathrm{m})$ and $k_0 = \mathcal{E}/(\hbar c)$. Since the droplet diameter is in micrometers, it is convenient to have k_0 in $\mu\mathrm{m}^{-1}$, so we multiply the expression of k_0 by the elementary charge $e = 1.602176634 \times 10^{-19}$C and by 10^{-6}. (2) Knowing $\mathcal{E}$, an estimation of n is obtained from [16]. (3) Using Eq. (10), the interval $[\ell_{\min}, \ell_{\max}]$ is obtained and an $\ell-$ array is defined. (4) Potential energy $\mathcal{E}_{p,ef}$ is then defined for each value of ℓ in the previous interval and digitized (made of steps). (5) Matrix $[M]$ and so $\ln|d|$ are then computed versus ℓ. TORs are thus easy to identify searching for the local minima of $\ln|d|$. (6) The associated values of Γ_{el}, Γ_a, and Γ are determined as explained above.

B. Example

Figure 6 displays the variation of $\ln|d|$ versus ℓ for $D = 26.5$ μm and $\mathcal{E} = 1.0156$ eV ($n = 1.3237$). The dots correspond to integer values of ℓ. There are three minima of $\ln|d|$. TOR corresponds to those minima for which ℓ is an integer. From a numerical point of view, it is rare to have a minimum of $\ln|d|$ for an exact integer value of ℓ. We thus choose to identify a TOR under the two (in this order) next circumstances:

- the (real) value of ℓ for which $\ln|d|$ is minimum must not be greater than $\epsilon = 0.03$ from the closest integer value;
- the associated value of $\ln|d|$, namely, that corresponds to this closest integer value, must be close enough to the local minimum of $\ln|d|$. Precisely, in Fig. 7, the distance AB must be greater than $AC/2$.

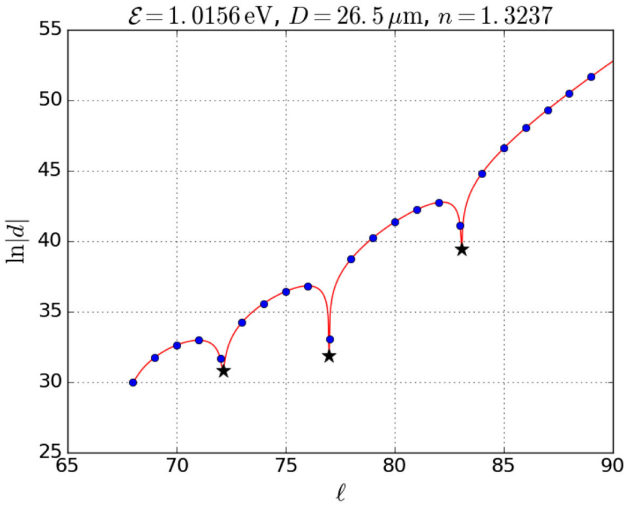

Fig. 6. Variation of $\ln|d|$ versus ℓ for a droplet of diameter $D = 26.5$ μm and an incident energy $\mathcal{E} = 1.0156$ eV. Blue dots are associated with integer values of ℓ. The three black stars indicate the three local minima.

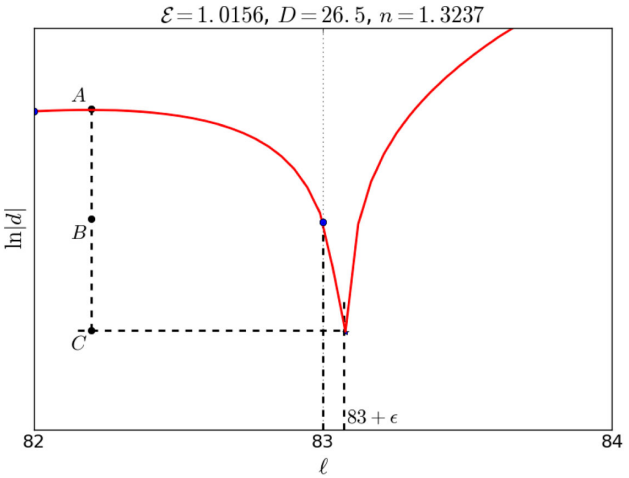

Fig. 7. Sketch for the criterion determination of a TOR using the example $\ell = 83$. The first criterion $\epsilon < 0.03$ is not satisfied.

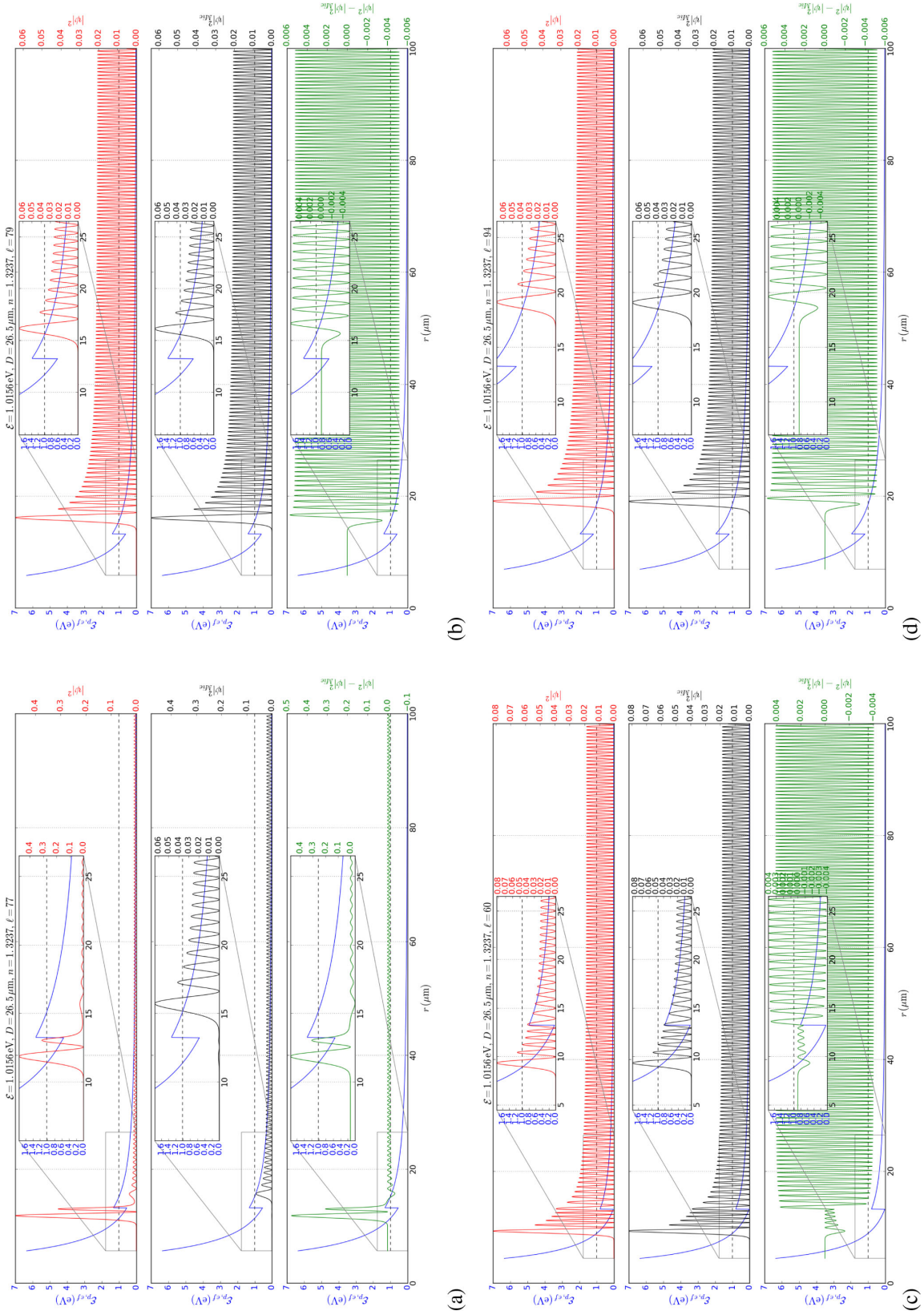

Fig. 8. Square modulus of the radial wavefunction showing light energy density (normalized, arbitrary unit) for (a) $\ell = 77$ (TOR occurrence), (b) $\ell = 79$ (no TOR occurrence), (c) $\ell = 60$ (optical resonance with no tunneling origin), and (d) $\ell = 94$ (no interaction). For each subfigure, the blue curve represents the optical potential energy $\mathcal{E}_{p,ef}$. The red and black curves are the light density given by the TMM ($|\underline{\psi}|^2$) and by Mie's theory ($|\underline{\psi}|^2_{\mathrm{Mie}}$), respectively; the green curve shows the difference ($|\underline{\psi}|^2 - |\underline{\psi}|^2_{\mathrm{Mie}}$). Ordinate axes are colored according the curves. The horizontal dashed lines indicate the value of the incident light energy.

Using these two assumptions, only the minimum at $\ell = 77$ is considered as a TOR. The minimum, located at $\ell = 83$ (Figs. 6 and 7) does not satisfy the first criterion, and the same for the minimum located at $\ell = 72$ (not shown).

From the $abcd$ matrix, the square modulus of the wavefunction, which is related to light energy density, can be determined and compared with Mie's theory predictions. This comparison is displayed in Fig. 8 with the associated optical potential $\mathcal{E}_{p,ef}$.

The tunneling resonance identified at $\ell = 77$ appears clearly by a significant and sharp peak of light density that indicates a susbtantial amount of light inside the droplet, contrary to the Mie's theory prediction according to which the amount of light inside the droplet is very weak [Fig. 8(a)]. The resonance widths obtained are $\Gamma_{el} = 3.96 \times 10^{-4}$ eV, $\Gamma_a = 3.48 \times 10^{-5}$ eV, and so $\Gamma = 4.31 \times 10^{-4}$ eV. The low value of Γ_a is due to the low value of $\mathrm{Im}\{\underline{n}\} = 2.27 \times 10^{-5}$ (viz., low absorption). In addition, the low value of Γ_{el} indicates that the TOR is very sharp.

For another value of ℓ that does not give rise to tunneling, e.g., $\ell = 79$ [Fig. 8(b)], light does not penetrate inside the droplet, and light density as given by the TMM (red curve) agrees very well with that predicted by Mie's theory (black curve). Figures 8(c) and 8(d) present, respectively, as an example, the case $\mathcal{E} > \mathcal{E}_H$ ($\ell = 60$), which corresponds to optical resonance *without* tunneling origin, and the case $\mathcal{E} < \mathcal{E}_L$ ($\ell = 94$) for which light does not even interact with the droplet. In both these cases, TMM and Mie's theory are in very good agreement.

Light densities in the two-dimensional (2D) Cartesian plane (not shown) are obtained by considering the associated spherical harmonics Y_{60}, Y_{77}, Y_{79}, and Y_{94}. Obviously, they do not impact the radial dependence: light density is still the highest inside the droplet in the case of a TOR and in perfect agreement with Mie's theory for the three other cases.

C. TOR Occurrences

Similar results have been obtained for other values of D and $\mathcal{E}$. As a summary, Fig. 9 provides a synthetic representation that indicates the TOR occurrences (values of ℓ, colorbar) for various values of D, from 5 μm to 30 μm, and of the incident energy $\mathcal{E}$, from 0.4 eV ($\lambda = 3$ μm) to 3.1 eV ($\lambda = 400$ nm) (i.e., from the near IR to the UV/blue limit).

For a given droplet (D is fixed), the lowest values of ℓ are associated with the lowest values of the incident energy $\mathcal{E}$. Conversely, for a fixed value of ℓ, the lower the energy, the higher the diameter. These results agree perfectly with the tunneling interpretation and with Eq. (10).

In the same way, Fig. 10 gives the values of the resonance widths Γ for the energy $\mathcal{E}$ and diameter D ranges indicated above. It appears clearly that resonance widths are small, ranging from values lower than 0.001 eV up to values 10 times higher. It means that $\mathcal{E}_r / \Gamma \sim 10^2$ or 10^3. Roughly, the higher the D and/or $\mathcal{E}$, the sharper the resonance. In other words, the highest values of Γ (viz., the less sharp the resonance) concern energies lower than 1 eV, i.e., the IR region of the electromagnetic spectrum.

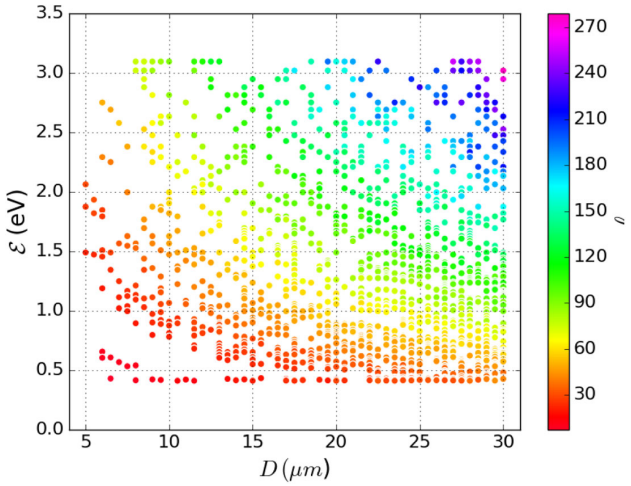

Fig. 9. TOR occurrences according to the triplet ($\mathcal{E}$, D, ℓ).

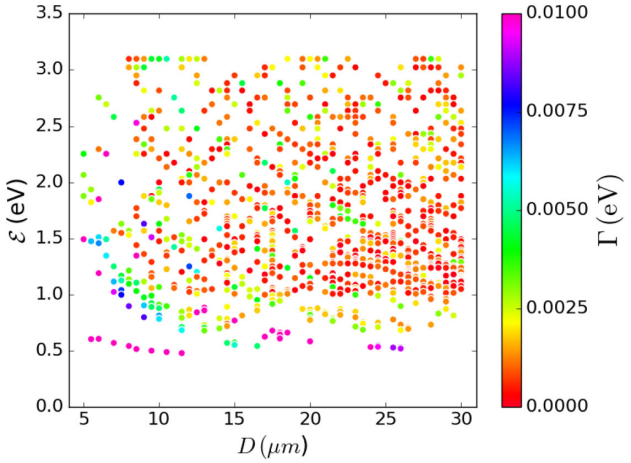

Fig. 10. Resonance width Γ versus ($\mathcal{E}$, D).

D. Cross-Section Ratios

Since TORs have been identified with their corresponding widths, the three cross sections can be computed using Eqs. (17)–(19) and compared with those given by Mie's theory [Eqs. (1)–(3)]. Precisely, for each diameter D and energy $\mathcal{E}$, the cross section $\sigma_\alpha(D, \mathcal{E}) = \sum_\ell^{\ell_{\max}} \sigma_{\alpha,\ell}(D, \mathcal{E})$—where α stands for "s" (scattering), "e" (extinction), and "a" (absorption)—is computed and compared to the corresponding Mie's theory cross sections [Eqs. (1)–(3)]. In the last finite series, the $\sigma_{\alpha,\ell}$ are computed using Eqs. (17)–(19) for each value of ℓ, which corresponds to a TOR and using Eqs. (1)–(3) otherwise. We obtain thus two quantities: σ_α if TORs are taken into account, and $\sigma_\alpha^{\mathrm{Mie}}$ otherwise. Comparisons are made by considering the ratio $r_\alpha = (\sigma_\alpha - \sigma_\alpha^{\mathrm{Mie}})/\sigma_\alpha^{\mathrm{Mie}}$. In the sequel, these ratios will be given in percent (%): the ratios r_α are always greater than 1 so, for example, $r_\alpha = 10\%$ means that σ_α is 10% higher than $\sigma_\alpha^{\mathrm{Mie}}$, i.e., $\sigma_\alpha = 1.10\sigma_\alpha^{\mathrm{Mie}}$.

Figure 11 displays the ratio r_s, r_e, r_a. It appears that scattering and extinction cross sections are a few percent (up to 15%) higher than those predicted by Mie's theory (i.e., r_e and r_s can reach 1.15): at low energy ($\mathcal{E} < 1.5$ eV) and for small

droplets ($D < 15$ μm), r_s and r_e are of the order of 12%. For larger diameters, r_s and r_e are between 5% and 8%. These two ratios are small (lower than 2%) for the largest diameters and the highest energies (i.e., in the blue/UV region of the electromagnetic spectrum). The case of absorption is also interesting, since σ_a can be two times higher than the Mie absorption cross section. This is not surprising since light energy density can be very important inside a droplet in the case of TOR. Figure 12 displays the probability density functions (pdf) of r_s, r_e, and r_a and shows how dispersed are the values of these ratios in the (simulated) sample considered herein. One can see that the dominant ratios are about 5% for scattering and extinction. For absorption, the ratio is mainly between 0% and 100%; a ratio higher than 100% can be obtained but rarely.

5. APPLICATION TO POLDER/3MI OBSERVATIONS

In the case of POLDER, or other similar satellites (as the future 3MI) and also airborne or ground-based cloud observations, light scattering does not concern only a single droplet but instead a population of thousands of droplets with various diameters and optical indices. In order to quantify the impact of TOR occurrences in such a context, the cross sections when TORs are taken into account are compared to those when TORs are not considered (i.e., Mie's theory).

A. Droplet Population

Different droplet size distributions (DSDs) can be chosen to characterize a droplet population. A realistic DSD, typical of warm clouds, is the gamma-modified distribution [26]

$$N_d(D) = 10^{-4} A (D/2)^2 \exp(-B D/2), \qquad \textbf{(23)}$$

where A and B are two constants. The quantity $N_d(D)$ represents the number (per unit volume) of droplets of diameter between D and $D + \mathrm{d}D$. The two constants are, if ρ_w denotes the liquid water density (taken at 1 g cm^{-3}), $A = 2.27 \times 10^{-8} W_l/(\rho_w \bar{D}^6)$ and $B = 6/\bar{D}$, W_l (g cm^{-3}) being the mass liquid water content and $\bar{D} = 2.14 \times 10^{-7} W_l/(\rho_w N_t)^{1/3}$ the mean diameter of the DSD; N_t (cm^{-3}) is the total number of droplets. Thus, given N_t and W_l, which are readily measurable physical quantities, and the range of droplet diameters D, the DSD is completely determined. The maximum diameter is chosen at 30 μm. Figure 13 displays an example of such a DSD [Eq. (23)].

For the next calculations, it has been assumed that (1) each droplet is a homogeneous dielectric sphere; (2) each droplet is optically independent of each other (clouds are disorganized media); (3) droplets present the same optical index (same temperature, same pressure, and no aerosols are dissolved or included in the droplets); (4) droplets are centered at the same point. This assumption is only for convenience in the management of the calculations. It is not a severe assumption since, at remote distances of observation, the exact position of each droplet inside the resolution volume is not of crucial importance. In Section 6, we will indicate how assumptions (1), (2), and (3) can be relaxed to some extent.

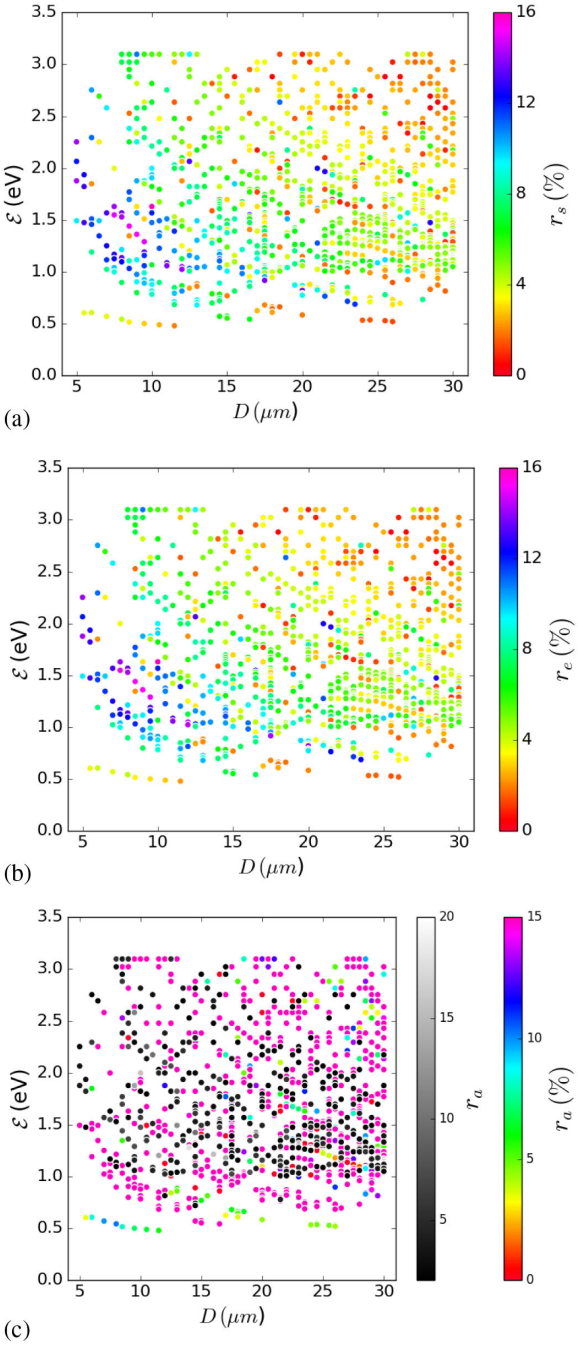

Fig. 11. (a) Scattering, (b) extinction, and (c) absorption cross-section ratio r_α (α) versus ($\mathcal{E}$, D). See text for details. In (c), the gray colorbar refers to ratio greater than 2, while the colored one is for ratio (in %) between 1 (0%) and 2 (100%).

B. Cross-Section Comparisons

Since droplets are optically independent of each other, the cross section of the droplet population, at a given incident light energy $\mathcal{E}$, is the *sum* of each individual (droplet) cross section. The hereafter considered energies $\mathcal{E}$ are those of the nine POLDER channels (Fig. 14). These channels present a width (full width at half-maximum) between 10 nm and 40 nm around, viz., a width in terms of energy on the order of 0.1 eV approximately. Since TOR width Γ is around 10^{-3} eV, each

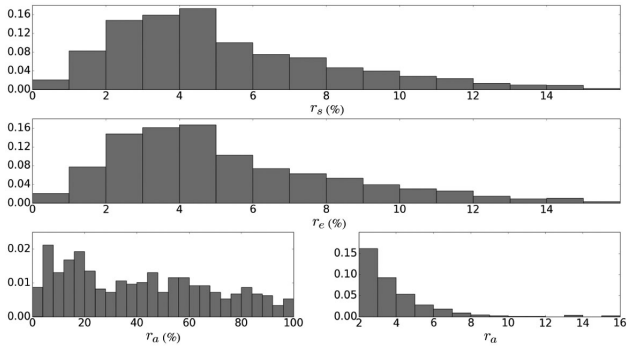

Fig. 12. Probability density functions of the cross-section ratios r_α (α): "s," scattering; "e," extinction; and "a," absorption.

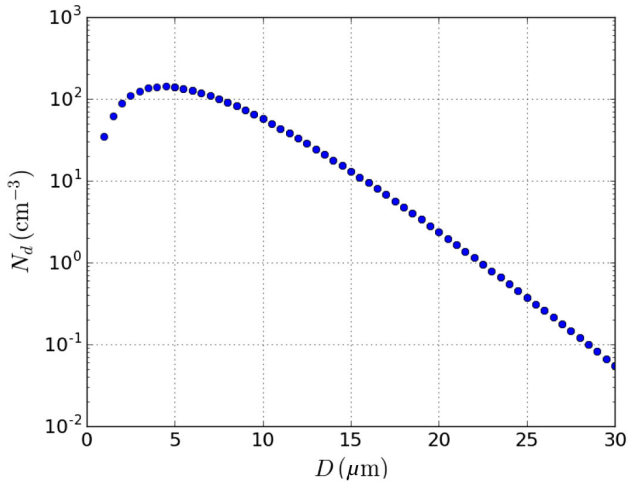

Fig. 13. Warm cloud droplet size distribution [Eq. (23)] with $N_t = 574$ cm^{-3} and $W_l = 0.2$ g cm^{-3}. This DSD has been chosen as a droplet population to illustrate the impact of TOR for remote sensing.

POLDER channel is expected to be full of TOR. For each POLDER channel, the procedure for cross-section computations is the following: (1) a POLDER channel is initially chosen and, for each energy $\mathcal{E}$ in this channel, TORs are searched for the entire droplet population. To do that, each diameter in the DSD is considered separately; for a given D, the values of ℓ that give rise to a TOR are determined using the methodology defined in Section 3. Let us denote these values, for instance, ℓ_1, ℓ_2 (two TOR occurrences). Resonance widths are also obtained. (2) Cross sections are then computed for the population according to

$$\sigma_\alpha(\mathcal{E}) = \sum_i N_d(D_i) \sum_{\ell=0}^{\ell_{\max}} \sigma_{\alpha,\ell}(D_i, \mathcal{E}), \tag{24}$$

where α stands for "s" (scattering), "a" (absorption), and "e" (extinction). The serie $\sum_\ell \sigma_{\alpha,\ell}$ has to distinguish the values of ℓ that give rise to a TOR from those that do not. For the former, Eqs. (17)–(19) are used, while for the latter, Eqs. (1)–(3) are obviously used. It follows that, if there are, for instance, two TOR occurrences at ℓ_1 and $\ell_2 > \ell_1$, $(D_i, \mathcal{E})$ being fixed,

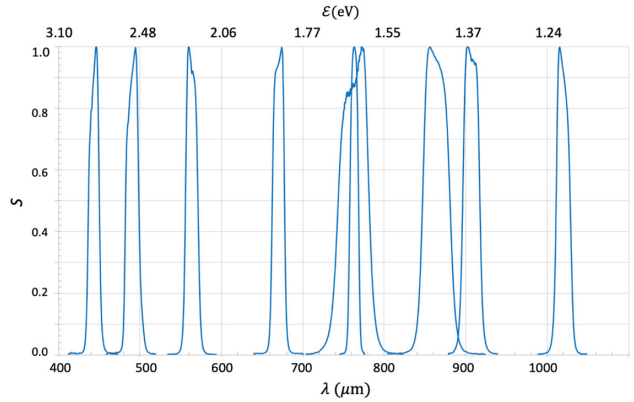

Fig. 14. POLDER spectral channels (S is the spectral response) with the wavelength (λ)–energy ($\mathcal{E}$) correspondence.

$$\sum_{\ell=0}^{\ell_{\max}} \sigma_{\alpha,\ell} = \sum_{\ell=0}^{\ell_1-1} \sigma_{\alpha,\ell}^{(\mathrm{Mie})} + \sigma_{\alpha,\ell_1} + \sum_{\ell_1+1}^{\ell_2-1} \sigma_{\alpha,\ell}^{(\mathrm{Mie})} + \sigma_{\alpha,\ell_2} + \sum_{\ell_2+1}^{\ell_{\max}} \sigma_{\alpha,\ell}^{(\mathrm{Mie})}. \tag{25}$$

(3) The cross section for the considered population is then multiplied by the spectral response $S(\mathcal{E})$ of the POLDER detector in order to weight the contribution of $\sigma_\alpha(\mathcal{E})$ in the POLDER channel. So,

$$\sigma_\alpha = \sum_j \left[S(\mathcal{E}_j) \sum_i N_d(D_i) \sum_{\ell=0}^{\ell_{\max}} \sigma_{\alpha,\ell}(D_i, \mathcal{E}_j) \right]. \tag{26}$$

(4) Points (1), (2), and (3) are repeated *without* taking into account any TOR, and so using only Mie's theory. That gives

$$\sigma_\alpha^{(\mathrm{Mie})} = \sum_j \left[S(\mathcal{E}_j) \sum_i N_d(D_i) \sum_{\ell=0}^{\ell_{\max}} \sigma_{\alpha,\ell}^{(\mathrm{Mie})}(D_i, \mathcal{E}_j) \right]. \tag{27}$$

The ratio $r_\alpha = \sigma_\alpha / \sigma_\alpha^{(\mathrm{Mie})}$ quantifies the impact of TOR occurrences. Since the COT is directly proportional to the total cross section, one deduces $\mathrm{COT}/\mathrm{COT}_{\mathrm{Mie}} = r_e$. In addition, the SSA is such that $\mathrm{SSA}/\mathrm{SSA}_{\mathrm{Mie}} = r_s / r_e$.

Table 1 summarizes the ratios obtained for each POLDER channel.

It appears clearly that absorption is much more important when considering TOR, since values of r_a range from 3.5% to 27.1%. Such percentages are easily understandable, since tunneling resonances lead to substantial increases of light energy inside the droplet compared to Mie's theory predictions (see Fig. 8). These values are consistent with those obtained in [7,9]. Such an important increase in the absorption cross section leads one to think that TOR may contribute to the anomalistic absorption, i.e., the positive difference between the measured cloud solar absorption and its theoretical estimate [27–29]. As suggested by [28], such an anomaly indicates a poor understanding of the interaction between sunlight and cloud. More recently, [9] has concluded that TOR effects are important for narrow spectral regions ($\Delta\lambda \sim 10$ nm) but

Table 1. Ratios r_s, r_a, and r_s Obtained for Each POLDER Channel[a]

Channel Number	1 (P)	2	3	4	5	6	7	8 (P)	9 (P)
Wavelength interval (nm)	412–473	535–594	879–939	989–1049	705–824	745–776	459–520	640–701	804–924
Energy interval (eV)	2.62–3.01	2.09–2.32	1.32–1.41	1.18–1.25	1.51–1.76	1.60–1.66	2.39–2.70	1.77–1.94	1.34–1.54
r_s (%)	0.942	0.980	1.007	0.923	1.030	1.048	0.932	1.00	1.070
r_a (%)	13.6	21.1	26.5	25.5	26.9	27.1	18.8	3.5	26.1
r_e (%)	0.942	0.980	1.010	0.935	1.031	1.049	0.932	1.00	1.072

[a] See text for details. The letter "P" indicates that the channel is polarized.

negligible for broadband cloud absorption. Moreover, based on comparisons between an atmospheric general circulation model and observational data, [30] has dismissed the effect of clouds on atmospheric absorption and suggested that water vapor is the dominant influence, at the planetary scale. It is not the place herein to debate about the anomalistic absorption, since this topic requires further examination and radiative transfer calculations. The ratio of scattering $r_s \sim 1\%$ is not so high because light density far from the droplet presents a small, but not negligible, difference between TOR and Mie's theory. The ratio of extinction r_e is of the same order of r_s because the Mie absorption cross section is relatively low in the spectral domain considered. Indeed, since $\sigma_e = \sigma_s + \sigma_a$, one has

$$r_e\sigma_e^{(\mathrm{Mie})} = r_s\sigma_s^{(\mathrm{Mie})} + r_a\sigma_a^{(\mathrm{Mie})},$$

$$r_e = r_s\frac{\sigma_s^{(\mathrm{Mie})}}{\sigma_s^{(\mathrm{Mie})}+\sigma_a^{(\mathrm{Mie})}} + r_a\frac{\sigma_a^{(\mathrm{Mie})}}{\sigma_s^{(\mathrm{Mie})}+\sigma_a^{(\mathrm{Mie})}}$$

$$\approx r_s, \tag{28}$$

since $\sigma_a^{(\mathrm{Mie})} < \sigma_s^{(\mathrm{Mie})}$. As a final remark, note that no general tendency emerges from these values: for a given droplet population, the behaviors of the ratios versus the energy are very difficult to predict since they depend on the TOR strength at a given energy and on the spectral response of the receiver channel at the location of the TOR. Some TOR can be very strong but with a small contribution to the spectral band because the spectral response for this TOR is very low, and vice versa. Similar orders of magnitudes have been obtained with other DSDs. These values concern also the new spaceborne instrument 3MI, since it has the same spectral bands of observation as POLDER. Only POLDER channels 2 and 4 are not included in 3MI. This last instrument will be able to observe in the following extra spectral bands (central wavelengths): 410 nm (3.022 eV), 555 nm (2.232 eV), 754 nm (1.643 eV), 1370 nm (0.904 eV), 1650 nm (0.750 eV), and 2130 nm (0.582 eV). As for POLDER, the bandwidths (full width at half-maximum) of these bands range from 10 nm to 40 nm. Note that TOR widths are typically $\Gamma \sim 10^{-2}$ eV at most, i.e., $\Delta\lambda_0 \sim 2$ nm if $\lambda_0 = 500$ nm and $\Delta\lambda_0 \sim 8$ nm at $\lambda_0 = 1$ μm. As indicated by [9], neglecting sharp resonances for such bands (or narrower) could cause substantial biases in remote sensing retrievals. Detailed data of sensitivity were not available at the time of writing this paper to calculate explicitly, as above for POLDER, the different ratios r_e, r_s, and r_a. However, similar orders of magnitude of the ratios, or a little bit higher, can reasonably be expected, since (1) the 3MI spectral band main characteristics are not substantially different from those of POLDER and (2), as seen above (e.g., Fig. 9), TOR proliferates for such spectral intervals in these bands. Solar radiation is a natural light and the ratios r_s, r_a, and r_e take into account the case of a polarized channel (POLDER channels 1, 8, and 9). Indeed, polarization is selected at the receiver filters, so that the cross sections ($\sigma_\alpha^{(\mathrm{Mie})}$ and σ_α, with $\alpha = s, a, e$) are modified in the exact same way (i.e., multiplying them by the squared cosine of the polarizing filter angle). The specific topics of polarization in the presence of TORs for non-spherical scatterers and for multiple scattering will be addressed in another study.

C. Ratio of the Angular Distribution of the Scattered Intensity

Figure 15 displays the ratio $r_d = I_{\mathrm{TOR}}(\theta)/I_{\mathrm{Mie}}(\theta)$ of the scattered light intensity versus scattering angle θ for the above considered droplet population and for each POLDER channel. Since the scattered intensity is directly proportional to the differential scattering cross section, r_d is also the ratio of the scattering cross sections when (and without) taking into account the TORs. The intensities $I_{\mathrm{TOR}}(\theta)$ and $I_{\mathrm{Mie}}(\theta)$ are easily calculated, for each diameter D and incident energy $\mathcal{E}$, using the scattering amplitudes given by the PWA (see above) and by Mie's theory (see [1]), respectively. Similar to the previous subsection, the cross sections of each droplet are weighted by the population $N_d(D)$ and the spectral response $S(\mathcal{E})$ of the POLDER channel. The ratio is higher than 1, especially at large scattering angles, and increases (not monotonically)

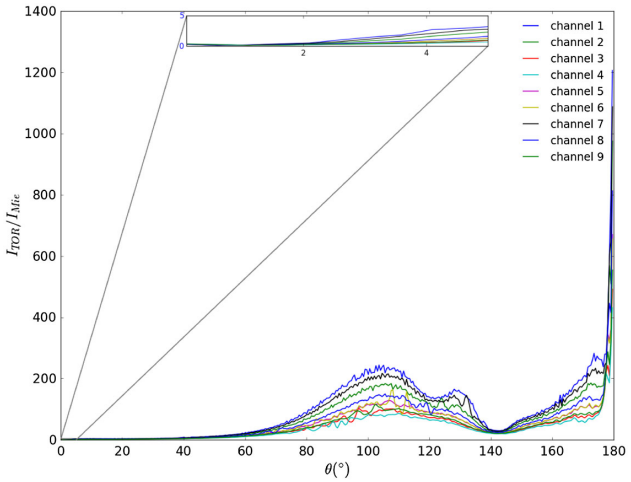

Fig. 15. Ratio of the scattered intensity $I_{\mathrm{TOR}}(\theta)/I_{\mathrm{Mie}}(\theta)$ (or ratio of the differential cross section) versus scattering angle θ, with and without (Mie's theory) taking into account TOR, for the droplet population in Fig. 13 and each POLDER channel.

with θ. At very low scattering angles, $r_d \approx 1$ (the corona is thus well described by Mie's theory), while $r_d \gg 1$ for $\theta > 170°$. This is in agreement with the [3]'s assumption that the glory, which is mainly a backscattering effect, has a tunneling origin. Obviously, the behavior of r_d depends on the angular behavior of the Mie scattering diagram. For scattering angles far from forward scattering, $I_{\mathrm{Mie}}(\theta)$ is, as well known, relatively low, especially for $\theta > 80°$, so that it is not surprising to obtain high values of r_d. Note, however, the minimum observed at $\theta \approx 140°$, which corresponds to the rainbow—the minimum angle of deviation is 138° for the primary bow given by a drop of refractive index of about 1.33; at this angle, I_{Mie} presents a peak (a caustic), which is relatively close to I_{TOR}.

This work has been achieved with a typical laptop (with i7 processor, RAM 16 Gb). Computation times are the following. For a given value of light energy and one droplet, the TOR characterization takes around 10 s. With a droplet population of 20 to 60 droplets, computation time is between 5 and 10 min. If now one considers a POLDER channel with around 100 values of light energy, total computation time is about half a day to one day. Once TOR is characterized, the cross sections are obviously very fast to compute.

6. CONCLUSION AND PERSPECTIVES

In this paper, another approach to light–matter interactions (for spherical symmetry) in atmospheric optics, viz., the QOA and PWA, has been used in order to take into account TORs, i.e., extremely sharp resonances. As underlined by [17], the QOA allows an exact reproduction of the light scattering by any medium of complex optical index. In order to characterize these resonances, which according to some relatively recent results explain completely the atmospheric glory, a flexible and fast algorithm, the TMM, accompanied by some reasonable assumptions for better numerical characterization, has been developed. The energetic location $\mathcal{E}_r$ and width Γ of any TOR have been identified for a large interval of droplet diameters (from 5 μm to 30 μm) over the whole electromagnetic spectrum of atmospheric interest (i.e., from the blue-limit of the visible to the near infrared). There are a lot of TORs in this spectrum, and their sharpness (small width, $\mathcal{E}_r/\Gamma \sim 10^2, 10^3$) explains why they are misrepresented in the common practices of atmospheric optics. However, we have shown that the importance of TOR should not be neglected. The associated cross sections of TOR have been calculated: they present a substantial enhancement with respect to Mie's theory predictions. This paper is not limited to isolated droplets, but results are also given for a whole cloud droplet diameter distribution and for the POLDER's and future 3MI channels. In this sense, this paper completes previous results based only on some specific examples (one droplet). An original point of this paper is the explicit calculations of TOR contributions that were made by taking advantage of the rapidity of the TMM.

The results suggest that TORs impact the different cross sections of a droplet and of a droplet population in the visible and the infrared. The increase of the absorption cross section of a cloud droplet population can reach almost 30% of Mie's theory predictions. This is explained by the strong enhancement of the light energy inside a droplet. Scattering and extinction cross sections are also higher than those of Mie's theory, but to a lesser extent. The results suggest moreover that higher spectrally resolved instruments, at a judiciously chosen spectral band, would be welcome for a complete profiling of TOR. Also, an appropriate inversion method, e.g., the Gelfan–Levitan–Marchenko equation, would be necessary to retrieve the optical potential from the scattering data. These two points are under investigation. However, for the time being, and from a practical point of view, the ratios introduced in this paper can be used as look-up tables in order to correct Mie's theory cross sections. Furthermore, future investigations will be devoted to quantify the impact of TOR on radiative transfer algorithms, in particular, stochastic ones (including 3D effects/multiple scattering): how are the results of such algorithms modified when TORs are explicitly taken into account? As concluded by [9] by means of a high-resolution radiative transfer model (with multiple scattering), we expect that TOR could be important. Answering this kind of question as thoroughly as possible deserves a specific paper.

While it has been applied to spherical homogeneous droplets, this approach can also be relevant for aerosols, or other complex-shaped scatterers, provided that they are assumed spherical. The above conclusions concern also, for instance, lidar aerosol measurements. Obviously, such an assumption is more restrictive when deviations from the spherical geometry are important. In addition, this approach is also convenient for heterogeneous scatterers of spherical symmetry, as, for instance, (1) a spherical wet aerosol, i.e., covered by a thin film of water, (2) a multilayered scatterer, i.e., made of several concentric spherical layers of different optical indices, and (3) scatterers with r-dependent optical index $\underline{n}(r)$. For cases (1) and (2), the $\mathcal{E}$-normalized effective potential energy is

$$\frac{\mathcal{E}_{p,ef}}{\mathcal{E}} = \begin{cases} 1 - n_i^2 + \dfrac{\ell(\ell+1)}{k_0 r^2} & r_{i-1} < r < r_i \\ \dfrac{\ell(\ell+1)}{k_0 r^2} & r > r_N \end{cases}, \tag{29}$$

with $i = 1, \ldots, N$, with N the number of layers [$N = 2$ for case (1)]. For case (3), n_i is substituted by $n(r)$. The case of aerosol-polluted droplets (e.g., by soot) is important: it has been mentioned by [9] but not addressed, though it is expected to significantly increase absorption, especially for broadband.

Optical index gradients at the scatterer edge, viz., between the scatterer and surroundings, can also be addressed. For example, in the realistic case of a droplet surrounded by a thin layer of water vapor, with a gradient of absolute humidity, the effective potential energy should vary continuously from inside the droplet to its outside.

Tunneling resonances (position, width) are impacted by all of these effects. This will be examined in a future paper.

Funding. PNTS-2016-11, CNES & Région Haut-de-France, Labex CaPPa (ANR-11-LABX-0005-01).

Acknowledgment. We would like to thank Fabrice Ducos (computing engineer at the Laboratoire d'optique atmosphérique, LOA), who performed the algorithm for the extraction of the POLDER image in Fig. 2. Thanks also

to Dr. Qiaoyun Hu (LOA) for some programming contributions. This work is part of the PhD thesis of R. Yaacoub. We are grateful to the Région Haut-de-France and to the CNES (Centre national d'études spatiales), which have equally funded this PhD. We thank also the Labex CaPPA (ANR-11-LABX-0005-01) and the CPER CLIMIBIO for their support in this work. This work has also been supported by the Programme National de Télédétection Spatiale (PNTS, http://programmes.insu.cnrs.fr/pnts/), grant no PNTS-2016-11.

REFERENCES

1. M. Born and E. Wolf, *Principles of Optics* (Pergamon, 1964).
2. G. Mie, "Beiträge zur Optik trüber Medien, speziell kolloidaler Metallösungen," Ann. Phys. **330**, 377–445 (1908).
3. H. M. Nussenzveig, "Does the glory have a simple explanation?" Opt. Lett. **27**, 1379–1381 (2002).
4. J. Spinhirne and T. Nakajima, "Glory of clouds in the near infrared," Appl. Opt. **33**, 4652–4662 (1994).
5. http://www.icare.univ-lille1.fr/parasol/overview.
6. P.-Y. Deschamps, F.-M. Bréon, M. Leroy, A. Podaire, A. Bricaud, J.-C. Buriez, and G. Sèze, "The POLDER mission: instrument characteristics and scientific objectives," IEEE Trans. Geosci. Remote Sens. **32**, 598–615 (1994).
7. H. M. Nussenzveig, "Light tunneling in clouds," Appl. Opt. **42**, 1588–1593 (2003).
8. D. L. Mitchell, "Parameterization of the Mie extinction and absorption coefficients for water clouds," J. Atmos. Sci. **57**, 1311–1326 (2000).
9. C. Zender and J. Talamantes, "Solar absorption by Mie resonances in cloud droplets," J. Quant. Spectrosc. Radiat. Transfer **98**, 122–129 (2006).
10. https://www.eumetsat.int/website/home/Satellites/FutureSatellites/EUMETSATPolarSystemSecondGeneration/3MI/index.html.
11. F.-M. Bréon and P. Goloub, "Cloud droplet effective radius from spaceborne polarization measurements," Geophys. Res. Lett. **25**, 1879–1882 (1998).
12. O. Pujol, R. Carles, and J. P. Pérez, "Quantum propagation and confinement in 1D systems using the transfer-matrix method," Eur. J. Phys. **35**, 035025 (2014).
13. L. Guimaraes and H. Nussenzveig, "Uniform approximation to Mie resonances," J. Mod. Opt. **41**, 625–647 (1994).
14. J. A. Stratton, *Electromagnetic Theory*, 1st ed. (McGraw-Hill, 1941).
15. J. D. Jackson, *Classical Electrodynamics* (Wiley, 1975).
16. G. Hale and M. Querry, "Optical constants of water in the 200 nm to 200 μm wavelength region," Appl. Opt. **12**, 555–563 (1973).
17. J. Taylor, *Scattering Theory: The Quantum Theory on Nonrelativistic Collisions* (Wiley, 1972).
18. W. Wiscombe, "Improved Mie scattering algorithms," Appl. Opt. **19**, 1505–1509 (1980).
19. P. Hodgson, *The Optical Model of Elastic Scattering* (Oxford University, 1963).
20. L. Schiff, *Quantum Mechanics* (McGraw-Hill, 1955).
21. A. Messiah, *Mécanique quantique* (Dunod, 1959).
22. L. Landau and L. Lifshitz, *Mécanique quantique: théorie non-relativiste* (Mir, 1981).
23. L. Valentin, *Physique subatomique: noyaux et particules* (Hermann, 1982).
24. C. Cohen Tannoudji, B. Diu, and F. Laloë, *Mécanique quantique II* (Hermann, 1997).
25. H. Kroemer, *Quantum Mechanics: For Engineering, Materials Science, and Applied Physics*, Prentice-Hall Series in Solid State Physical Electronics (Prentice-Hall, 1994).
26. H. Pruppacher and J. Klett, *Microphysics of Clouds and Precipitation* (Springer, 1997).
27. G. L. Stephen and S.-C. Tsay, "On the cloud absorption anomaly," Q. J. R. Meteorol. Soc. **116**, 671–704 (1990).
28. P. Pilewski and F. P. J. Valero, "Direct observations of excess solar absorption by clouds," Science **267**, 1626–1629 (1995).
29. R. Cess, M. Zhang, P. Minnis, L. Corsetti, E. Dutton, B. Forgan, D. Garber, W. Gates, J. Hack, E. Harrison, X. Jing, J. Kiehi, C. Long, J. Morcrette, G. Potter, V. Ramanathan, B. Subasilar, C. Whitlock, D. Young, and Y. Zhou, "Absorption of solar radiation by clouds: observation versus models," Science **267**, 496–499 (1995).
30. A. Arking, "Absorption of solar energy in the atmosphere: discrepancy between model and observations," Science **273**, 779–782 (1996).

Bibliography

J. Adam. The mathematical physics of rainbows and glories. *Physics Reports*, 356(4):229 – 365, 2002.

L. Bi, P. Yang, G. Kattawar, and I. Mishchenko. Optical tunneling by arbitrary macroscopic three-dimensional objects. *Phys. Rev. A*, 92(4), 2015.

M. Born and E. Wolf. *Principles of Optics*. Pergamon Press, 2006.

F. Bréon and P. Goloub. Cloud droplet effective radius from spaceborne polarization measurements. *Geophysical Research Letters*, 25(11):1879–1882, 1998.

J. Bricard. Contribution à l'étude des brouillards naturels - (Constitution et propriétés. Diffusion et diffraction de lumière par les gouttelettes d'eau). *Ann. Phys.*, 11(14):148–236, 1940.

H. Bucerius. Therorie des regenbogens und der glorie. *Optik*, 1(3):188–212, 1946.

C. Cohen-Tannoudji, B. Diu, and F. Laloe. *Mécanique quantique II*. Hermann, 1997.

P. Deschamps, F. Breon, M. Leroy, A. Podaire, A. Bricaud, Buriez, and G. J. Seze. The polder mission: instrument characteristics and scientific objectives. *IEEE Transactions on Geoscience and Remote Sensing*, 32(3):598–615, May 1994. doi: 10.1109/36.297978.

L. G. Guimaraes and H. M. Nussenzveig. Uniform approximation to mie resonances. *Journal of Modern Optics*, 41(3):625–647, 1994.

G. M. Hale and M. R. Querry. Optical Constants of Water in their 200 nm to 200 ¯m Wavelength Region. *Applied Optics*, 12(3):555–563, 1973.

H. Hertz. The forces of electrical oscillations, treated by maxwell's theory. *Ann.der Physik*, 36, 1889.

P. E. Hodgson. *The Optical Model of Elastic Scattering*. Oxford University Press, 1963.

B. R. Johnson. Theory of morphology-dependent resonances: shape resonances and width formulas. *J. Opt. Soc. Am. A*, 10(2):343–352, Feb 1993.

B. Jonsson and S. T. Eng. Solving the schrodinger equation in arbitrary quantum-well potential profiles using the transfer matrix method. *IEEE Journal of Quantum Electronics*, 26(11), 1990.

V. Khare. Surface waves and rainbow effects in the optical glory, 1982.

V. Khare and H. M. Nussenzveig. *The Theory of the Glory*. Springer, 1977.

H. Kroemer. *Quantum Mechanics: For Engineering, Materials Science, and Applied Physics*. Prentice-Hall series in solid state physical electronics. Prentice Hall, 1994.

L. D. Landau and L. M. Lifshitz. *Mécanique quantique : théorie non relativiste*. Mir, Moscou, 1981.

P. Laven. Simulation of rainbows, coronas, and glories by use of mie theory. *Appl. Opt.*, 42 (3):436–444, Jan 2003.

P. Laven. Noncircular glories and their relationship to cloud droplet size. *Appl. Opt.*, 47(34): H25–H30, Dec 2008a.

P. Laven. Effects of refractive index on glories. *Appl. Opt.*, 47(34):H133–H142, Dec 2008b.

K.-n. Liou and J. E. Hansen. Intensity and polarization for single scattering by polydisperse spheres: a comparison of ray optics and mie theory. *Journal of the Atmospheric Sciences*, 28(6):995–1004, 1971.

D. K. Lynch and S. N. Futterman. *Appl. Opt.*, 30(24):3538–3541, 1991.

A. Messiah. *Mécanique quantique*. Dunod, 1959.

G. Mie. Beiträge zur Optik träber Medien, speziell kolloidaler Metällosungen. *Annalen der Physik*, 330(3):377–445, 1908.

R. G. Newton. *Scattering Theory of Waves and Particles*. Dover Publications, 2002.

H. M. Nussenzveig. High-frequency scattering by an impenetrable sphere. *Annals of Physics*, 34(1):23 – 95, 1965. ISSN 0003-4916.

H. M. Nussenzveig. Complex angular momentum theory of the rainbow and the glory. *J. Opt. Soc. Am.*, 69(8):1068–1079, 1979.

H. M. Nussenzveig. *Diffraction Effects in Semiclassical Scattering*. Cambridge University Press, 1992. doi: 10.1017/CBO9780511599903.

H. M. Nussenzveig. Does the glory have a simple explanation? *Opt. Lett.*, 27(16):1379–1381, 2002.

H. M. Nussenzveig. Light tunneling in clouds. *Appl. Opt.*, 42(9):1588–1593, Mar 2003.

H. M. Nussenzveig. *Diffraction effects in semiclassical scattering*, volume 1. Cambridge University Press, 2006.

H. M. Nussenzveig. The Science of the Glory. *Scientific American*, 306:68–73, 01 2012.

H. M. Nussenzveig and W. J. Wiscombe. Diffraction as tunneling. *Phys. Rev. Lett.*, 59: 1667–1670, 1987.

J. Pérez, R. Carles, and O. Pujol. *Quantique, fondements et applications*. De Boeck, 2013.

J. F. Pernter and F. M. Exner. *Meteorological optics*. W. Braumüller, 1910.

H. R. Pruppacher and J. D. Klett. *Microphysics of Clouds and Precipitation*. Springer, 1997.

O. Pujol, R. Carles, and J. P. Pérez. Quantum propagation and confinement in 1D systems using the transfer-matrix method. *European Journal of Physics*, 35(3):035025, 2014.

B. Ray. The Formation of Coloured Bows and Glories. *Nature*, 111:183–183, 01 1923. doi: 10.1038/111183a0.

L. I. Schiff. *Quantum Mechanics*. McGraw-Hill, 1955.

J. A. Stratton. *Electromagnetic theory*. McGraw-Hill New York, 1st ed. edition, 1941.

J. R. Taylor. *Scattering Theory: The Quantum Theory on Nonrelativistic Collisions*. John Wiley & Sons, 1972.

G. Tissandier. *Ombres extraordinaires Spectres aériens et auréoles lumineuses*, volume 1 – 26. Imp. Simon Racon et comp., 1873.

A. Ulloa, J. Juan, G. Vega, and C. A. Jombert. *Voyage historique de l'Amérique meridionale: fait par ordre du roi d'Espagne par Don George Juan et par Don Antoine de Ulloa.* Arksteé & Merkus Amsterdam ; Leipzig, 1752.

L. Valentin. *Physique subatomique : noyaux et particules.* Hermann Paris, 1982. ISBN 2705659285.

H. C. Van De Hulst. A theory of the anti-coronae. *J. Opt. Soc. Am.*, 37(1):16–22, Jan 1947.

G. N. Watson. *A treatise on the theory of Bessel functions.* Cambridge university press, 1995.

C. T. R. Wilson. Nobel banquet speech. https://www.nobelprize.org/prizes/physics/1927/wilson/speech/, 1927.

R. Yaacoub, O. Pujol, and P. Dubuisson. Tunneling optical resonances in light–droplet interactions: simulations of spaceborne cloud droplet observations. *J. Opt. Soc. Am. A*, 36 (12):2076–2088, Dec 2019.

C. Zender and J. Talamantes. Solar absorption by Mie resonances in cloud droplets. *J. Quant. S. Rad. Trans.*, 98:122–129, 2006.